이학박사 학위논문

STM study of one-dimensional topological system and 1UC-$FeSe/SrTiO_3$ Superconductor

일차원 위상학적 시스템과 1UC-$FeSe/SrTiO_3$ 초전도체에 대한 주사터널링현미경 연구

2018 년 2 월

서울대학교 대학원
물리천문학부
오 명 철

STM study of One-dimensional Topological System and 1UC-$FeSe/SrTiO_3$ Superconductor

일차원 위상학적 시스템과 1UC-$FeSe/SrTiO_3$ 초전도체에 대한 주사터널링현미경 연구

지도 교수 국 양

이 논문을 이학박사 학위논문으로 제출함
2017 년 12 월

서울대학교 대학원
물리천문학부
오 명 철

오명철의 이학박사 학위논문을 인준함
2018 년 1 월

위 원 장 최 석 봉 (인)

부위원장 국 양 (인)

위 원 차 국 린 (인)

위 원 김 기 훈 (인)

위 원 서 정 필 (인)

Abstract

The discovery of the integer quantum hall effect has led to a lot of research on the system topology. Studies on 2D or 3D topological systems, which have been studied extensively in recent years, have improved the understanding of new physical properties that the system topology has not been known so far. Studies on 1D topological systems have also been initiated by Su-Schrieffer-Heeger(SSH), and many exotic phenomena such as the Majorana zero mode have been found so far. There are not many examples of 1D systems that have been isolated yet. Through this thesis I report that the Se atom is self-assemble on Ge (111) and is arranged in a staggered hopping structure, and its unique structure makes a system similar to polyacetylene. It has been shown that topological edge states are possibly created at both ends of the wire. In the same way, the self-assembled island as well as the one-dimensional wire were found to have a state at the edge.

Besides the topological insulator, there is another high-Tc superconductor (HTSC) as another strongly correlated system. The paring mechanism in HTSC is not well known yet. Many HTSCs have been studied with STMs, but in this paper we have studied FeSe / SrTiO3(100), an interface induced thin film superconductor first reported in Xue group in 2012. Two-dimensional high-temperature superconductors and the unusually high superconducting phase transition temperatures only appear on SrTiO3 or Titanate substrates have led to a number of studies on the mechanism of this exotic phenomenon. I observed at the dopant state while adjusting the doping level in this article, and I studied at how its ordering contributes to the formation of high Tc. We also studied the bosonic mode which makes pairing based on the Migdal-Eliashberg model.

Keywords: Topological system, High-Tc superconductor, FeSe/STO
Student Number : 2014-30112

Table of Contents

List of Figures

1. Introduction

More than thirty years after its invention by G. Binnig and H. Rohrer Scanning Tunneling Microscope (STM) has been used in a wide range of research area, and proven itself a useful instrument to investigate diverse conducting materials. By resolving the Si(111) 7X7 reconstruction structure, STM opened a new era in the observing nano-sized structures. It stimulates many enthusiastic scientists to conduct various experiments in surface science of condensed matter, and inspires creative ones to develop new scheme of instruments, such as Atomic Force Microscope. It is suitable system so far to measure not only atomic scale topographic feature but also local density of states of electrons. In addition to observe electronic topography and spectroscopy, STM can manipulate several atoms to position specific location on the surface, and this can results distinctive quantum mechanical behaviors. Recently, many studies on low-dimensional materials have been performed using STM characteristics. Since STM has surface-sensitive characteristics like Angle Resolved Photoemission Spectroscopy (ARPES), it is suitable for measuring Graphene, Transition Metal Dichalcogenides(TMD), Topological Insulator (TI) and so on.

Since Su-Schrieffer-Heeger suggested the theory about polyacetylene[1] simple topological system, one-dimensional topological system has been understood much, but due to the difficulty to create an isolated system compared to a 2D [2]–[5] or 3D[6]–[8]topological cases , little experimental studies were conducted. Nevertheless, edge state in 1D topological system has exotic phenomena like Majorana zero mode[9], [10] at the edge state which occurs in superconducting 1D topological system. We show here that Se can separate the 1D wire from the system generated by the passivation created on Ge (111) and have a topological edge state. If the edge of a 1D wire has one atomic termination, the edge mode can be determined from this unique termination, and the edge state

is created and protected due to the topology of the wire and its robustness is observed.

Another strongly correlated system is a High−T_c superconductor (HTSC). Since the BCS theory has a high Tc which is difficult to explain, there is still much discussion about the pairing mechanism. There are some theories that the phonon is involved in pairing as well as the spin−fluctuation mechanism, the orbital−fluctuation mechanism and the conventional superconductor. The recently discovered FeSe / $SrTiO_3$(100) [11] is attracting people's attention because it is a two−dimensional system with HTSC, and it shows different characteristics from the gap symmetry seen so far. Since this sample only produced a superconducting phase at 1UC, the ARPES[12]–[15] and STM[16]–[18] studies were more involved than the transport experiments. The fact that the superconducting layer is well exposed also facilitates the study of STM.

To study the pairing mechanism of FeSe / STO(100), it was experimented with STM. According to Migdal−Eliashberg theory[19], a bosonic mode feature interacts with the pairing electron outside the Gap, which is analogous to the pairing mechanism. I also observed the dopant state under the under−doped state while controlling the doping level of the FeSe / STO(100) system and observed its long range ordering.

2. Scanning Tunneling Microscopy

2.1. Quantum Tunneling of Electrons

2.1.1. Introduction

The study on quantum tunneling phenomenon started from explaining the phenomenon such as α−decay, field ionization of hydrogen and field emission in the early stage of quantum mechanics in 1920s, and has been applied to many fields through subsequent studies. Quantum tunneling is a pure quantum mechanical nature, in which particles with small masses go beyond potential barriers that cannot overcome in classical mechanics.

Quantum mechanically, in the stationary state, the probability density of finding a particle of energy E at certain position $\vec{r}$ can be given by $|\psi(\vec{r})|^2$, where $\psi(\vec{r})$ is a single particle wave function, which can be obtained by time−independent Schrödinger equation

$$-\frac{\hbar^2}{2m}\nabla^2\psi(\vec{r}) + V(\vec{r})\psi(\vec{r}) = E\,\psi(\vec{r}) \qquad (1)$$

for given potential $V(\vec{r})$.

For a simple one−dimensional case, we can think a square potential well with width d and height V_0 as shown in Figure 1. In the left and right region, potential is $V(\vec{r}) = 0$, while the magnitude of potential is V_0 in the barrier region. For a particle with energy E $(0 < E < V_0)$, one can obtain standing wave solution with wave number $\mathrm{k} = \frac{\sqrt{2mE}}{\hbar}$ in the left region where the particle comes in and the right region where the particle goes out. Although it is forbidden in classical mechanics, still there is a solution in the barrier region in quantum mechanics. In this region, the solution is exponentially decaying in the form of an evanescent wave with the decay length $\kappa = \frac{\sqrt{2m(V_0-E)}}{\hbar}$. In order to satisfy the continuity of the wave function in the boundary of each region, $\psi(x)$ must be matched. After $d\psi(x)/dx$ is matched at the edges of the regions in order to satisfy the equation

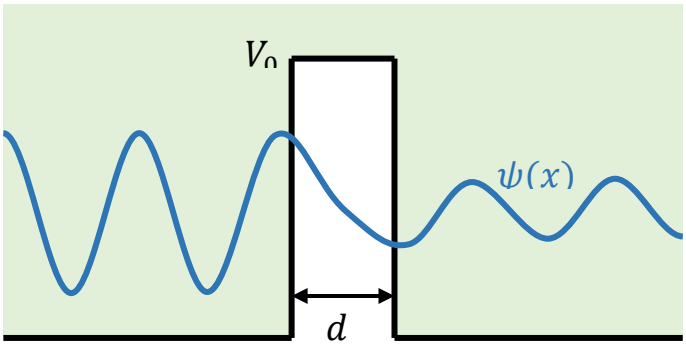

Figure 1. Tunneling through a square potential well

The amplitude of the wave function (only the real part of is plotted) of an electron coming from the left is damped in the barrier region but still there is a finite possibility of finding the particle on the right.

above, the amplitude ratio t of the wave function when the particle moves from the left region to the right region is derived, and we can derive transmission ratio which is a square of amplitude ratio when $\kappa \gg d^{-1}$,

$$T = |t|^2 \approx \frac{16k^2\kappa^2}{(k^2+\kappa^2)^2}\exp(-2\kappa d)\,. \qquad (2)$$

Since the transmission ratio exponentially decays according to the width of the barrier, the width of the potential barrier must be very small in order to measure the tunneling phenomenon and this explains why tunneling phenomenon does not appear in the macroscopic system.

Through the one-dimensional equation we have seen so far, one can deduce the case of Scanning Tunneling Microscopy(STM). The STM is different from the one-dimensional case described above. A sample has a flat shape, but a tip has a non-flat geometry even at atomic size. This form is able to induce local transfer of the tunneling current, and when it is measured, the topographic features of the electronic density of the sample surface can be observed.

For the simple model, one can assume the shape of the STM tip apex is almost hemispherical. If the radius of the tip apex is R, distance difference from tip to sample can be calculated

$$\Delta z = R - Rcos\theta = R\left(1 - \sqrt{1 - \frac{\Delta x^2}{R^2}}\right) \approx \frac{\Delta x^2}{2R}. \qquad (3)$$

From equation (2), tunneling current dependence at the position Δx at the tip apex can be derived as,

$$I(\Delta x) \propto e^{-\kappa\frac{\Delta x^2}{R}}. \qquad (4)$$

Typically, $\kappa \sim 1\text{Å}^{-1}$. Therefore, $\mathrm{R} = 1\mathrm{nm}$ and $\Delta x \sim 3.3\text{Å}$ lead e^{-1} factor, which can be defined resolution limit of the STM tunneling current imaging. Recently, controlling and functionalizing tip apex lead a much better resolution for STM imaging, which allows us to see atomic features.

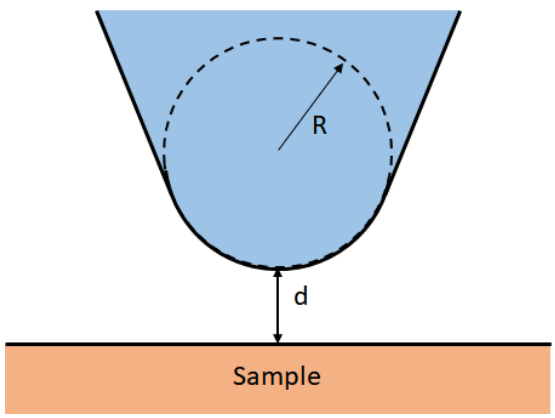

Figure 2. Schematic image of STM tunneling junction

2.1.2. Bardeen Tunneling

After I. Giaver measured the tunneling current at the superconductor tunneling junction in 1960[20], J.Bardeen analyzed the tunneling at the planar junction in many-body viewpoints in 1961[21]. The model used by Bardeen is called the Transfer Hamiltonian method, extended by Tersoff, Haman[22], [23] and Chen[24] and can be used to describe the STM. This model has some limitations to apply to actual STM in the basic assumption, but it gives a fundamental understanding of STM.

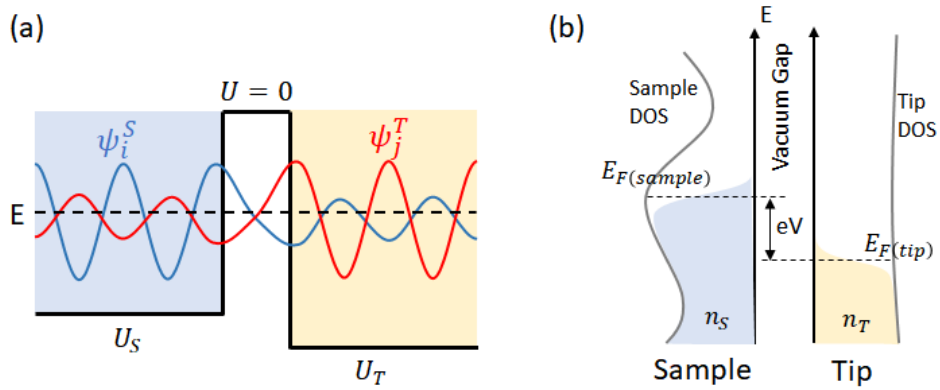

Figure 3. Schematic of Bardeen tunneling

Bardeen's tunneling theory is based on the following assumptions. First of all, all electrons are treated as single particles and interactions between electrons are neglected. Such an approximation is reasonable when the energy of the tunneling electrons is low. Next, the coupling of electronic states of tip and sample due to the direction interaction between tip and sample is not considered. This assumption is valid when the distance between tip and sample is sufficiently large(>4Å). Third, only the elastic process of the tunneling electrons are taken into account. In other words, energy loss due to quasi-particle excitation such as phonon, plasmon, and spin-excitation is not considered. A lot of research has been done on phenomena caused by inelastic processes recently, but this is covered later. Finally, it is assumed that the tunneling process is performed only in one dimension. Since we ignore the influence on tip-sample geometry, this also becomes a valid approximation when the distance between tip and sample is sufficiently large.

Now let S be the wave function of the unperturbed sample and T be the index of the unperturbed tip wave function. From the Schrodinger equation,

$$i\hbar\frac{\partial\psi^\alpha}{\partial t} = \left(-\frac{\hbar^2}{2m}\frac{\partial^2}{\partial z^2} + U_\alpha\right)\psi^\alpha \qquad (5)$$

, where U_α is potential function of α region (S or T), and ψ^α is dependent on both time and spatial coordinates. The stationary state are $\psi^\alpha = \psi_i^\alpha e^{-iE_i t/\hbar}$

, where E_i is eigenvalue of i−th state. Then the equation can be modified as

$$\left(-\frac{\hbar^2}{2m}\frac{\partial^2}{\partial z^2} + U_\alpha\right)\psi_i^\alpha = E_i\psi_i^\alpha. \quad (6)$$

Now, when tip and sample are close enough, the single electron wavefunction ψ can be derived from the equation,

$$i\hbar\frac{\partial\psi}{\partial t} = \left(-\frac{\hbar^2}{2m}\frac{\partial^2}{\partial z^2} + U_S + U_T\right)\psi. \quad (7)$$

Let's use time−dependent perturbation method. At $\mathrm{t}\to-\infty$, a tip is far from to sample surface and stationary state of electron can be represented ψ_i^S at sample region and there is no electron state at the tip. As time evolves, we can treat this equation adiabatically which is reasonable when the time−scale is larger than 10^{-15} sec. Then, we can think U_T is only time−dependent function which can be represented as,

$$U_T(t) = U_T e^{\lambda t/\hbar} \ (\lambda > 0). \quad (8)$$

When the tip approaches to sample, the electron state can be represented linear combination of unperturbed eigenstates of the both tip and sample,

$$\psi = c_i(t)\,\psi_i^S e^{-iE_i^S t/\hbar} + \sum_j d_j(t)\,\psi_j^T e^{-iE_j^T t/\hbar} \quad (9)$$

From the boundary condition at $\mathrm{t}\to-\infty$, $c_i(\mathrm{t}=-\infty)=1$ and $d_j(\mathrm{t}=-\infty)=0$. Since tip is approaching to sample so that U_T is time dependent function, we can assume that $c_i(t)$ and $d_j(t)$ are only depend on $U_T(t)$. With the Bardeen's assumption $\langle\psi_i^S|\psi_j^T\rangle \approx 0$, applying above equation to the equation (7) and project it with ψ_j^T,

$$i\hbar\frac{\partial d_j(t)}{\partial t} = \langle\psi_j^T|U_T|\psi_i^S\rangle e^{-\frac{i\left(E_i^S-E_j^T+i\lambda\right)t}{\hbar}} + \sum_n\langle\psi_j^T|U_S|\psi_n^T\rangle e^{-\frac{i\left(E_n^T-E_j^T\right)t}{\hbar}} \quad (10)$$

With time-dependent perturbation theory second-term of the right-hand side of the equation can be neglected because it is second-order process, therefore the equation can be simplified

$$i\hbar\frac{\partial d_j(t)}{\partial t} \approx \langle\psi_j^T|U_T|\psi_i^S\rangle e^{-\frac{i\left(E_i^S-E_j^T+i\lambda\right)t}{\hbar}} \tag{11}$$

Now, denote $M_{ij} \equiv \langle\psi_j^T|U_T|\psi_i^S\rangle$ which is tunneling matrix element, we can get

$$d_j(t) = \frac{1}{E_i^S - E_j^T + i\lambda} M_{ij} e^{-\frac{i\left(E_i^S-E_j^T+i\lambda\right)t}{\hbar}} \tag{12}$$

If we calculate tunneling probability $P_{ij}(t) = \frac{d}{dt}|d_j(t)|^2$ from sample to tip from i state to j state, and take $\lambda \to 0$ limit,

$$P_{ij}(t) = \frac{2\pi}{\hbar}\delta\left(E_i^S - E_j^T\right)|M_{ij}|^2 \tag{13}$$

which is Fermi Golden Rule, the result of first order time-dependent perturbation theory. Now we can think of the continuous energy spectrum in a continuum rather than a single state i and j. In this case, the electrons can tunnel in every state i and j in the energy spectrum. The occupation of electrons in the solid follows the Fermi-Dirac distribution. Now, when the voltage V is applied between the tip and the sample, the electrons are tunneled. In order for the electrons to be tunneled through the tunnel, the state for tunneling must be unoccupied. Considering the current flowing from the tip to the sample and the current flowing from the sample to the tip between the sample and the tip,

$$\begin{aligned} I_{S\to T} &= \frac{4\pi e}{\hbar}\sum_{ij} f(E_i^S - E_F^S)\left[1 - f\left(E_j^T - E_F^T\right)\right]|M_{ij}|^2\delta\left(E_i^S - E_j^T - eV\right) \\ I_{T\to S} &= \frac{4\pi e}{\hbar}\sum_{ij} f\left(E_j^T - E_F^T\right)\left[1 - f(E_i^S - E_F^S)\right]|M_{ij}|^2\delta\left(E_i^S - E_j^T - eV\right) \end{aligned} \tag{14}$$

In this equation, factor 2 is multiplied by the spin degeneracy of the electron. Therefore, net current I is,

$$I(V) = \frac{4\pi e}{\hbar}\sum_{ij}\left[f\left(E_j^T - E_F^T\right) - f(E_i^S - E_F^S)\right]|M_{ij}|^2\delta\left(E_i^S - E_j^T - eV\right) \tag{15}$$

The finite summation over discrete state can be converted by integral form by applying $\sum_i \rightarrow \int d\varepsilon\, \rho(\varepsilon)$, where $\rho(\varepsilon)$ is a density of states (DOS).

$$I(V) = \frac{4\pi e}{\hbar} \int d\varepsilon \left[f(E_F^T - eV + \varepsilon) - f\left(E_F^S + \varepsilon\right) \right] \rho_T(E_F^T - eV + \varepsilon) \rho_S(E_F^S + \varepsilon) \left| M(E_F^S + \varepsilon, E_F^T - eV + \varepsilon) \right|^2 \quad (16)$$

For T=0, Fermi-Dirac distribution function is changed to step function, and assuming $E_F^T = E_F^S = E_F$,

$$I(V) = \frac{4\pi e}{\hbar} \int_0^{eV} d\varepsilon\, \rho_T(E_F - eV + \varepsilon) \rho_S(E_F + \varepsilon) \, |M|^2 \quad (17)$$

For small bias voltage, assuming $\rho_T(\varepsilon) = \rho_T(E_F) = const$,

$$\frac{dI}{dV} \approx \frac{4\pi e}{\hbar} \rho_T(E_F) \rho_S(E_F + eV) \, |M|^2 \quad (18)$$

Therefore, we can measure DOS of the sample by tunneling current measurement. For the STM, this principle is used commonly for investigating local density of states (LDOS) of the sample surface.

2.1.3. Inelastic Electron Tunneling Spectroscopy

STM not only observes the local electronic structure of the surface, but also the vibration mode of molecules and the bosonic mode of the sample surface such as phonon, surface-plasmon excitation. Inelastic Electron Tunneling Spectroscopy (IETS) observes the phenomenon that excitation of bosonic mode generates a new channel through which electrons tunnel through an interaction with an electron tunneling (e.g. coulomb interaction or spin interaction). When a new tunneling channel is opened due to bosonic mode, the tunneling current of the electron is further increased, and the step shape as shown in the following figure appears in the tunneling conductance. As a result, the tunneling current of the electron is further increased. As a result, a step form as shown in the following figure appears in the tunneling conductance. To calculate this, we can use equation discussed previously. Consider the potential U_S containing vibrating adatom with frequency ω. Then, we

can use time dependent potential $U_S + U_0\cos(\omega t)$, rather than U_S. By applying the equation result discussed previously,

$$i\hbar\frac{\partial d_j(t)}{\partial t} = M_{ij}e^{-\frac{i\left(E_i^S - E_j^T + i\lambda\right)t}{\hbar}} + \delta M_{ij}\cos(\omega t)e^{-\frac{i\left(E_i^S - E_j^T\right)t}{\hbar}} \quad (19)$$

, where $M_{ij} = \langle\psi_j^T|U_T|\psi_i^S\rangle$ and $\delta M_{ij} = \langle\psi_j^T|U_0|\psi_i^S\rangle$.
After integration, the inelastic contribution of the coefficient $d_j(t)$ becomes

$$\delta d_j(t) = \frac{\delta M_{ij}}{2}\left[\frac{e^{-\frac{i(E_i - E_j + \hbar\omega)t}{\hbar}}}{E_i - E_j + \hbar\omega} + \frac{e^{-\frac{i(E_i - E_j - \hbar\omega)t}{\hbar}}}{E_i - E_j - \hbar\omega}\right] \quad (20)$$

One can derive inelastic contribution of tunneling probability P_{ij} likewise equation 13,

$$\delta P_{ij} = \frac{d}{dt}\left|\delta d_j(t)\right|^2 \propto \frac{2\pi}{\hbar}\delta\left(E_i - E_j \pm \hbar\omega\right)\left|\delta M_{ij}\right|^2 \quad (21)$$

Thus, contributions to inelastic tunneling are added to equations 14−16. As a result, the inelastic term is added to the dI/dV in the existing elastic term, which makes the particle−hole symmetric feature at fermi energy + $\hbar\omega$ energy level, due to δP_{ij} is proportional to $\delta\left(E_i - E_j \pm \hbar\omega\right)$. If we calculate this more precisely, we will see a figure in the form of a step in the form shown in figure 4b. In other words, when the inelastic tunneling channel is opened in the density of state of the observed sample and the changed dI/dV is further differentiated, the value corresponding to the original vibration energy appears. In the case of a molecule or a single atom, the dip−peak feature as shown in figure 4c appears at d^2I/dV^2 because it has a discrete vibration mode. Phonon mode can be expressed in the same way. Especially, since the inelastic scattering becomes strong in the optical phonon with narrow dispersion in phonon density of state or Van hove Singularity in acoustic phonon mode, it is possible to observe specific phonon modes through IETS.

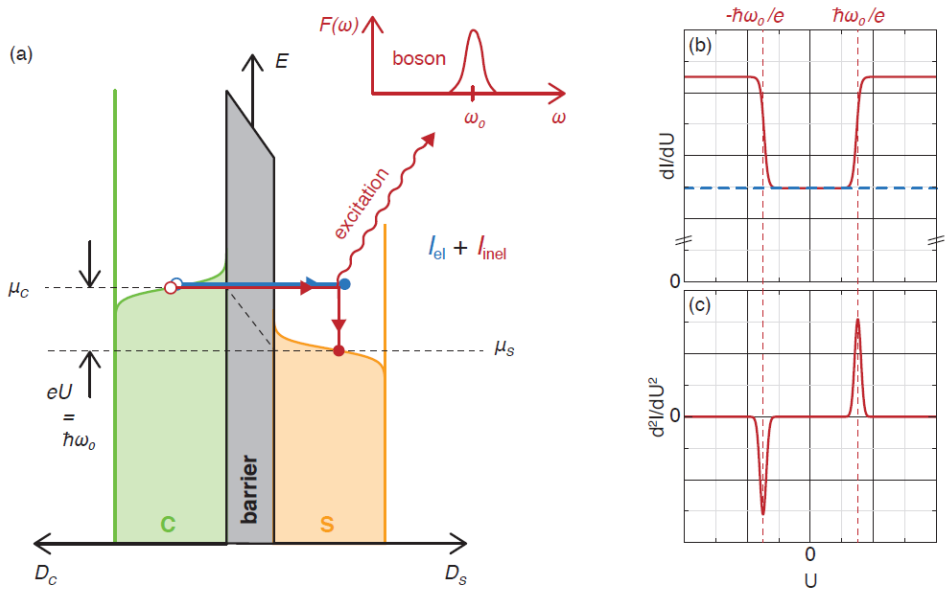

Figure 4. Principle of inelastic electron tunneling spectroscopy (taken from [25])

2.2. Scanning Tunneling Microscopy

Bardeen's equation includes the local density of states (LDOS) of sample at the position $\vec{r_t}$ term, which is $\sum_\nu |\Psi_\nu(\vec{r_t})|^2 \, \delta(E_\nu - E_\mu) \equiv \rho_S(\vec{r_t}, E_F)$. Assuming that the tunneling matrix and the LDOS of the tip are constant, differential tunneling conductance at the specific location is proportional to LDOS at the given voltage, such as

$$\frac{dI}{dV} \propto \rho_S(E_F - eV). \tag{22}$$

Thus, so called scanning tunneling spectroscopy which visualizes LDOS is the imaging the spectrum of differential tunneling conductance at the given position by sweeping bias voltage.

On the other hand, topography is mapping the intensity of tunneling current, on the ground that tunneling current is exponentially decreases when the tip becomes more distant from the sample. A topographic image can be obtained by two methods; constant height method and constant current method. In the constant

height method, the height of a tip is fixed, and STM records the tunneling current flowing between them. By imaging the distance calculated from current-height relation with recorded current, topographic image can be acquired. However, if the set position of tip is lower than sample surface, the tip may be damaged by collision with sample.

In the constant current, distance between tip and sample is determined from current feedback. STM keeps the flows of tunneling current constant by fixing distance with tip and sample. This distance can be controlled with a z-feedback piezoelectric transducer and the z-feedback information at each point is recorded to draw a topographic image. This method doesn't need burdensome height calculations and prevents tip-sample collision.

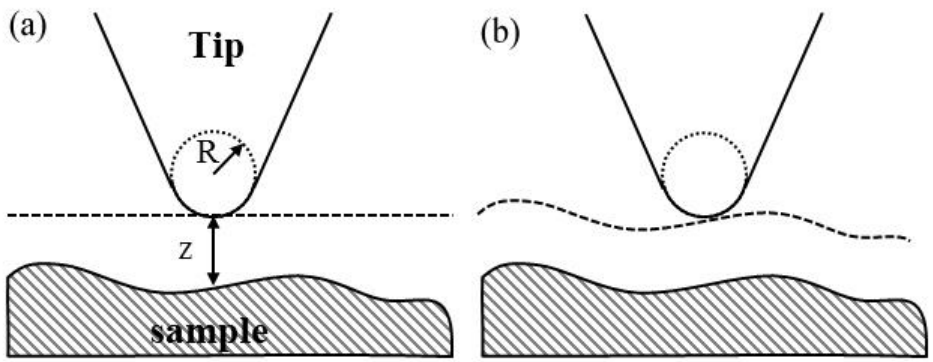

Figure 5. Schematic of picture of STM tip and sample surface with distance z and local radius R.
(a) constant height mode, (b) constant current mode.

3. Experimental Setup and Method

3.1. STM System Setup

Before presenting the results of the experiment, we will first look at the equipment used here. This equipment was completed in the laboratory by students and professors' ideas and efforts from designing to assembling. The temperature can be lowered to 5.9K, and the temperature can be controlled with PID controller with continuous cooling cryostat system. In-situ sample growth and measurement is also possible because the scanner and sample preparation equipment are in an ultrahigh vacuum (UHV) chamber. Therefore, it is possible to measure the physical properties of uncontaminated samples. In this section, we will introduce and explain each part of this STM.

3.1.1. STM Head

We can see head part of STM which is integral part of the scanning tunneling microscope system. The STM scanner fabricated in the laboratory approaches a tip near to the sample with a Pan-type walker[26].The specification of the scanner is that the maximum scan range is 700 x 7000 nm2 considering the maximum voltage of ±140V of the electronics used and in the 5.8 K, 2.5 nm/V in the XY direction and 0.5 nm/V in the Z direction. The CAD and photo of the STM head are depicted in Figure 6 and Figure 7.

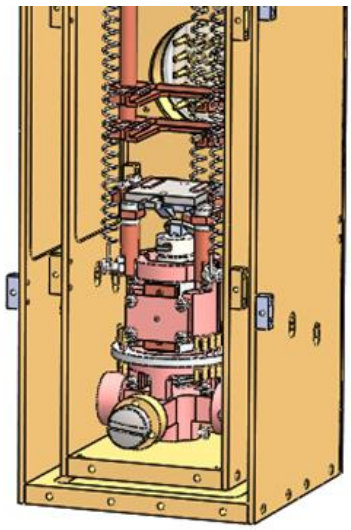

Figure 6. CAD image of STM head

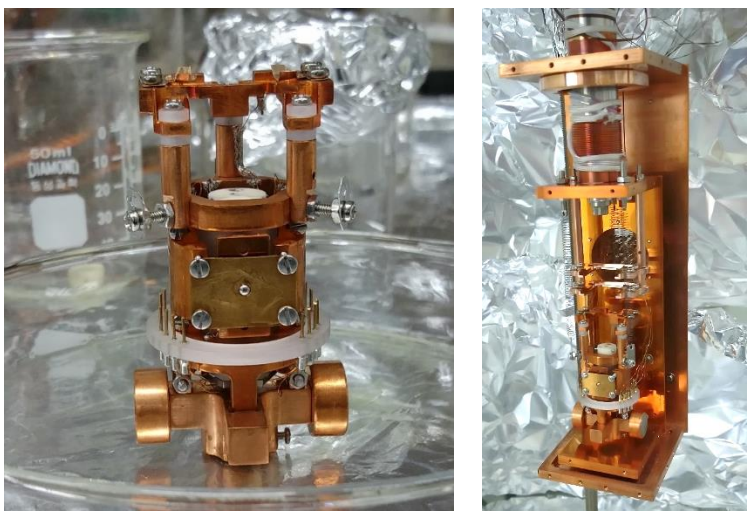

Figure 7. Pictures of STM Head

3.1.2. Ultra High Vacuum System

This STM was installed inside an ultrahigh vacuum (UHV) chamber. This section discusses the UHV chamber. The fabricated chamber consists of a preparation chamber and main chamber Figure 8. The preparation chamber is used for sample preparation and

growth. And the main chamber is used for sample loading and scanning. In the preparation chamber, there is a sample heater for sample heating and annealing by e-beam and filament heating. And there is a tip heater for annealing and sputtering a tip. There is also an ion gun for sample sputtering. Finally, there is a tip heater which can heat and self-sputter a tip in order to clean it. There is also a carrousel storage that can store several samples and tips. The prepared sample can be transferred to the main chamber by tray and loaded on the scanner with wobble stick motion. Everything from preparation to experiment is done in ultra-high vacuum (Figure 9, Figure 10)

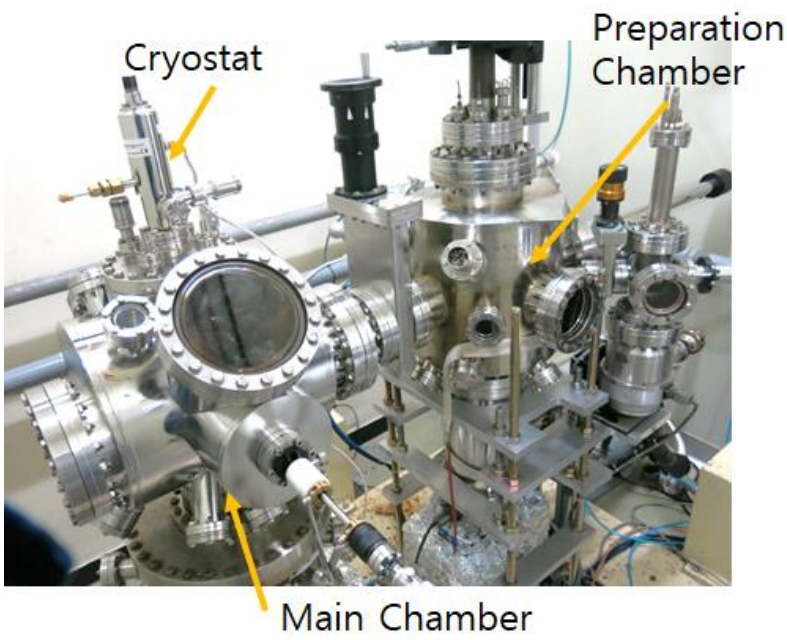

Figure 8. UHV main chamber and preparation chamber.

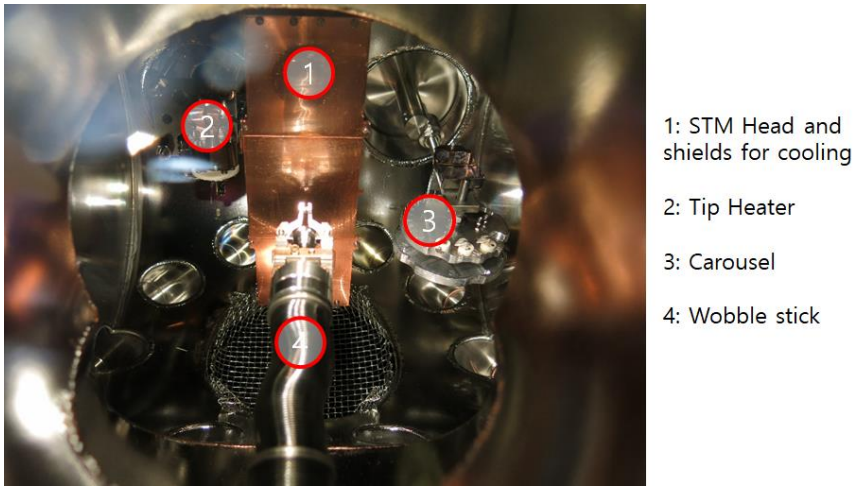

Figure 9. Main chamber configuration

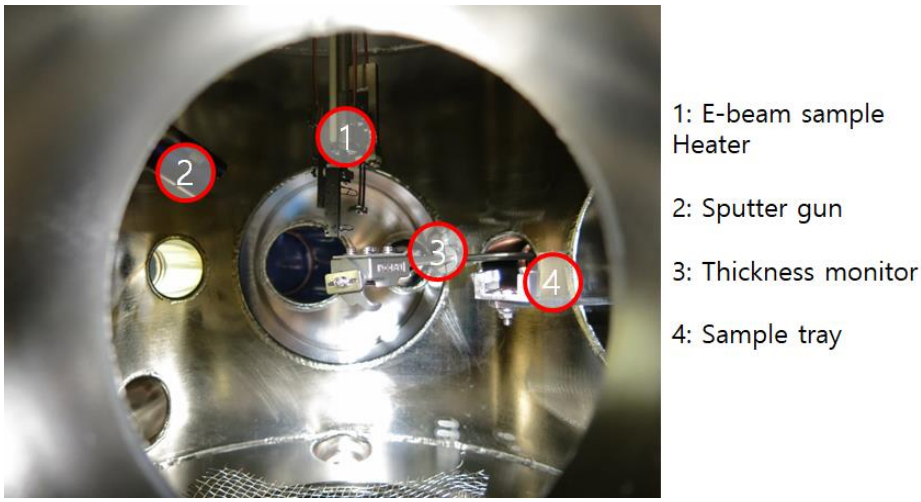

Figure 10. Preparation Chamber Configuration

3.1.3. Micro Four Point Probes

The four point probe measurement method is a suitable method for measuring the electronic transport properties of surfaces [27]. In general, it is difficult to measure the characteristics of a sample with a resistance or a very small material such as a superconductor. This is because of the contact resistance of the probe. If you try to measure the resistance of the sample with two probes, the wire or

contact resistance in the current path will give additional resistance. The four-point probe measurement has been developed to solve this problem, and its principle is as follows. Taking the simplest linear probe measurement as an example, four probes are lined up at the same interval, and the current flows out of the probe. Then an E-field is formed along the direction of the current and a potential is formed along the direction perpendicular to the E-field. Then you can measure only the potential difference between the two probes using the other two probes. If the impedance of the probe that measures the potential is made very large, the loss of the measuring current does not occur, and the low resistance can be measured. This principle is used to measure the transport properties of the sample. Recently, a lot of research has been done on low dimensional materials[12], [28]–[30], and studies have been made to measure transport by growing a thin film and depositing electrodes directly on the sample.

However, this fabrication process is difficult in cases where the sample is easily broken when exposed to air. Covering the capping layer to prevent it can affect the intrinsic properties of the sample, so once the sample is grown on the UHV, it is better to observe it in-situ. Moreover, in the case of four-point probe measurement, as the probe interval increases, the electric field generated by the probe will act to the depth. In the case of such a wide probe, not only the characteristics of the direct sample but also the effect of the substrate is measured. However, the narrower the probe spacing, the smaller the electric field penetrating into the sample, resulting in a more surface sensitive result. (Figure 11) Combining this system with variable temperature STM allows for in-situ viewing of transport properties with temperature on UHV grown samples. I made this study possible by combining a micro-four-point-probe (M4PP) sensor made by CAPRES to Scanning Tunneling Microscope head Figure 12.

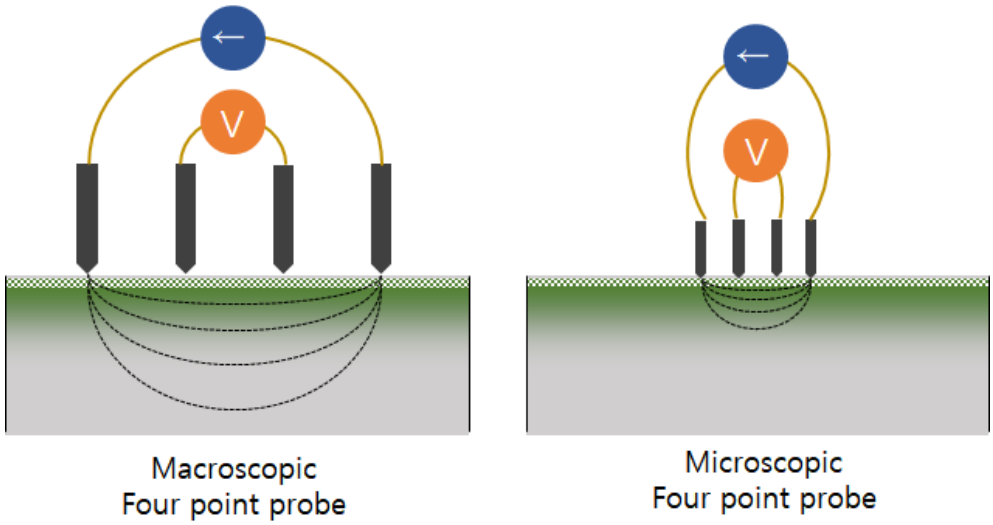

Figure 11. Schematic image of macroscopic four-point probe and microscopic four point probe.

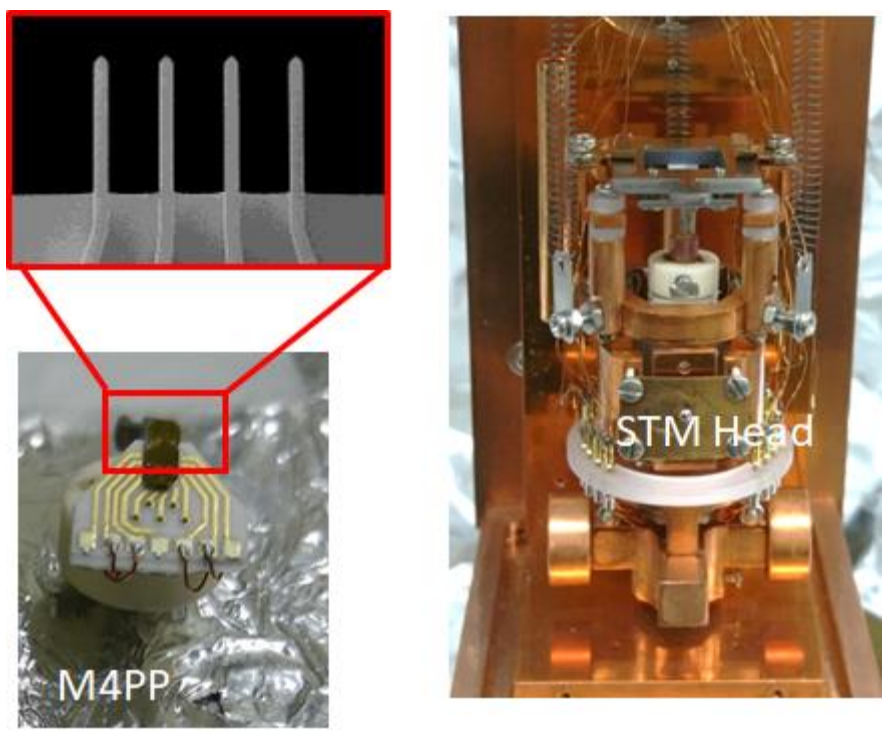

Figure 12. Micro four-point-probe(M4PP) mountable VT-STM system

3.2. System for *in situ* Sample Preparation

3.2.1. Sputter and annealing

A common method of cleaning crystal samples is the ion bombardment and annealing (IBA) process. By physical bombardment of ion to the sample surface it removes contaminations or segregated material which is followed by annealing process which smoothens surface corrugation.

For this process, a leak valve is installed in the preparation chamber to inject Ar gas and an ion gun is installed for ion sputtering as well. Prior to starting the sputtering process, place the sample in a heater and align the heater to the specified position. Then, the sputter gun is operated for 5 to 10 minutes with the Ar gas backfilled at about 10^{-5} torr for ion sputtering. Immediately following annealing is done by heating the sample using an e−beam heater. E−beam heating is a method of heating a sample by accelerating thermionic emitted electron from a filament by applying a high voltage to the filament and generating kinetic energy delivered to sample.

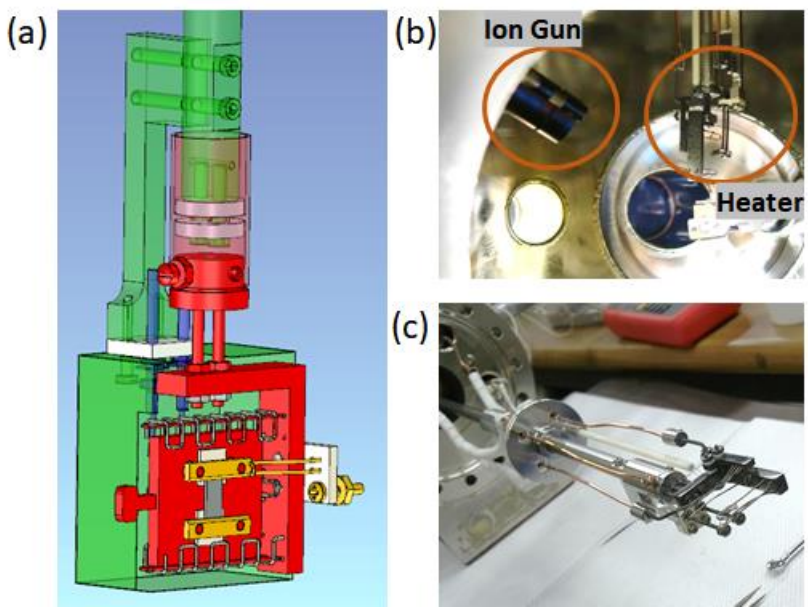

Figure 13. Sample heating and sputtering system

3.2.2. Source preparation

The deposition sources used in this paper are Fe and Se. Since the melting point of Se is as low as 217℃, the range of evaporation temperature is about 150 ~ 180℃. Therefore, the source can be evaporated using a typical Knudsen cell. Since Se is a substance with high reactivity, alumina(Al_2O_3) or p-BN is suitable materials for crucible to evaporate the source. A tungsten wire with a diameter of 0.5 mm is wound around the tapped crucible, and when the tungsten wire is flowed at around DC 2A, the temperature is saturated and evaporated at about 30 to 40 minutes. I wrapped the crucible with a stainless-steel shield attached to the water cooling part so that the surroundings were not heated by the radiation and the pressure did not rise. Due to the reactivity of Se, the shield made of Ta or Cu is easily corroded.

The Fe source is different from the Se source. Similar to Se, it can be deposited using crucibles using alumina. However, due to the high deposition temperature of Fe, outgassing occurs at the crucible and its surroundings during deposition, which adversely affects the purity of the grown sample. Therefore, unlike Se, the Fe source uses an e-beam heating method for the iron rod. The iron rod is connected to the flange while making thermal insulation by using a thin tungsten wire which is bonded by spot welding. The tungsten filament is placed around the iron rod to flow electric current to the filament, High voltage is applied to collide electron to Fe rod. Then, the kinetic energy of the electron is changed from the iron rod to the thermal energy and the iron rod is heated to the evaporation temperature. Similarly, there is a radiation shield. Because of the high evaporation temperature of Fe, the shielding is done using a water jacket because of the large amount of radiation coming out during deposition. The source evaporator was subjected to sufficient outgassing before use and the deposition rate could be calibrated using a homebuilt thickness monitor.

Figure 14. Knudsen cell for Se source deposition

4. One-dimensional Topological System -Se on Ge(111)

4.1. 1D Topological system

4.1.1. Introduction

A study of the topology of the system began with the discovery of Integer Quantum Hall Effect(IQHE) by von Klitzing in 1980. Since the birth of Landau theory which successfully described about second order phase transition, phase transition was thought to be understood by the spontaneous symmetry breaking of matter to the late 20th century. For example, crystal can be described as translational and rotational symmetry breaking, ferromagnetism and anti-ferromagnetism as rotational symmetry braking of spin space, liquid crystal as rotational but not translational, and superconductivity as gauge symmetry breaking. However, in the case of IQHE, resistance is quantized as the magnetic field varying without any apparent symmetry breaking, which is a multiple of a constant value (1 / 25812.807572Ω) regardless of the shape and size of the material and the degree of impurity, and it was a new type of phase transition.

4.1.2. Su-Schrieffer-Heeger Model

Representative example of simple topological system is a Su-Schrieffer-Heeger (SSH) model describing polyacetylene which is one-dimensional topological system. Polyacetylene consists of a chain of hydrogenated carbons as shown in Figure 15. This chain is dimerized around two carbons as shown in the figure due to Peierls instability at low temperatures, resulting in a super cell, and the electron hopping rate of the intra dimer and the inter dimer are different.

This staggered hopping nature can be described with Su-Schrieffer-Heeger(SSH) model[1] which describes polyacetylene atomic chain. This Hamiltonian can readily be transformed to Hamiltonian in one dimensional k-space,

$$\mathcal{H} = \int_0^{2\pi} \frac{dk}{2\pi} \left(\Psi^{\dagger}(k) H(k) \Psi(k) \right) \tag{23}$$

,where $H(k) = \begin{pmatrix} 0 & h(k) \\ h^*(k) & 0 \end{pmatrix} = \begin{pmatrix} 0 & t_1 + t_2 e^{ik} \\ t_1^* + t_2^* e^{-ik} & 0 \end{pmatrix}$, $\Psi(k) = \begin{pmatrix} \psi_A(k) \\ \psi_B(k) \end{pmatrix}$, t_1 is intra-dimer hopping constant, t_2 inter-dimer hopping constant, ψ_A and ψ_B are electron state at site A and site B, respectively (Fig. 4a). From this equation, the condition that a topological edge state can occur is that intra-dimer hopping should be smaller than inter dimer hopping. In the opposite case, the system only has a trivial state.

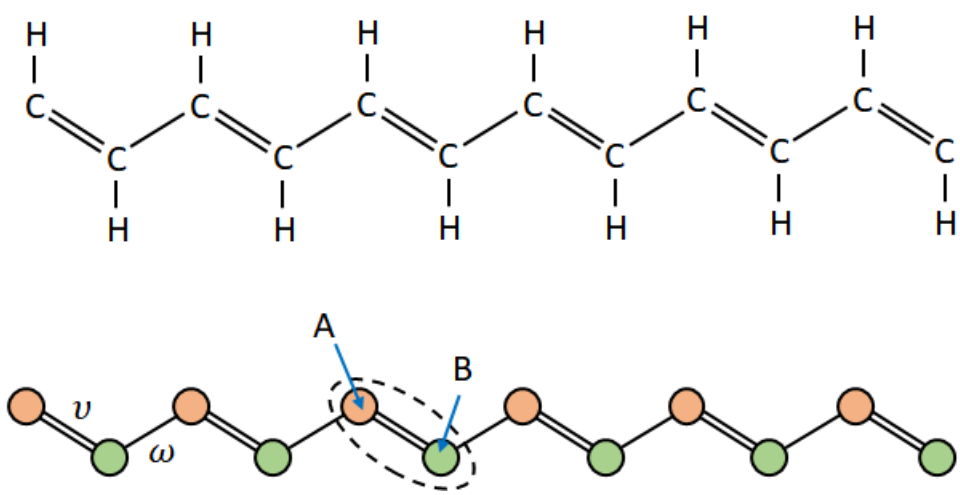

Figure 15. Polyacetylene(top) and Su-Schrieffer-Heeger Model(bottom)

When a topological edge state appears, a degenerated midgap state is created at both ends of the chain. This state has a coherent state at the left and right ends of the chain. If we denote as L on the electron state at left edge and R as the right edge state, the coherent state can be written as, $|0+\rangle = \frac{|\mathrm{L}\rangle + e^{i\phi}|\mathrm{R}\rangle}{\sqrt{2}}$, $|0-\rangle = \frac{|\mathrm{L}\rangle - e^{i\phi}|\mathrm{R}\rangle}{\sqrt{2}}$.

The important criteria that topological edge state occurs is intra cell hopping should be smaller than inter cell hopping. In other words, the topological edge state is attained when the end bonding of the chain is weakened, and the topological edge state cannot be obtained because the opposite case is well dimerized to the end atom.

4.2. Sample Preparation and Characterization

First, the Ge(111) substrate was cleaned to prepare the substrate. This germanium sample was degenerated doped with Ga (hole doped) and used after dicing a 2-inch wafer. When resistance increases due to Schottky barrier between metal and semiconductor, it is difficult to measure STM at low temperature, so Tantalum is put into contact material. Ge (111) was introduced into the UHV chamber after sonication using IPA, Acetone and DI water to remove the adhesive and contaminants.

In the UHV chamber, cleaning was started after outgassing at 600 ° C ~ 700° C for 8 hours. The IBA process was used. The surface was sputtered using Ar ion and the cycle of annealing at 650 ° C for 20 minutes was repeated. As a result, we obtained a well-known germanium c (2x8) [31] structure on the following clean terraces (Figure 16)

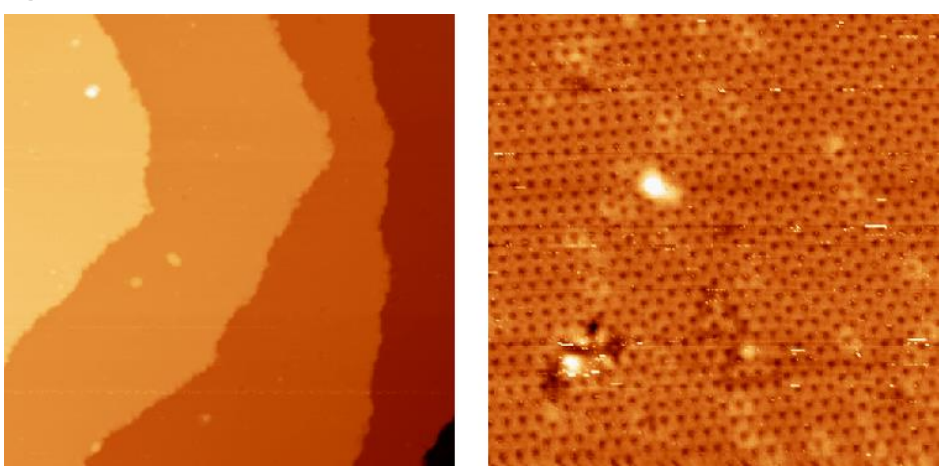

Figure 16. IBA cleaned Ge(111) Surface and c(2x8) reconstruction

Se atom was deposited on the clean Ge (111) surface using Knudsen cell. The temperature of the Ge substrate was maintained at room temperature when Se deposition process, and the amount of Se was less than 1ML. Immediately thereafter, post-annealing was performed for 30 minutes at around 300 ° C. Even if Se was sprinkled more than 1ML, only Se combined with Germanium was left after annealing, so a multi-layer structure could not be made. After post annealing, the well-ordered Se structure reveals as shown in Figure 17.

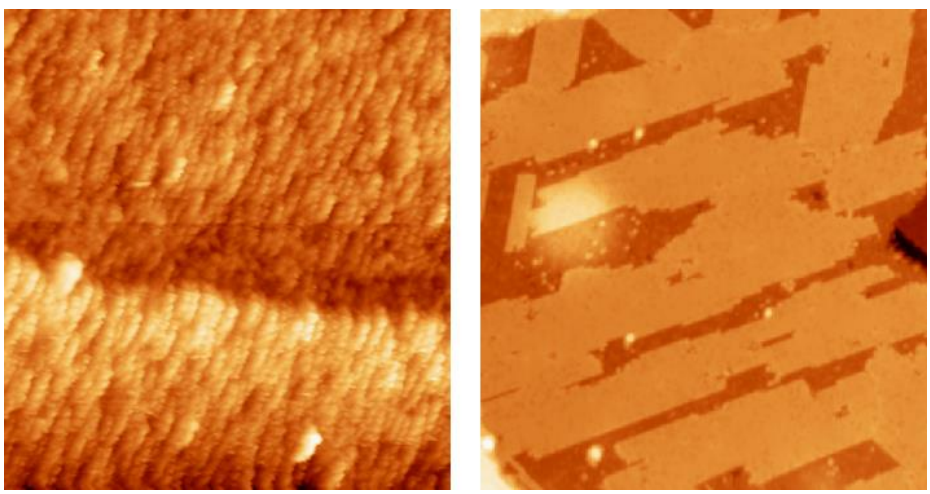

Figure 17. Before and after annealing of Se on Ge(111)

4.3. One-dimensional Se wire on Ge(111)

In our system, Se atoms were deposited on Ge(111) plane on diamond structure) substrate and self-organized in the form of islands with ordered array of wires at elevated temperature Figure 17. Even though the bare Ge(111) surface reveals a well-known c(2x8) structure[31, p. 8], after the Se wires and islands were grown, the surface of Ge(111) is unreconstructed to 1x1 structure[32]–[34] and 2x1 structures[35]–[37]. DFT based geometry optimization modeling of Se atoms on Ge substrate shows the Se island on Ge(111)

surface consists of π−bonded wires of Se atoms running in [011] direction Figure 18 c.

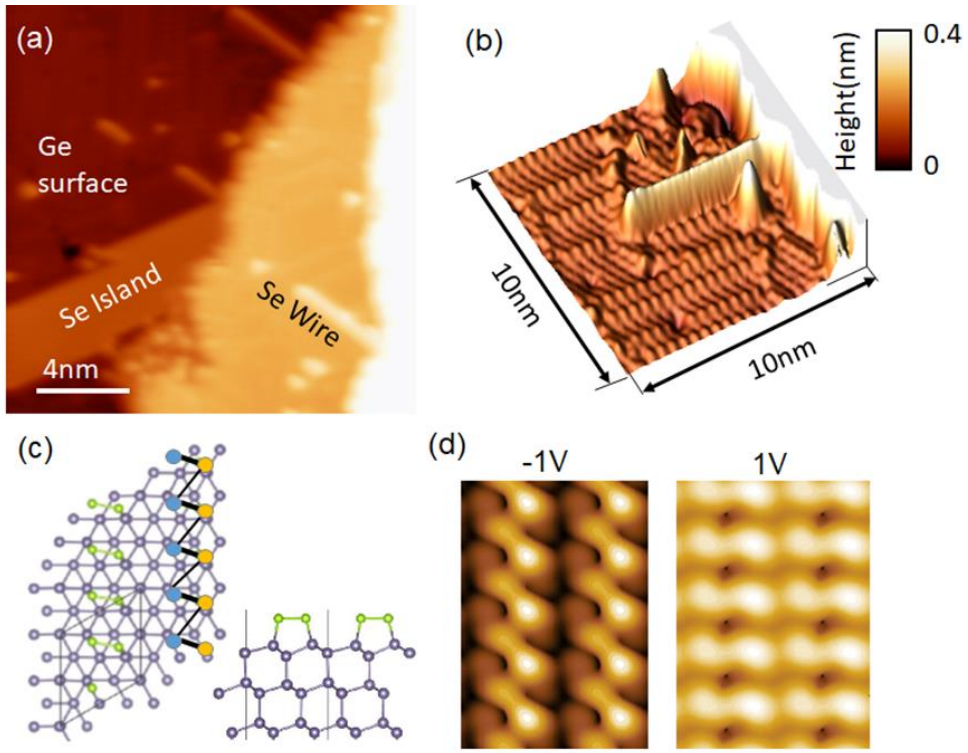

Figure 18. STM topographic images and DFT calculated result of Se on Ge(111)

Only one side of the wire row can be imaged by STM(Figure 18 a) The surface unit cell contains two Se atoms both making bonds on dangling bonds on the topmost layer of the unreconstructed Ge(111) surface respectively, and π*−bonding between the nearest two Se atoms dimerizes them. The array of wires thus form 2x1 structure with respect to Ge(111) surface. This π−bonding nature of Se wire produces a zigzag structure in the occupied states similar to the 2x1 reconstruction of Ge (111) [38]. Even though the height of two Se atoms in dimerized Se are almost the same, one Ge atom in the topmost layer bonding with a Se atom (right atom) is shifted slightly leftward direction while other topmost layer Ge atom bonding with a left Se atom is not shifted as illustrated Figure 18 c. Due to this asymmetry nature of bonding site, two atoms of the Se dimer are not

equivalent to each other. Mostly, the occupied states are localized on the light Se atom and are the same in the empty state even the ratio of the localization is different. Consequently, we mainly observe through the STM is one side of the dimer. We present high resolution STM topography image of the Se wire (Figure 18 b)on Ge substrate. A wire consists of different types with different atomic configuration. This is related to the threefold rotational symmetry of the Ge(111) surface. Since the Se wire are aligned with the three directions, and it can have three rotational symmetric types on the surface. The Ge (111) surface has mirror symmetry, from which the Se wire can also have a mirror symmetric chiral pair. Energetically preferred, island formation reveals more frequently. However, since the presence or absence of the end state is determined according to the termination of the edge of the island, analysis of the origin of the edge state of the island becomes difficult. In order to investigate origin of the edge state we grows an isolated one dimensional wire with well controlled growth condition.

Single chains are easy to understand because of their simple structure. To understand the physical meaning of the phenomena in the system, a simple modeling can help. The result that the atomic features are well visible even at large tunneling junction voltage differences and small tunneling currents compared to good metals support that the electrons on the Se wires are well localized. These features imply that the tight binding modeling can nicely explain this system. In this system, each se wire consists of an array of Se dimers. DFT results shows that hopping along the wire direction is preferred with zigzag shape in the occupied state via π−bonding. Also, bonding between the Se atoms in a dimer make strong hopping channel. Figure 19 a−b, shows the tunneling spectra of the se wire grown adjacent to the terrace. When we look at the local density of states (LDOS) of electrons according to position, we can see the gap feature on both Se wire and Ge (111). In the case of Ge (111), there is a gap between about −0.3 eV and 0.3 eV, while the Se wire has a relatively wide gap from −0.1 eV to 1.0 eV. There is an intrinsic state near 0.6eV

at Germanium substrate. Even at the middle of wire it shows a state near 0.6ev which is an intrinsic state of the Germanium due to the tunneling from vicinity of the wire which has very narrow size.

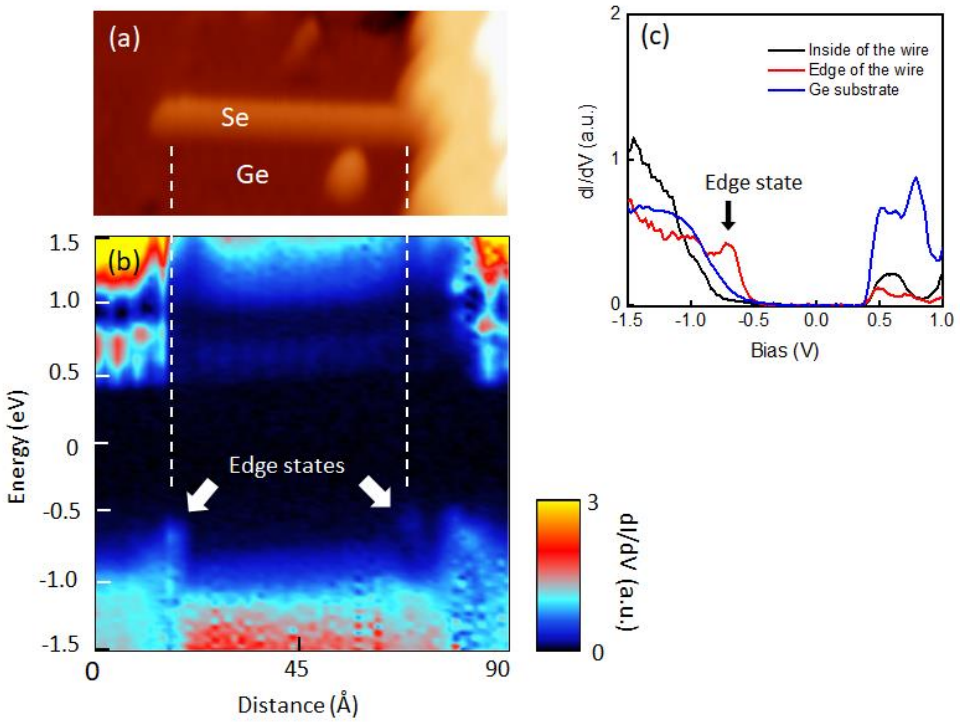

Figure 19. Positional dependent dI/dV along the Se wire.

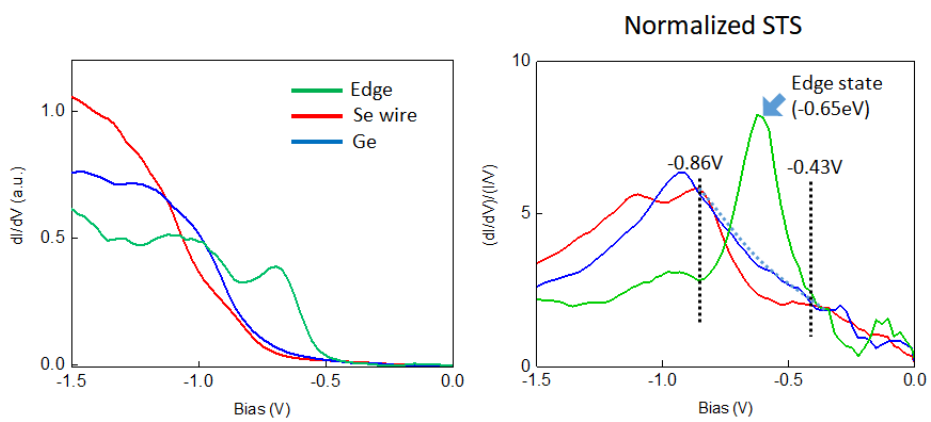

Figure 20. Subgap feature and Edge states of single Se chain on Ge(111)

Interestingly, we can see that there is a state at −0.65 eV only at Se wire edge (Figure 19 b−c). Since dI/dV is able to show both Ge and Se chain states, Ge and Se chain DOS are hybridized together at the wire edge. However, a state at −0.65 eV can be regarded as a state that is localized only at the edge because both Ge and Se chain do not have such state. It is also hard to consider this edge state in the Shockley state because of the strong localized effect of the position. As will be discussed later, due to termination nature of the wire, the Tamm state scenario is also possible.

Figure 20 shows the sub−gap feature. It is difficult to see the sub−gap directly because Ge and Se wire have low density in the filled state near the Fermi level and DOS in the background at high bias. However, when this is normalized, the sub−gap like feature can be identified from about −0.86 eV to −0.43 eV, and it can be confirmed that there is an edge state in the center. DFT simulation, but it shows the possibility that the edge state is mid−gap state.

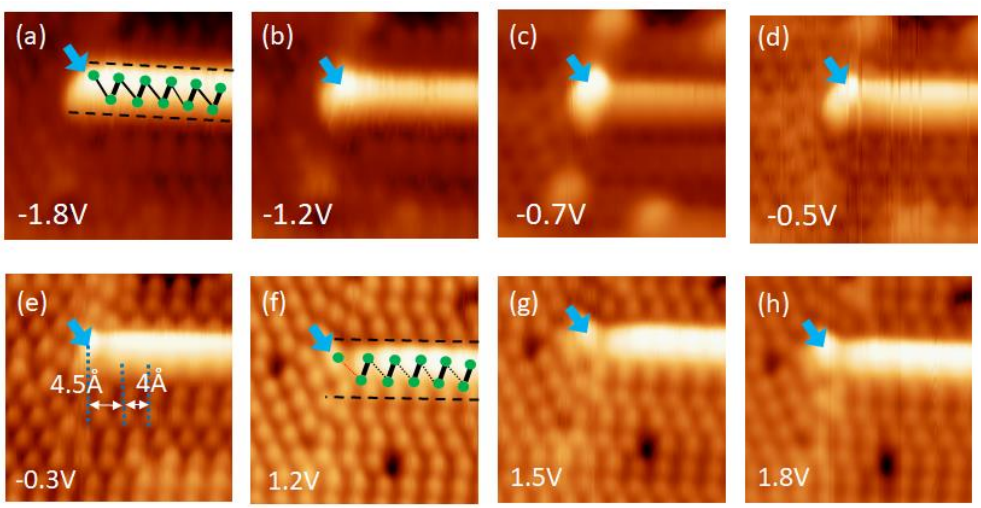

Figure 21. STM images at the end of Se wire with different bias voltage.

From the DFT results, we can think of the atomic configuration like Figure 21a from the topographic image based on the fact that one side of the chain is emphasized in STM topographic image according to chirality of the chain. In the Filled state, zigzag structure caused

by π−bonding shows a uniform height than the image in the empty state. In the empty state, the bond is formed by σ*−bonding, so well dimerized feature reveals. From the topographic images at the different bias voltage, there is no difference in the occupied state of −1.8 eV, but it can be seen that electronic density at the edge becomes larger near 0.65 eV with the edge state (Figure 21c−d). At the small bias far from the 0.65eV the edge state disappears again. An interesting thing to note in the empty state (Figure 21f−h) is that there is a node not seen in the filled state at the end of the wire, and it is possibly related with a Se monomer termination. Therefore, the topographic feature at the end of the wire shows smaller sized feature than the other dimerized Se atoms in the chain, The Se atoms in the chain are bonded to the germanium and the nearest Se atoms, so that the isolated Se atoms at the end of the wire only bonds with the topmost Ge atoms. From the result of the atomic configuration shown in Figure 18c, if the Se atom makes bonding with 2 topmost Ge atoms, it goes farther away from the next−terminated Se dimer(Figure 21e). Empty states have σ*−bonding nature and electron density tends to become localized to the dimer, so the electron density between the atom and the chain is gets smaller if the atomic distance gets farther. Hybridization among reconstructed Ge atoms also serves to reduce bonding with the chain. This reduced electron density between the atom and the chain makes a node. On the other hand, the reason why the isolated form from the image of the filled stat is not clearly seen is that the filled state has larger hopping between the dimers due to the π−bonding. This π−bonding nature delocalize the electron and make electron in the chain able to well hop with terminated atoms, so the chain reveals uniform feature. From this it can be seen that the termination of the wire differs from the configuration in the chain. This termination effect also can be seen the other side of edge Figure 22, thus we can think the edge termination of the wire is symmetric.

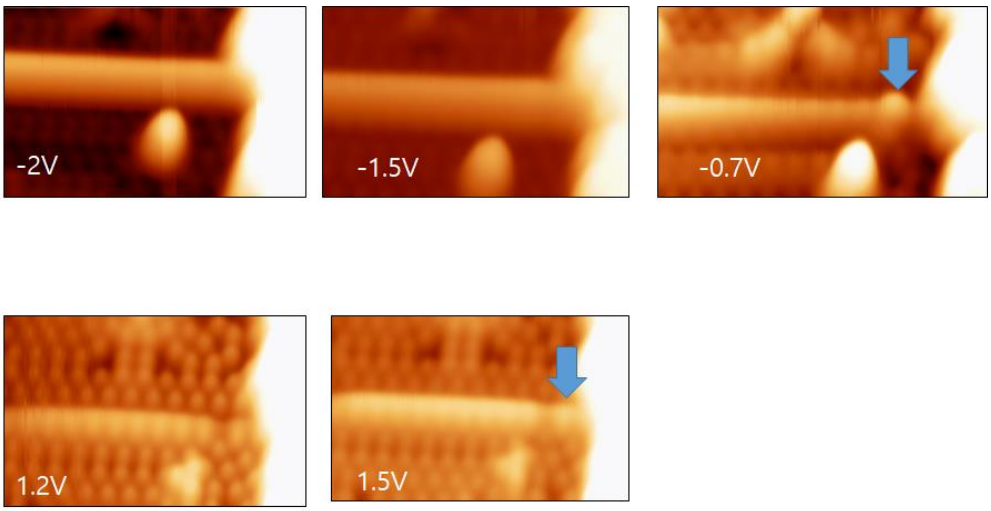

Figure 22. STM images at the opposite end of Se wire with different bias voltage.

4.4. Se island on Ge(111)

The selenium atoms grown on Ge (111) are self-assembled on Ge (111) and have an array form of the chain as shown in Figure 23. The arrangement of the se atoms at this time is not different from the single line mentioned above. However, this island has various domain nature. An island consists of different type of domain with different atomic configuration. This is related to the threefold rotational symmetry of the Ge(111) surface. Since the Se wires in each domain are aligned with the same direction, a domain can have three rotational symmetric types on the surface. The Ge (111) surface has mirror symmetry, from which the Se wire can also have a mirror symmetric chiral pair. Energetically preferred, each domain has only one phase. Thus, in addition to inter-chain interaction is very weak in that there is only weak bonding between two chains, its nature is almost the same with one-dimensional chain.

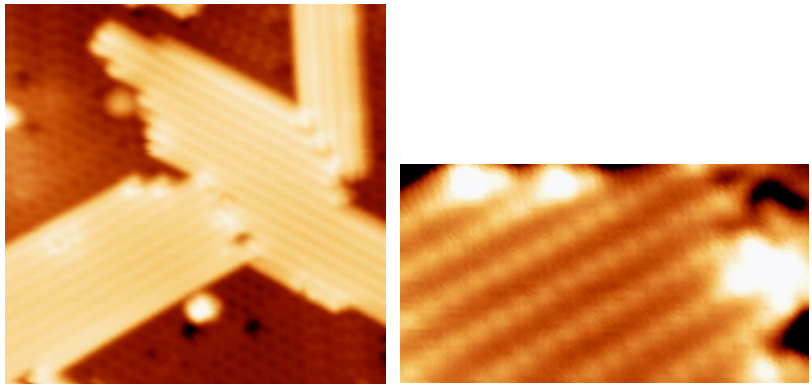

Figure 23. STM topographic image of Se island on Ge(111)

With functionalized tip we can see detailed feature of the Se island Figure 24. This functionalized tip make it easier to see beyod the se chain. This functionalized tip shows the characteristics of the substrate disregarding Se state. The brightest part of the atomic image shown below is highlighted at the center of the chain, along the center of the chain, with the topmost atoms of Ge highlighted brightly.

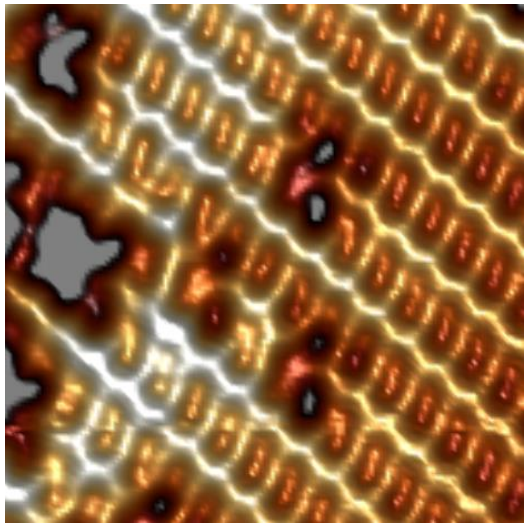

Figure 24. Atomic image of Se/Ge(111) with functionalized tip

Selenium is missing from the above image where the hole like parts in the STM topographic image. It is easy to see that if the dimerized Se is missing from the DFT result, it looks like the following feature, also it fits well with DFT calculated result, so that the hole like shape

is tilted with respect to wire direction. There are a deeper hole and a lesser hole part, and the deeper part is the higher electron density in the original chain. Therefore, when an atom is missing, it appears to be deeper effectively. This result shows that the DFT calculation is well validated.

To observe the electronic structure of the Se island, the tunneling spectra were observed near the Se island. (Figure 25). We measured the positional local density of states (LDOS) along the direction from the Se island to the Ge (111) substrate. LDOS shows a broad band gap on the Se island from −0.1 eV to 1.0 eV. This is because the Se island shows an semi conducting property like Se wire. When we go over Ge (111), we can see that the band gap of Ge spans about −0.3 eV to 0.3 eV. In particular, Germanium has a state near 0.7 eV, which is also the same as seen in the previous one-dimensional Se wire result.

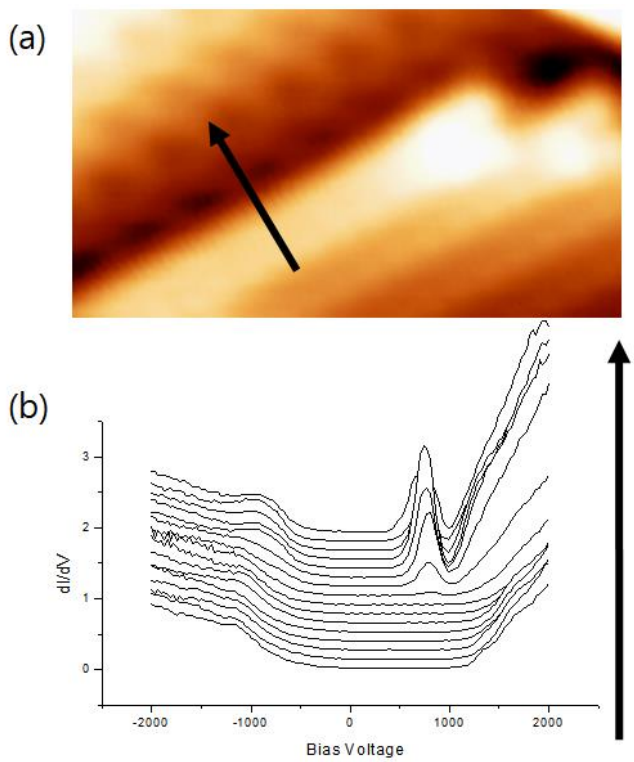

Figure 25. Position dependent tunneling specta on Se island Ge(111) surface

We could see a peculiar atomic structure near the domain boundary. (Figure 26) However, when it is assumed that this is not dispersive, it can be seen that the near structure has changed due to the atomic structure of the domain boundary. Interestingly, in the case of a specific defect in the island, a symmetric shape appears at both edges, and this state is dispersively dispersed to the periphery. More research is needed to see if this is a topological effect.

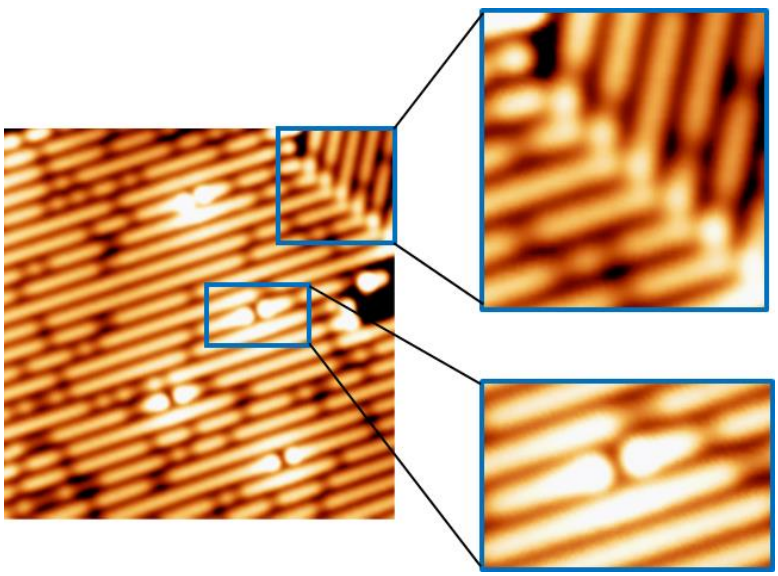

Figure 26. Edge state around domain boundary and defects

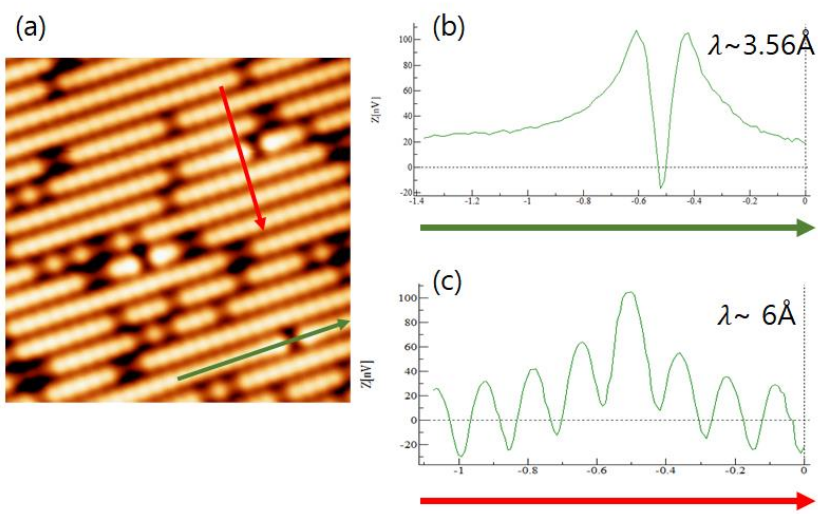

Figure 27. Decay length of the edge state measurement on Se wires

4.5. DFT calculation of the system

4.5.1. Geometry Optimization

Geometry optimization is the name of the process of finding a configuration of atoms with the minimum energy. A reasonable starting point for geometric optimization is the use of experimental data, i.e. STM topographic data of the atoms. The energy and wave functions are computed for the initial guess of the geometry, which is then modified iteratively until (I) an energy minimum has been identified and (II) forces within the atoms are zero. This can often be difficult for some cases, where there may be several energy minima, and some effort may be required to find the global minimum. But in those cases where atoms have unknown or unconfirmed structures, geometry optimization can also be used to locate minima on a potential energy surface and can predict the equilibrium structure of the atoms in question.

The geometry optimization calculations were done with the VASP[39], using the density functional theory in the generalized gradient approximation(GGA). Based on PBE pseudo potential, we performed to simulate several examples.

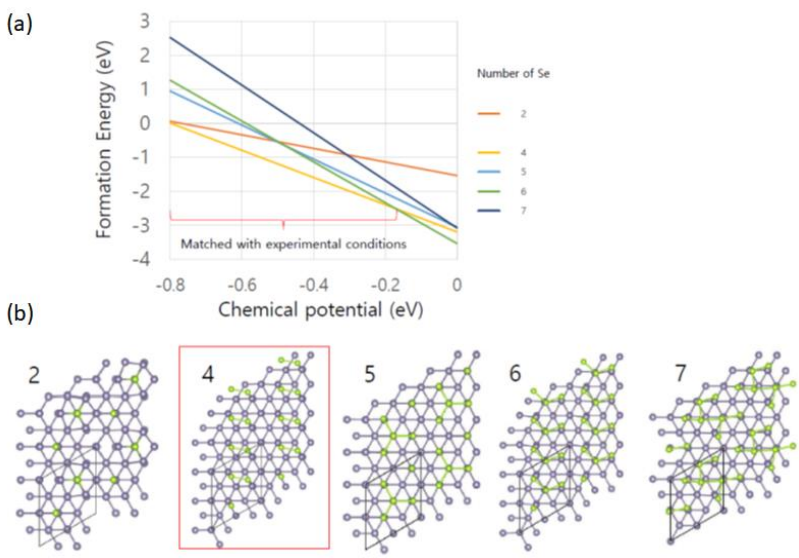

Figure 28. DFT based formation energy calculation of representative candidates

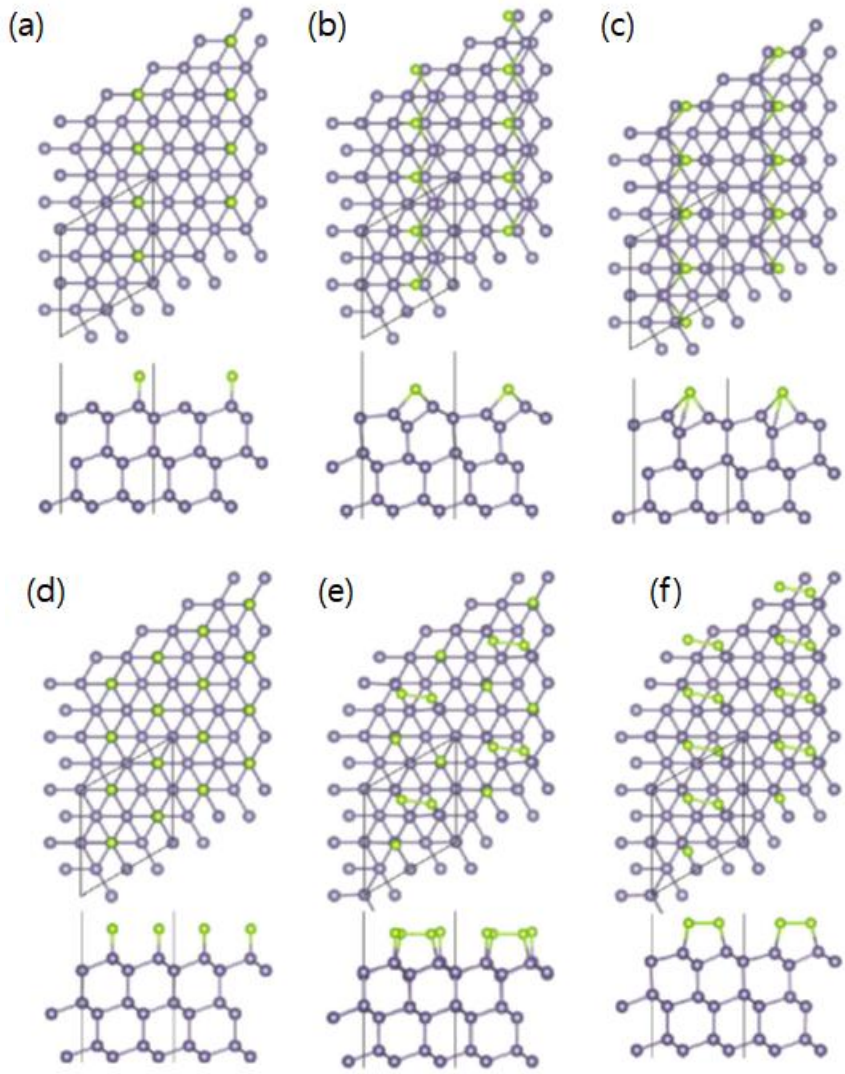

Figure 29. DFT based geometry optimization calculation of Se atoms on Ge(111) surface.

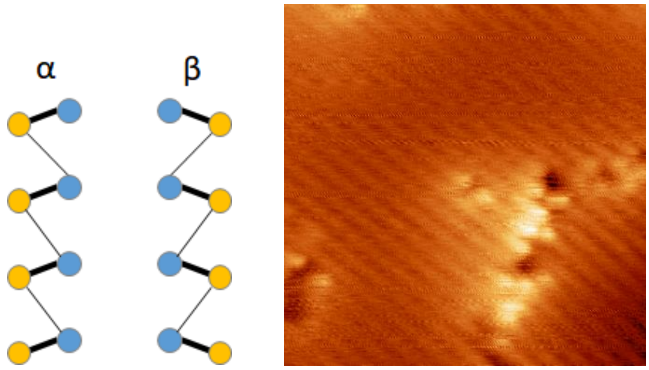

Figure 30. Chirality of a Se wire and Chiral boundary STM image

There are two possible chiralities (α and β). The α wire has right-hand chirality which is a mirror symmetric pair of β wire (left-hand chiral).

4.6. Modeling and Simulation

4.6.1. One-dimensional wire calculation

We used tight binding simulation to determine which types of edge state this wire termination can give. Based on the SSH model, a total of 50 atoms were calculated. As shown in Figure 31a, hybridization with a Ge substrate results in the hopping of the isolated atom with α, and the deformation of the hopping in the next terminated dimer is considered. In the chain, the inter-dimer hopping constant is set to t_1 and the intra-dimer hopping constant t2. The absolute values of t_1 and t_2 are arbitrarily set because they only determine the size of the gap.

Since the strength of the bonding at the edge part changes, the hopping constant at the edge part is set to α at the first termination edge and to β at the second termination edge. Figure 31a illustrates this SSH model. Because we do not know the exact hopping constant of the system, dimensionless values are needed to interpret topological properties. Therefore, the α and β defined near the edge are expressed by introducing the dimensionless ratio λ_α and λ_β for t_1 and t_2, respectively. When there is local disorder in the edge

part, the topological phase transition according to λ_α and λ_β is examined while changing the values of t_1 and t_2.

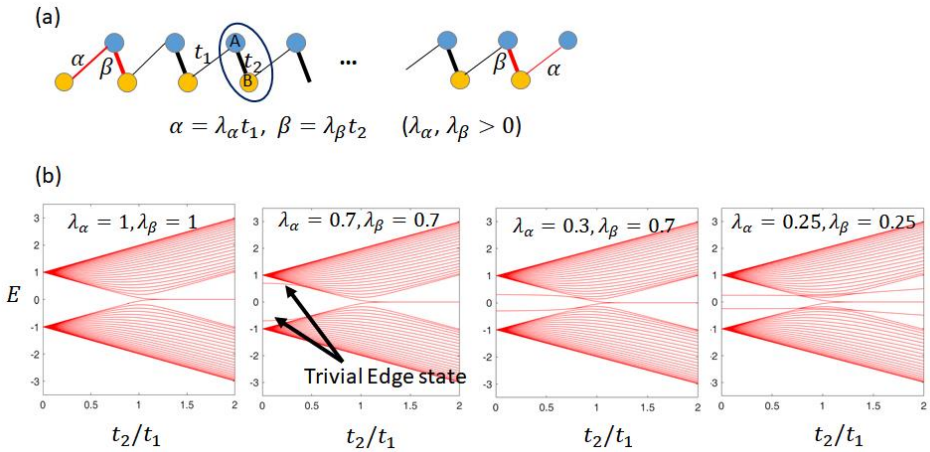

Figure 31. Tight binding calculation of Se wire

Topological phase transition refers to the phase transition that occurs when the system's Hamiltonian is adiabatically changed, but the symmetry of the system is maintained but the topology changes. The leftmost figure in Figure 31b shows the topological phase transition in a typical SSH model.

In this case, the termination bonding becomes t_1 because $\alpha = t_1$ and $\beta = t_2$. If we look at the energy eigenvalue while changing the ratio of t_1 to t_2, we can see that t_1 begins to become smaller than t_2 and a new state exists in zero energy. When $t_1 < t_2$, a topological phase transition occurs, resulting in a new topological phase with an edge state. Interestingly, this always appears, regardless of the value of λ_α and lambeta. If λ_α and λ_β are not 1, an edge state is generated, but occurs in energy other than zero, and zero bound state occurs only in $t_1 < t_2$. In the case of $\lambda_\beta < t_1/t_2$, we can see that not only zero energy edge state but also edge state occurs in other energy and coexist with each other.

If we see the eigenstate at this time, we can see that it is as shown in Figure 30. The zero-energy edge state is generated at the second termination edge and the non-zero energy edge state is at

the edge of the chain. In this case, the atoms in the chain end are isolated due to weak bonding, creating a separate state, and the topological edge state in the remaining chain. In this way, even if local distortion occurs in the chain, calculation of the Zak phase is necessary to determine whether the zero-energy edge state generated in this system is a topological non-trivial case or a trivial case. If the system is a topological trivial, the Zak phase is zero, but if it is non-trivial, it is π.

When we calculate the Zak phase of this system, the Zak phase has π and the Zak phase has zero regardless of the system termination when $t_1 < t_2$. This suggests that if the symmetry is not broken (the chiral symmetry is preserved in this system), a topological protected edge state may occur, and this may result in an edge state because it is also robust to local disorders. From the result of this phase transition, we find that the edge state in zero energy is topological. From this model Hamiltonian, we can see that the edges of this system can have topological behavior, even though the local disorder is on the edge, and that the termination of the chain is far from the chain. This means that the edge state in this system can be interpreted topologically despite differences from the model.

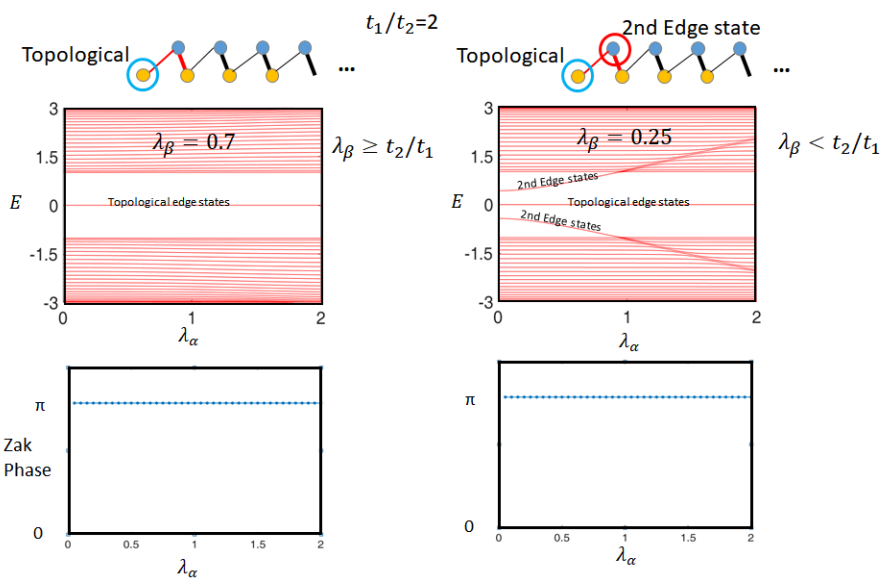

Figure 32. Second termination edge state and Zak phase

4.6.2. Se island calculation and analysis

To understand the physical meaning of the phenomena in the Se island system, a simple modeling can help. This system has an insulating nature as seen in the tunneling spectroscopy result in the previous chapter. Moreover, the result that the atomic features are well visible even at large tunneling junction voltage differences and small tunneling currents compared to good metals suggests that the electrons on the Se wires are well localized. These features imply that the tight binding modeling can nicely explain this system. In this system, each se wire consists of an array of Se dimers.

Each dimer makes a hopping channel in the direction along the wire and perpendicular to it. DFT results shows that each dimer can easily hop in the direction perpendicular to the wire in the unoccupied state but hopping along the wire direction is preferred with zigzag shape in the occupied state. In the occupied state, staggered hopping occurs in the wire direction and inter-chain hopping occurs uniformly in the direction perpendicular to the wires. Generally, an island is considered to have a single chirality over the whole area, the toy model as shown in Fig. can be introduced. In this model, each dimer has an intra-dimer hopping constant t_2 and a inter-dimer hopping t_3 which is weaker than former. And each chain is connected through inter-chain hopping t_1 which is the smallest hopping constant among three.

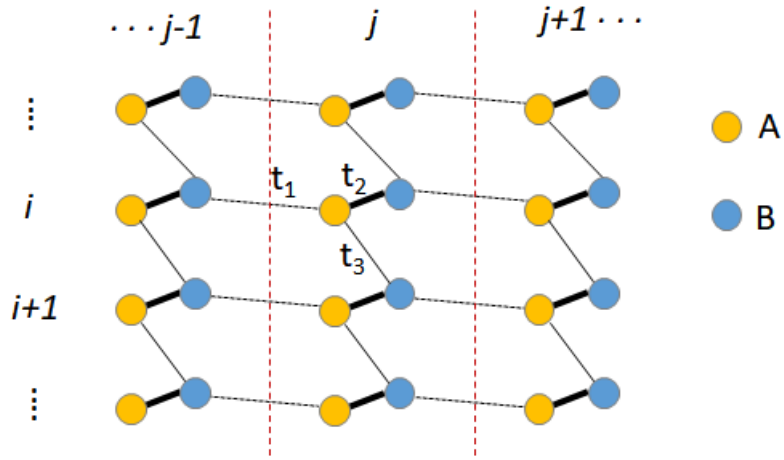

Figure 33. Toy model of Se island on Ge(111)

Each island consists of an array of Se wires with the same chirality.

From above model, each se atom in the dimer in the i−th row and j−th column can be divided into A and B sub cell site because each site has translation symmetry, so they can be indexed as A(i,j) and B(i,j). Without regarding onsite coulomb potential which only can contribute chemical potential offset of this system, one band model Hamiltonian can be represented as

$$\mathcal{H} = \sum_{i,j} \Psi_{i,j}^{\dagger} U \Psi_{i,j} + \Psi_{i,j}^{\dagger} V \Psi_{i,j+1} + \Psi_{i,j}^{\dagger} V^{\dagger} \Psi_{i,j-1}\,, \qquad (24)$$

where $\Psi_{i,j} = \begin{pmatrix} \psi_{A(i,j)} \\ \psi_{B(i,j)} \end{pmatrix}$, $U = \begin{pmatrix} 0 & t_1 \\ t_1^* & 0 \end{pmatrix}$ and $V = \begin{pmatrix} 0 & t_2 \\ t_3^* & 0 \end{pmatrix}$, with Wannier function $\psi_{A(i,j)}$ and $\psi_{B(i,j)}$ for each site A(i,j) and B(i,j). Due to translation symmetry, Wannier function of A site is $\psi_{A(a,j)} = \psi_{A(b,j)} e^{ik(b-a)R}$, likewise B site. Thus this Hamiltonian can be reduced as

$$\mathcal{H} = \mathrm{n_i} \left(\sum_{j} \Psi_j^{\dagger} U \Psi_j + \Psi_j^{\dagger} V \Psi_{j+1} + \Psi_j^{\dagger} V^{\dagger} \Psi_{j-1} \right) \qquad (25)$$

where, $\Psi_j = \begin{pmatrix} \psi_{A,j} \\ \psi_{B,j} \end{pmatrix} = \begin{pmatrix} \psi_{A(1,j)} \\ \psi_{B(1,j)} \end{pmatrix}$ and $\mathrm{n_i}$ is the number of rows. This Hamiltonian can readily be transformed to Hamiltonian in one dimensional k−space,

$$\mathcal{H} = \int_0^{2\pi} \frac{dk}{2\pi} \left(\Psi^{\dagger}(k) H(k) \Psi(k) \right) \tag{26}$$

where, $H(k) = \begin{pmatrix} 0 & h(k) \\ h^*(k) & 0 \end{pmatrix} = \begin{pmatrix} 0 & t_1 + t_2 e^{ik} + t_3 e^{-ik} \\ t_1^* + t_2^* e^{-ik} + t_3^* e^{ik} & 0 \end{pmatrix}$

and $\Psi(k) = \begin{pmatrix} \psi_A(k) \\ \psi_B(k) \end{pmatrix}$.

From above equation, we can think of this system as equivalent to 1D system. For an edge state to occur at E = 0, we need to satisfy

$$\Psi^{\dagger} H^{\dagger} H \Psi = H^2 = E^2 = 0$$

because, $H\Psi = E\Psi$.

Since $q = e^{ik}$ must set and $h(k) = 0$ must be made from $H^2 = 0$, it becomes

$$t_1 + t_2 e^{ik} + t_3 e^{-ik} = t_2 q^2 + t_1 q + t_3 = 0 \tag{27}$$

From this equation, end state of site A only exist when $|q_{1,2}| < 1$ (Im [k] >0),because of boundary condition $\psi_{A,0} = \psi_{B,0} = 0, \psi_{A,\infty} = \psi_{B,\infty} = 0$. Based on this Hamiltonian, I tried simulation using MATLAB. When we calculate 12x48 atom sites, we can see the result like Figure 34.

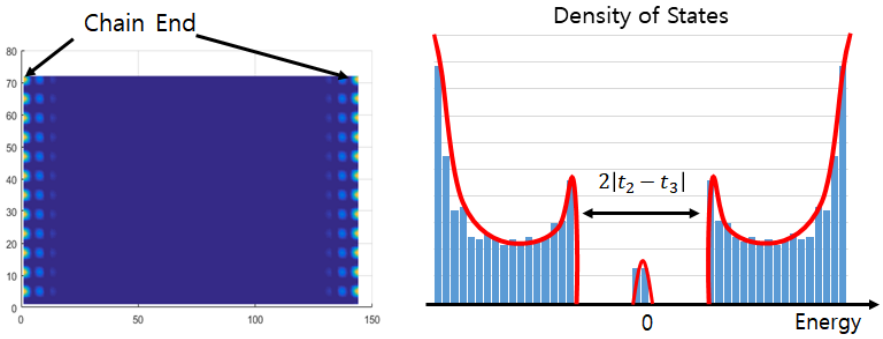

Figure 34. MATLAB simulation result of edge state of Se wires and calculated density of states

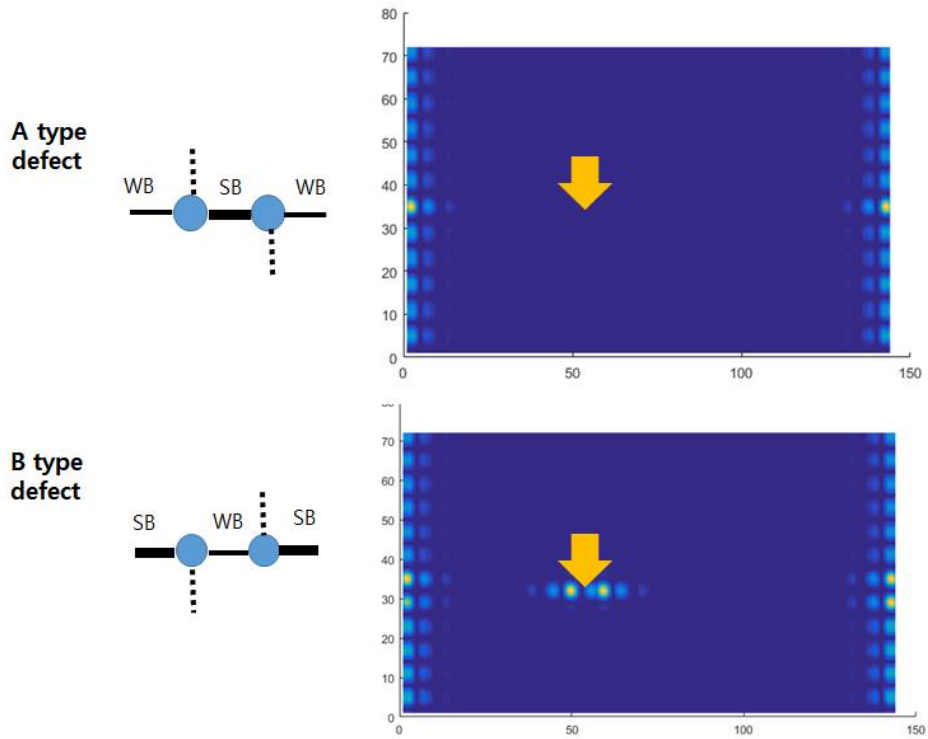

Figure 35. Simulation result of defect induced edge state of Se wires at different dimer defect

The peak of density of state can be seen at zero bias when calculated with tight junction. When the Eigenstate corresponding to this Eigen value is simulated, the result is shown on the left side of Figure 34, and it can be seen that the state occurs at the edge of the multiple chain. In order to explain the defect state shown in Figure 26, simulation was performed according to the defect type. In the case of the monomer defect, only one state appears in the form of appearance of the state. Therefore, two types of dimer defects were considered. As shown in Figure 35, the dimer was calculated as a B-type defect consisting of a weak bond between a dimer defect (A type defect) and a dimer (strong bond) between dimers. As a result, the edge state does not appear in the A-type defect and the edge state symmetrically in the B-type defect.

Typical A-type defects are easier to generate due to weaker bonding to the periphery than B-type defects in energy, which supports that there are more defects without edge state in Fig. However, in the case of B-type defects, the frequency of formation is high because of the high formation energies, which can demonstrate that the edge state has fewer defects on both sides. However, since this defect is hardly physically generated, the possibility of a scenario concerning B-type defect is low. Rather, we can think of the defect of the Ge (111) surface atom bonding with the Se dimer. When a Ge (111) surface atom defect is generated, the Se dimer does not have a site for bonding. Therefore, it does not make an edge state like a type A defect. However, due to the absence of Ge (111), a defect induced doping effect is produced in Se / Ge (111), which can be interpreted as creating a state around the edge as well.

4.7. Discussion

One dimensional Se chain can grow in one-dimensional wire form on Ge (111) surface. Due to the symmetry of the bond between the Ge (111) surface atom and the Se atom, this Se wire is in the chain form of an array of Se dimers. Therefore, the hopping in the intra-dimer is large and the inter-dimer hopping is in the form of staggered hopping consisting of tunneling. When not considering the hybridization through the Ge (111) surface, this can be expressed as an SSH model. Due to the termination of the Se wire, an edge state can occur. The following scenario can be considered.

1. Charge state: It is the state that the state makes on the Se wire because of the charging due to the state at the end side. Charge state analysis cannot interpret that Ge's Fermi level does not go up around the edge of the Se wire.

2. Dangling bond: Dangling bonds can act as an orbital state that does not charge Ge (111). However, since the dangling bond of the

Ge (111) surface is not terminated, it has a dangling bond as a whole. Therefore, it is difficult to interpret that only the dangling bond at the end of the wire has a state.

3. Isolated atomic state: There is a state which is caused by an independent Se atom. For this to be established, the distance between Se atom and Se wire must be larger than the Thomas-Fermi screening length, and even if only a little hopping exists, it can be interpreted by edge reconstruction.

4. Edge reconstruction: In trivial case, it is a state that occurs because the symmetry at the edge changes in the general chain. It is a state that can occur even if the symmetry is broken and the bonding is weak, and it may exist if only the hopping with the wire exists.

5. Topolgical state: It is a state caused by the topology of the system. Se Chain is a scenario that you can think of because it has staggered hopping nature.

From the experimental data, potential scenarios are edge reconstruction and topological state. However, these two cannot be distinguished from the experiment through STM. To distinguish whether the edge is topological or trivial, it is important that the Hamiltonian of the system is topological trivial or non-trivial. If the Hamiltonian of the system is non-trivial, this edge state can be interpreted as topological. If it is a trivial, this state is interpreted as edge-reconstruction. Through the tight binding calculation, we can see that the topology of the whole system is maintained even if the edge has local distortion. We could see that this system is a topological edge state. However, considering the role of hybridization with the Ge substrate, it is necessary to take a closer look at the DFT calculation.

5. Thin Film High-Tc Superconductor: FeSe on $SrTiO_3$(100)

5.1. Introduction

Since the discovery of H.K. Onnes in 1911, much research has been done on superconductors. Superconductors are a representative example of quantum phenomenon ocurring in the macroscopic system and are being studied steadily because of their exotic characteristics. Superconductors are materials with the following properties,

1. Perfect conductor – no electric field in the material because it has zero resistance
2. Perfect diamagnetism – there is no magnetic field (B = 0) inside, which is one way to distinguish a superconductor from a perfect conductor.

5.1.1. Phonon mediated Superconductivity (BCS theory)

The first successful theoretical approach to the mechanism of superconductivity was proposed by Bardeen, Cooper and Schrieffer in 1957. Cooper suggested that in 1956, two electrons could make a bound state due to an attractive force (Cooper pair), the next year Bardeen, Cooper and Schrieffer suggest that phonons can create Cooper pairs by giving an effective attractive force between the electrons and explain the superconductivity in the solid. According to the equation, Hamiltonian of superconductor system can be represented by second quantization form which is

$$\mathcal{H} = \sum_{\vec{k}\sigma} \varepsilon_{\vec{k}} c^{\dagger}_{\vec{k}\sigma} c_{\vec{k}\sigma} + \sum_{\vec{k}\vec{k}'} V_{\vec{k},\vec{k}'} c^{\dagger}_{\vec{k}'\uparrow} c^{\dagger}_{-\vec{k}'\downarrow} c_{-\vec{k}\downarrow} c_{\vec{k}\uparrow} \qquad (28)$$

, where $V_{\vec{k},\vec{k}'}$ is interaction potential. This Hamiltonian does not include any explicit term involving electron-phonon interaction. While it will be dealt in the next chapter, this degree of freedom for selecting an interacting potential means that any electron-electron

interaction can be a candidate to make a Cooper pair, even without a phonon mediated interaction, and create superconductivity. More precisely, this expression is for describing a singlet cooper pair (s−wave or d−wave), so for a superconductor such as a p−wave or an f−wave, the spin part in the second term is modified. For a conventional superconductor in which phonon mediated pairing dominates, $V_{\vec{k},\vec{k}'}$ can be represented as,

$$V_{\vec{k},\vec{k}'} = V_{\vec{k},\vec{k}+\vec{q}} = \sum_j \left|g_{\vec{q}j}\right|^2 \frac{2\hbar\omega_{\vec{q}j}}{\left(\varepsilon_{\vec{k}+\vec{q}} - \varepsilon_{\vec{k}}\right)^2 - \hbar^2\omega_{\vec{q}j}^2} \tag{29}$$

, where $g_{\vec{q}j}$ and $\omega_{\vec{q}j}$ are electron−phonon coupling constant and phonon frequency with momentum of phonon $\vec{q}$ in j−th mode, respectively.

In order to solve Equation (28), one can use mean field approximation or the variational principle. In this paper, the mean field approximation is going to be used. We can denote second term of the Equation (6) with mean field approach,

$$\mathcal{H}_{\text{pair}}^{\text{eff}} = \sum_{\vec{k}\vec{k}'} V_{\vec{k},\vec{k}'} \left(\langle c_{-\vec{\mathrm{k}}\downarrow} c_{\vec{\mathrm{k}}\uparrow} \rangle c_{\vec{k}'\uparrow}^{\dagger} c_{-\vec{k}'\downarrow}^{\dagger} + \langle c_{-\vec{k}'\downarrow} c_{\vec{k}'\uparrow} \rangle^{*} c_{-\vec{\mathrm{k}}\downarrow} c_{\vec{\mathrm{k}}\uparrow} \right) - \text{const} \tag{30}$$

For a simplification, we can define,

$$\Delta_{\vec{\mathrm{k}}} \equiv -\sum_{\vec{k}'} V_{\vec{k},\vec{k}'} \langle c_{-\vec{k}'\downarrow} c_{\vec{k}'\uparrow} \rangle \tag{31}$$

Having collected the terms from Equation(30) and dropping the constant, we obtain the result of the quadratic effective Hamiltonian

$$\mathcal{H}_{\text{pair}}^{\text{eff}} \approx -\sum_{\vec{k}} \left(\Delta_{\vec{\mathrm{k}}} c_{\vec{k}\uparrow}^{\dagger} c_{-\vec{k}\downarrow}^{\dagger} + \Delta_{\vec{\mathrm{k}}}^{*} c_{-\vec{\mathrm{k}}\downarrow} c_{\vec{\mathrm{k}}\uparrow} \right) \tag{32}$$

Now the total Hamiltonian becomes $\mathcal{H} = \mathcal{H}_{\text{K.E.}} + \mathcal{H}_{\text{pair}}^{\text{eff}}$ and this Hamiltonian can be diagonalized using the Bogoliubov de Gene (BdG) Transform by defining the creation and annihilation operator of BdG quasiparticle,

$$\begin{aligned} \gamma_{\vec{k}\uparrow} &= u_{\vec{\mathrm{k}}} c_{\vec{\mathrm{k}}\uparrow} - v_{\vec{\mathrm{k}}} c_{-\vec{k}\downarrow}^{\dagger} \\ \gamma_{\vec{k}\downarrow} &= u_{\vec{\mathrm{k}}} c_{\vec{\mathrm{k}}\downarrow} + v_{\vec{\mathrm{k}}} c_{-\vec{k}\uparrow}^{\dagger} \end{aligned} \tag{33}$$

The total Hamiltonian is diagonalized as

$$\mathcal{H} = \sum_{\vec{k}\sigma} \mathrm{E}_{\vec{\mathrm{k}}} \gamma_{\vec{k}\sigma}{}^{\dagger} \gamma_{\vec{k}\sigma} \tag{34}$$

The free electron energy is defined as $\varepsilon_{\vec{k}}$ according to equation (28). Using equation (34) it is easy to derive the relation between electron energy eigenvalue $\varepsilon_{\vec{k}}$ and quasi-particle energy Eigen value $\mathrm{E}_{\vec{\mathrm{k}}}$.

$$\mathrm{E}_{\vec{\mathrm{k}}} \left(u_{\vec{\mathrm{k}}}^2 - \left| v_{\vec{\mathrm{k}}} \right|^2 \right) = \varepsilon_{\vec{k}} \tag{35}$$

By comparing with equation (32) we can get,

$$2 u_{\vec{k}} v_{\vec{k}} = \frac{\Delta_{\vec{k}}}{E_{\vec{k}}} \tag{36}$$

Finally we can get relation,

$$\mathrm{E}_{\vec{\mathrm{k}}} = \sqrt{\varepsilon_{\vec{k}}^2 + \left| \Delta_{\vec{k}} \right|^2} \tag{37}$$

Solving this equation more, we can get following result as depicted Figure 36.

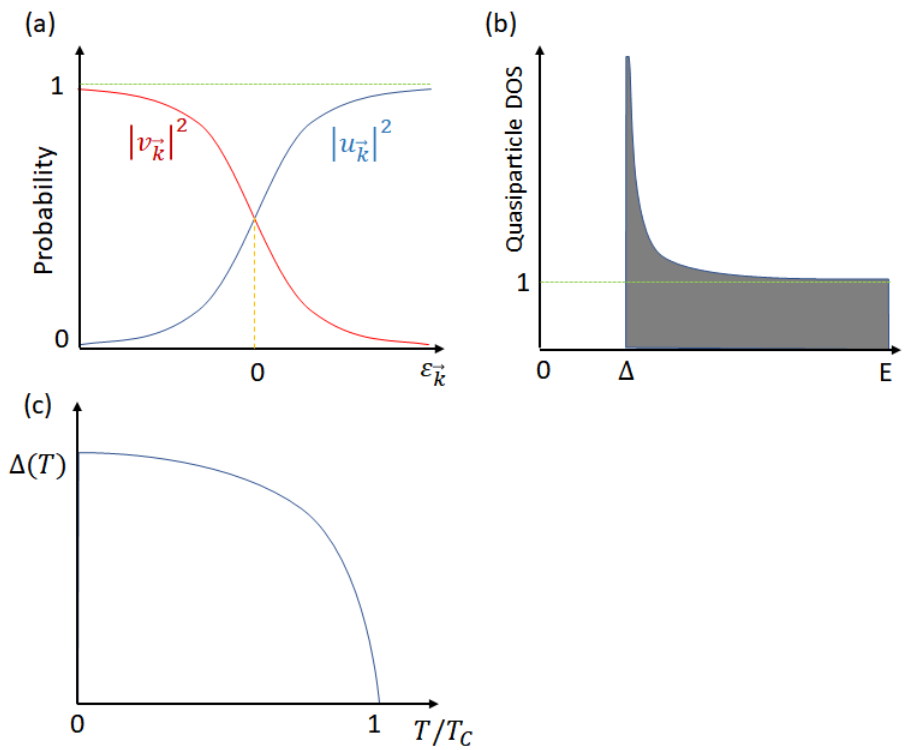

Figure 36. Properties of BCS superconductors

(a) comparison of coherence factors, (b) quasiparticle DOS (c) Δ vs T dependence

5.1.2. Unconventional superconductivity.

Eliashberg theory evolved the concepts of BCS theory and extended it to the strong coupling regime [19]. So many researchers would expect other superconductors to be explained based on the BCS theory. More they thought that the superconductivity phenomenon was explained in general. However, in 1986, J. G. Bednorz and K. A. Muller found superconductivity in a ceramic-based copper-oxide layer ($Ba_xLa_{5-x}Cu_5O_{5(3-y)}$) [40], bringing the superconducting system to a new phase. This discovery was revolutionary, firstly, that superconductivity appeared in ceramic-based insulating materials, and secondly that the electron-phonon coupling of BCS theory could not explain its critical temperature of 30K. Superconductivity was observed in other materials of the copper-oxide family, and the discovery continued, and the critical temperature reached 475K at present $Sn_{11}SbTe_{10}Ba_2VMg_{23}O_{46+}$ [41]. Since the critical temperature is higher than that of the elemental superconductor, they are called high-temperature superconductors.

Although high-temperature superconductors have not been described in the BCS theory and Eliashberg theory, researchers still agree that this unconventional superconductor will also exhibit superconductivity due to Cooper pairing. However, there are various hypotheses as to which bosonic mode other than phonon acts as a mediator of pairing. This situation is the same in heavy fermions discovered in 1979 [42] and in iron pnictides discovered in 2008 [43].

After the copper oxide series, another series of high-temperature superconductors began to be discovered, iron pnictides ($LaFeAsO_{1-x}F_x$, 2008 in Hosono group [43]). This discovery was also revolutionary because of iron. According to conventional superconductivity, the magnetic moment only serves to break superconductivity. In fact, superconductivity is broken when a small amount of magnetic atoms are placed in a conventional superconductor. According to Eliashberg theory, $LaFeAsO_{1-x}F_x$ has

a relatively small electron−phonon coupling constant and the expected Tc is only 0.8K. However, the actual measurement reached 26K. The discovery beyond this common sense and the impossibility of explaining it with existing theories was another opportunity for the scientific community to produce numerous theories and experiments with myriad discoveries and challenges.

The most promising scenario is Cooper pairing by spin fluctuation. The phase diagram of Fe pnictide shows antiferromagnetic or spin density wave in the absence of electron or hole doping. And as the magnetic phase disappears, the superconducting phase appears adjacent. In addition to this indirect evidence, one research supporting this scenario have been published [44]. They compared the optical measurement of Ba $(Fe_{1-x}Co_x)_2As_2$ with that of inelastic magnetic neutron scattering by Eliashberg theory and found that the spin fluctuation is strongly coupled with the electron in that system.

Another difference between unconventional superconductors and conventional superconductors is the symmetry of order parameters. Conventional superconductors have isotropic s−wave gap symmetry because S = 0 and L = 0. As a result, we have the quasiparticle density of state of fully−gapped form of U−shape. However, Cuprate (coper−oxide) has d−wave symmetry because it is spin singlet (S = 0) and L = 2. Thus, since the gap symmetry is not isotropic, and the quasiparticle density of state is represented as the average value in all k directions, it has a V−shape in this case. In the case of Fe−based superconductor, s + − symmetry is proposed and verified through many experiments. The gap parameter is isotropic but the sign at the Gamma point and at the M point are different. Depending on whether the fermi surface passes through two pockets of different sign, it is either a V−shape gap or a U−shape gap.

Unconventional superconductors have been studied mainly in copper oxide series and Fe pnictide series. Many experiments and scenarios have emerged because existing theories do not fit well, but they implicitly agree that Cooper pairing will occur through other mechanisms.

5.2. Electron–Boson interaction

5.2.1. Eliashberg Theory

In crystals, atoms are in lattice form. This lattice consists of a combination of ion cores, which vibrates mechanically in the equilibrium position when energy is not given when energy is given. If the displacement of this vibration is small enough, the vibration of this ion core can be approximated by a simple harmonic oscillation, and the energy eigenvalues are quantized according to the quantum mechanics.

If the displacement of this vibration is small enough, the vibration of this ion core can be approximated by a simple harmonic oscillation, and the energy at this time is quantized according to the quantum mechanics. In quantum mechanics, there is second quantization method to treat collective excitation in quasi–particle picture. This type of lattice vibration is called phonon as a bosonic quasiparticle picture. The vibration of the lattice is scattered due to the interaction between the electron and the phonon and can be analyzed similar to the particles in the classical picture. However, it is hard to imagine that this scattering process is performed in a local area, unlike the actual collision between particles (ex)Umklapp Process). Due to the periodic nature of the lattice in the crystal, this vibration has a normal mode with a certain k value depending on the energy and is called phonon dispersion.

Second quantization can be used to simply represent a quasiparticle picture. Hamiltonian by phonon is given as follows. [25]

$$H_{ph} = \sum_{\vec{q}} \sum_{j}^{3n} \hbar\omega_j(\vec{q})(b_{j,q}^{\dagger} b_{j,q} + \frac{1}{2}). \qquad (38)$$

,where $b_{j,q}^{\dagger}$ and $b_{j,q}$ are creation and annihilation operator for phonon in j branch and momentum q with energy dispersion $\omega_j(\vec{q})$. For small momentum $\vec{q}$, if the dispersion of vibration mode is linear in q, it is called acoustic phonon. If it has non–zero energy at q = 0, it is called optical phonon. Now we can consider a system where

phonon and electron interact. In the Born–Oppenheimer approximation, the atomic mass is much larger than the mass of the electron, thus separating the atomic motion from the electron motion. The system considering interaction between phonon and electron is based on this approximation. Since the equations in which atomic motion and electron motion are combined are complex to deal with, it is possible to use an approximation method by simply adding an interaction term to the Hamiltonian and electron Hamiltonian for the phonon used above. This Hamiltonian is called Fröhlich Hamiltonian and can be described as follows.[45]

$$H_F = \sum_{\vec{k}} \varepsilon(\vec{k}) c_{\vec{k}}^{\dagger} c_{\vec{k}} + \sum_{\vec{q},j} \hbar\omega_j(\vec{q}) \left(b_{j,q}^{\dagger} b_{j,q} + \frac{1}{2} \right) + \sum_{\vec{k},\vec{G}} \sum_{\vec{q},j} [M_j(\vec{q})\, c_{\vec{k}+\vec{q}+\vec{G}}^{\dagger} c_{\vec{k}} b_{\vec{q},j} + M_j(-\vec{q}) c_{\vec{k}-\vec{q}+\vec{G}}^{\dagger} c_{\vec{k}} b_{\vec{q},j}^{\dagger}] \quad (39)$$

As seen in this equation, the first term and the second term are Hamiltonian for free electrons and free phonons, respectively. However, the final term is the interaction term describing the scattering of electrons and phonons, where M is the matrix element of the electron–phonon iteraction. The first of the third term means that the electron having the wave vector k absorbs the phonon and the scttering of the phonon receives the momentum q, and the second means that the electron emits a phonon with q. The Feynman diagram clearly shows. On the left is the process of phonon absorption, and on the right is the emission of the phonon.

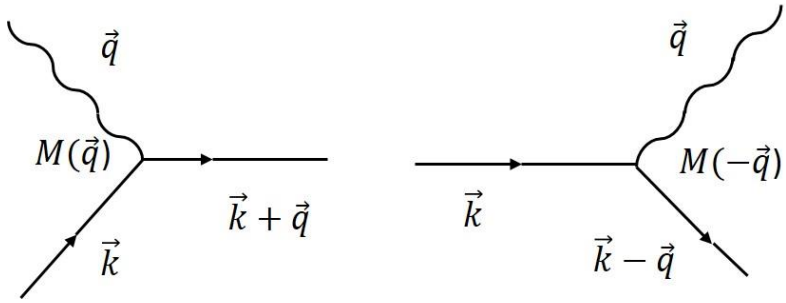

Figure 37. Feynman Diagrams of electron–phonon scattering

The phonons emitted by electrons are again absorbed by other electrons. Through this, the coupling between electrons by electron–phonon interaction can be considered. When the electron moves, it passes through the positively charged ion core in the lattice, and the position of the ion core changes by the electron. This produces a phonon, which can be driven by the local electric field created by the generated phonon. That is, two electrons mediate the phonon and are coupled to each other. The canonical transformation of the Hamiltonian above makes it more clear. When the above Hamiltonian is canonical transformed, the first order of the off–diagonal term is as follows. [25]

$$H_{e-e} = \sum_{\vec{k},\vec{k'}} \sum_{\vec{q}} |M(\vec{q})|^2 \frac{\hbar\omega_{\vec{q}}}{(\varepsilon_{\vec{k}+\vec{q}} - \varepsilon_{\vec{k}})^2 - (\hbar\omega_{\vec{q}})^2} c^{\dagger}_{\vec{k'}+\vec{q}} c_{\vec{k'}} c^{\dagger}_{\vec{k}-\vec{q}} c_{\vec{k}} \tag{40}$$

For a more clear representation here, the dispersion relation by the Umklapp process ($\vec{G} \neq \mathbf{0}$) is neglected and only one branch of the dispersion relation is considered. In this equation, although the phonon is not created or annihilated, it can be seen that the phonon is involved in the coupling of the two electrons by causing an energy exchange. The interesting thing is that if the energy of two electrons is almost the same, the coupling term mediated by the phonon becomes negative (i.e. $\left|\varepsilon_{\vec{k}+\vec{q}} - \varepsilon_{\vec{k}}\right| < \hbar\omega_{\vec{q}}$), so it attracts two electrons in the vicinity of the fermi level, and the coupled pair can lower the energy of the system Therefore, we can consider the existence of a ground state in which a pair exists.

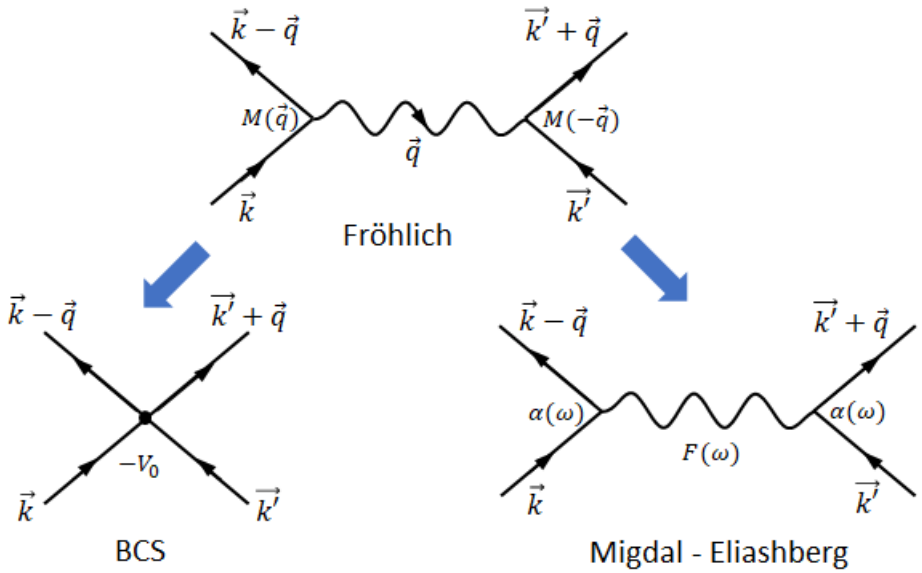

Figure 38. Illustration of electron−electron interaction in three different models

To further simplify the equation, if we define the coupling term as follows,

$$|M(\vec{q})|^2 \frac{\hbar\omega_{\vec{q}}}{\left(\varepsilon_{\vec{k}+\vec{q}}-\varepsilon_{\vec{k}}\right)^2-\left(\hbar\omega_{\vec{q}}\right)^2} = \begin{cases} -V_0, & \left|\varepsilon_{\vec{k}+\vec{q}}-\varepsilon_{\vec{k}}\right| < \hbar\omega_D \\ 0, & otherwise \end{cases} \quad (41)$$

,where ω_D is Debye frequency of the system. Equation (40) becomes pairing term of the BCS Hamiltonian. In order for this assumption to be established, the size of the interaction term must be small, so that it is only valid in the region where $n(E_F)\mathrm{V}_0 \ll 1$. ($n(E_F)$: electron density at Fermi level)

Eliashberg solved this coupling term in Frohlich Hamiltonian using the Eliashberg function $\alpha^2F(\omega)$. This Eliashberg function is expressed as Equation 30, $F(\omega)$ is the density of states of the phonon, and α is the average value of the electron−phonon coupling constant along the energy ω.

$$\alpha^2F(\omega) = \int \frac{d^2k}{v_F} \int \frac{d^2k'}{(2\pi)^3 v'_F} \sum_j M_j(\vec{k} - \vec{k'}) \delta(\omega - \omega_j(\vec{k} - \vec{k'}))(\int \frac{d^2k}{v_F})^{-1}. \quad (42)$$

In the isotropic S wave superconductor, it is an important assumption that the Eliashberg theory deals with approximation by averaging neglecting the contribution of the momentum dependence of the electron phonon coupling. Superconducting properties can be obtained by using this Eliashberg function. At T = 0, the superconducting gap function $\Delta(\omega)$ can be derived by the following two equations using the Eliashberg function.

$$\Delta(\omega) = \frac{1}{Z_s(\omega)} \int_o^{\omega_c} d\nu \, Re(\frac{\Delta(\nu)}{\nu^2 - \Delta^2(\nu)})(K_+(\nu, \omega) - \mu^*)$$
$$(1 - Z_s(\omega))\omega = \int_o^{\infty} d\nu \, Re(\frac{\Delta(\nu)}{\nu^2 - \Delta^2(\nu)}) K_-(\nu, \omega) \quad (43)$$

Where $\Delta(\omega)$ is a gap function defined with energy ω and $Z_s(\omega)$ is a normalization factor and is associated with superconducting self-energy. μ^* is given to consider screening effect as an electron-electron pseudo-potential. ω_c is a cutoff frequeny, usually 10 times the value of the Debye frequency. Here, the Eliashberg function is contained in the following function,

$$K_{\pm}(\nu, \omega) = \int_o^{\infty} d\omega' \, \alpha^2F(\omega')(\frac{1}{\omega + \omega' + \nu + i\delta} \mp \frac{1}{\omega - \omega' - \nu + i\delta}) \quad (44)$$

, where $\delta \longrightarrow 0$. Therefore, two parameters, $\alpha^2F(\omega)$ and Coulomb blockade pseudo-potential μ^*, can be derived for the phonon mediated conventional superconductor, which is well suited for even the strong coupling limit. To obtain the quasi particle density of state through the gap function $\Delta(\omega)$ derived from these two equations, the equation derived from the following BCS theory can be used.

$$\frac{n_S(E)}{n_N(E_F)} = Re\left(\frac{E}{\sqrt{E^2 - \Delta^2(E)}}\right) \quad (45)$$

, where $n_S(E)$ is a density of states in superconducting phase, and $n_N(E)$ is that of normal metal phase. According to the original BCS theory, the gap function delta has a constant value, but the gap function derived from the Eliashberg theory has an energy dependent value. Therefore, the quasi-particle density of state derived from the BCS theory shows monotonic decreasing outside the gap, but quasi-particle DOS according to the Eliashberg theory allows the feature of bosonic mode involved in coupling.

Considering the gaussian phonon distribution with peaks at ω_0 as shown in the following figure, due to the influence, the gap function has the shape shown as the following figure, resulting in phonon mode in the vicinity of $\omega_0 + \Delta$ in quasi-particle density of states. Once this is further differentiated, the dip feature will appear at $\omega_0 + \Delta$. This dip shape is not general and can vary depending on the symmetry of the gap and the shape of the band. Generally, the log singularity is generated, but one side becomes stronger or weaker, and the following form appears.

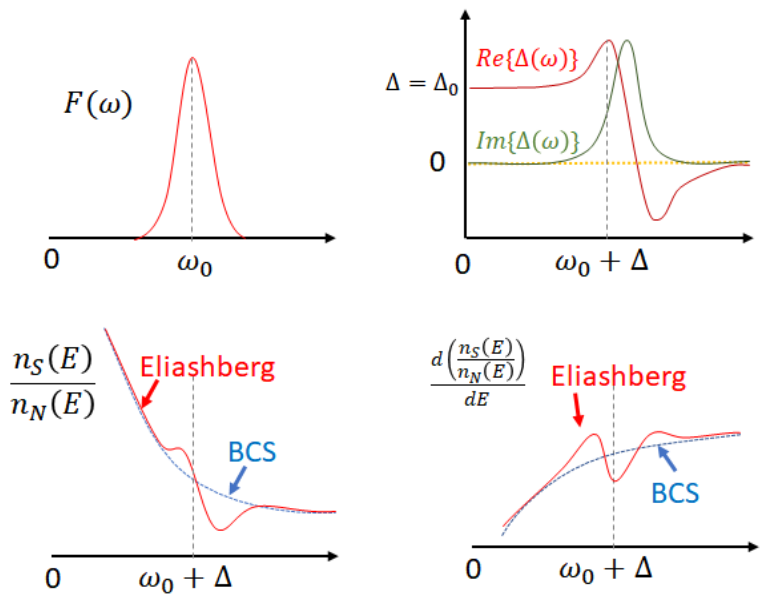

Figure 39 Application of the Eliashberg gap equations to a gaussian single-phonon mode model

This change in density of states is observed symmetrically in the empty-state and filled-state due to the particle-hole symmetry of the superconductor. Similar to the IETS described above, phonon mode can be observed through electron tunneling. However, the IETS is generally a dip-peak form with positive energy and dip with negative energy, which is in contrast to the peak-dip feature of the Eliashberg feature. The size of the Eliashberg feature is larger than the size of the IETS by the general phonon mode, so it is easy to observe using the tunneling measurement.

The Eliashberg equation can also be described in the same way as phonon by ordinary bosonic excitation. Therefore, features of other bosonic modes (eg, plasmon, magnon, polaron ..) other than phonon mode also appear in the same form. Since the Eliashberg feature only reflects the phonon or bosonic mode involved in pairing, observing the Eliashberg feature can reveal the mechanism involved in the pairing mechanism. However, in reality, it is not observable according to the spectrum feature of bosonic mode. Since bosonic modes such as Optical Phonon have a narrow energy spectrum, they can be reflected clearly in DOS, but in case of spin fluctuation, they show a broad energy spectrum. It is also possible to reduce the size of the observation error.

5.2.2. Superconducting mechanism in FeSe/STO

The octahedral oxygens can easily rotate around the center, giving rise to possible distortions to the perfect crystal. At Tc ≈ 105K, STO undergoes a cubic to tetragonal anti-ferro distortive transition. This phase transition is from the rotation of the oxygen octahedral around one of the cubic main axes, and two adjacent cell rotate in the opposite direction. Also, there is ferroelectric phase transition observed by Raman spectroscopy around 50K quite close to superconducting phase transition of FeSe/STO. These exotic characteristics of STO are considered as ingredients for enhancing Tc of FeSe/STO system

5.3. Sample Preparation and Characterization

Like complex oxides of the general formula ABO_3, $SrTiO_3$ (STO) has a simple cubic perovskite structure at room temperature, consisting of simple cubic lattice of strontium atom at the corner, oxygen atoms at the face center, and titanium atoms at the body center as shown in Figure 40.

Even though there are many different phases in iron selenides, it is well known that FeSe in tetragonal layered structure (α−FeSe phase) is preferred to grow on the STO(100) surface. In each layer of α−FeSe, Fe layer is sandwiched between two Se layers of, and the top Se layer atoms are arranged in 45 degrees with respect to the bottom Se layer atoms as shown in Figure 40. Since FeSe layer and STO have small lattice misfit ~3.6% (FeSe : 3.76Å, STO : 3.90 Å), FeSe can readily be grown on the STO(100) surface by molecular beam epitaxy.

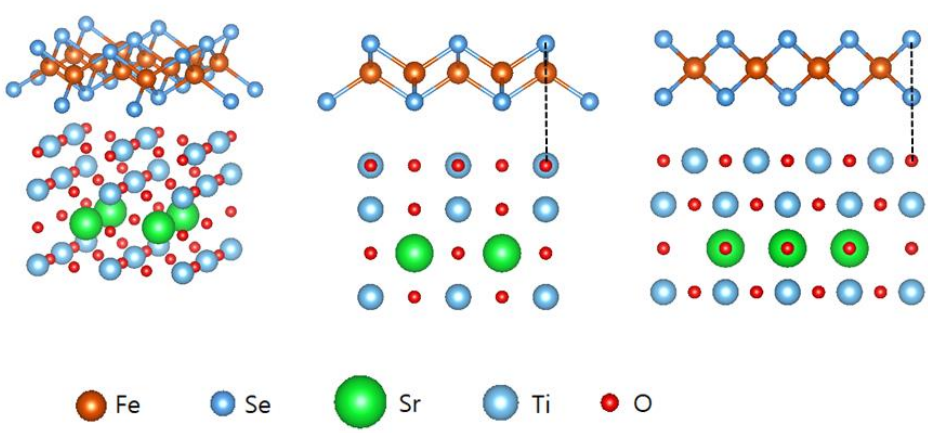

Figure 40. Atomic structure of FeSe/SrTiO3(100)

There is a double TiO2 layer between FeSe and SrTiO3(100). Normally, oxygen vacancies occur in upper TiO2 layer[46].Low selenium atom of FeSe layer bonds to the oxygen (vacancy) site on the TiO_2 layer.

In the recent experiment with scanning transmission electron microscope(STEM), there is a double TiO_2 between FeSe and STO interface as shown in Figure 40. It is considered that oxygen vacancies on topmost layer of the double TiO_2 layer behave as charge dopants when FeSe/STO is in superconducting phase. On the oxygen vacancy site, Se atom in the bottom layer of FeSe bonds. This double TiO_2 layer, also referred as titania, is considered as the ingredient to enhance Tc of FeSe/STO system so far, and there are many experimental supports about this substrate effect

5.3.1. STO Cleaning

The surface of $SrTiO_3$ (100) shows SrO and TiO_2 at random. Therefore, it is difficult to grow FeSe because it has no termination in case of as received sample. What is important in FeSe / STO is the TiO2 layer of the top most double layer, which is related to the coupling with the substrate. To make this, we refer to the commonly known cleaning method [11], [47].

First, we sonicate using Acetone and IPA to remove residues on the surface of the sample. After that, to remove SrO, it was immersed in buffered HF for 5 minutes and then rinsing with DI water and removing SrO.

Since SrO is a polar compound, it dissolves well in water. The cleaned sample was introduced into the UHV chamber and was subjected to overnight outgassing at 900 ° C. The sample was annealed at 1100 ° C for 15 minutes and then repeatedly washed at 900 ° C. Since annealing is performed at high temperature, resistance heating method is used to lower the outgassing rate. In this method, only the STO part is locally heated and a clean surface can be obtained. After that, STM was confirmed to be clean and density of state of bare STO was obtained through tunneling spectroscopy(Figure 41).

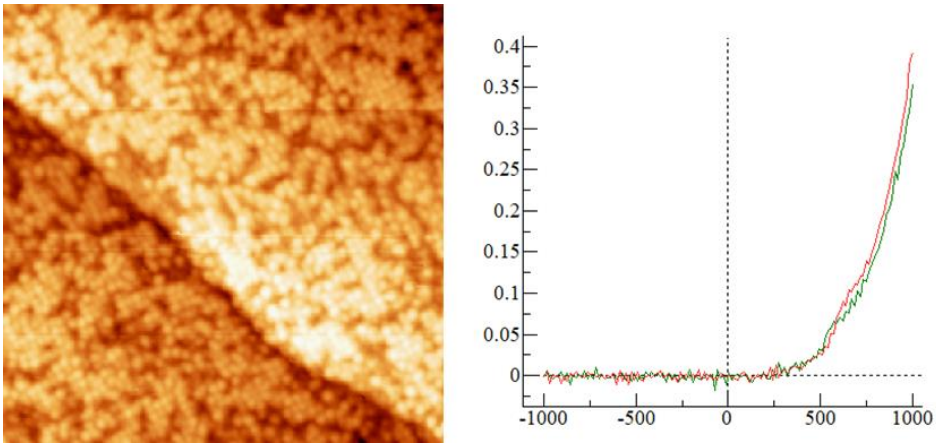

Figure 41. Clean $SrTiO_3$(100) surface and its tunneling spectra

5.3.2. FeSe Growth and doping

FeSe was grown on a clean $SrTiO_3$(100) surface using the molecular beam epitaxy method. Fe was deposited by an e−beam heating source and Se was deposited by a Knudsen cell. Deposition rate was measured using a homebuilt thickness monitoring sensor. 1UC−FeSe was grown using the method grown in the Xue group [47]. The deposition rate ratio of Fe and Se was 1: 10 ~ 20 and the temperature of the substrate was maintained at 450 ~ 500 ℃ during source deposition. After the growth, the post annealing was carried out at a temperature of between 530 and 580 ° C for 1.5−2 hours which is measured by a pyrometer with 0.6 emissivity.

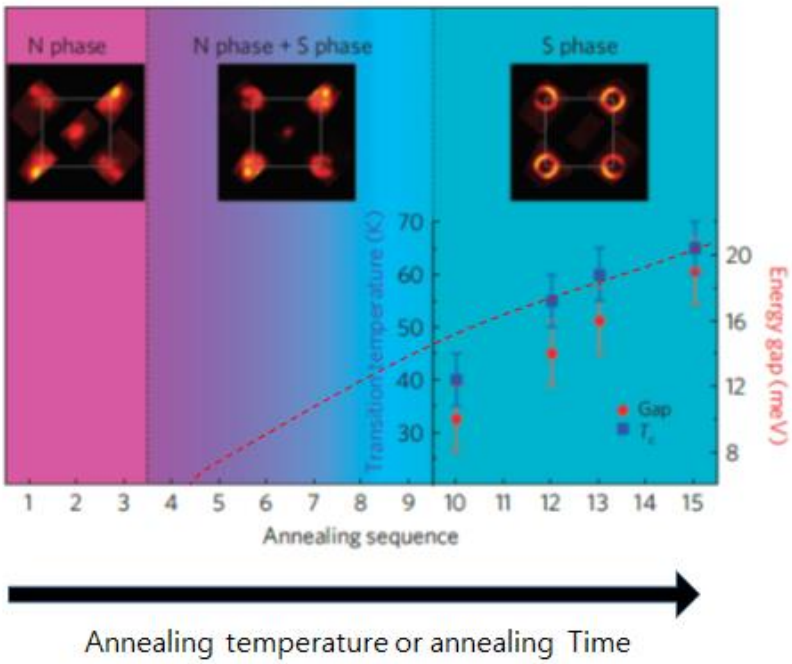

Figure 42. Doping level vs annealing sequence

(Phase diagram from [48])

This post annealing temperature and time are important when growing FeSe because the doping level of the superconductor is determined. Figure 42 shows the results of ARPES by controlling the doping level by creating many oxygen vacancies through different annealing sequences. When the doping level is low, FeSe shows the insulating nature. However, when the doping level is increased through post-annealing, the superconducting phase comes out. FeSe / STO superconductors are known to increase Tc as post annealing is maintained at high temperature for a long time, but FeSe does not grow and disappear at too high post annealing temperature (>600 ° C.)

However, the ability to easily adjust the doping level through annealing shows the possibility of studying the superconductivity of various phases while controlling the doping level. Using this point, we discussed the phenomena observed in the under-doped FeSe / STO

phase grown at various post-annealing temperatures in the next chapter.

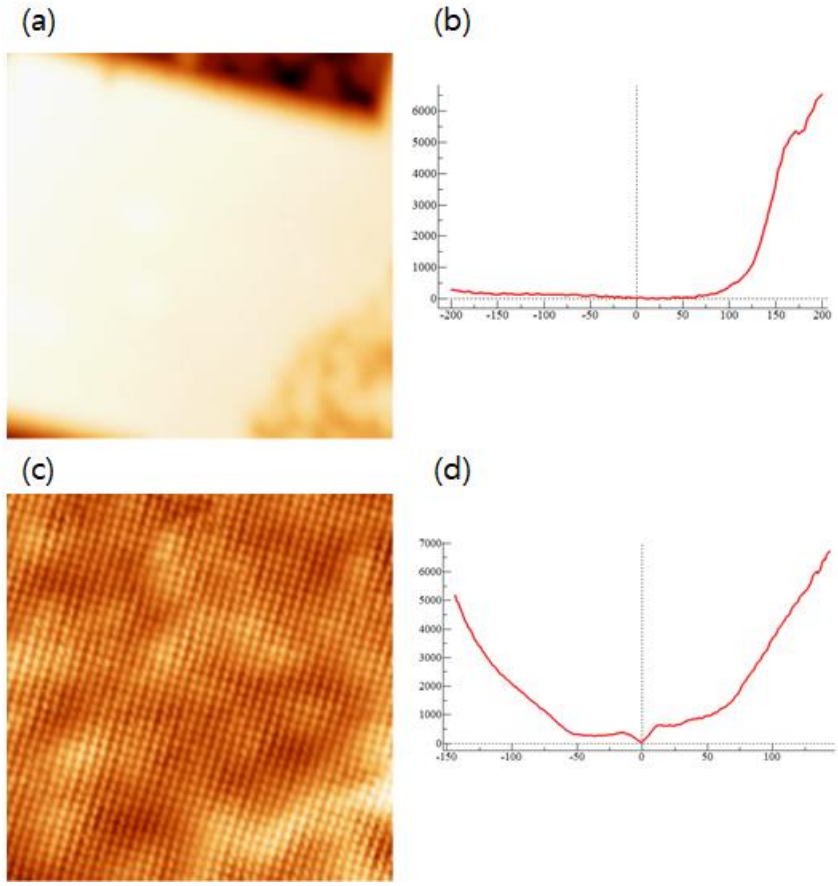

Figure 43. Topographic image and tunneling spectra of $FeSe/SrTiO_3(100)$

5.4. Oxygen vacancy dopant ordered state on 1UC-FeSe/STO

5.4.1. Oxygen vacancy ordering in High-Tc

It is well known that the microstructures of the transition-metal oxides, including the high-transition-temperature (high-Tc) copper oxide superconductors are complex. This is particularly so when there are oxygen interstitials or vacancies[49], which influence the bulk properties. For example, the oxygen interstitials or vacancies in

the spacer layers separating the superconducting CuO_2 planes undergo ordering phenomena in $Sr_2O_{1+y}CuO_2$[50] $YBa_2Cu_3O_{6+y}$[51] and La_2CuO_{4+y}[52]–[54] that induce enhancements in the transition temperatures with no changes in hole or electron concentrations.

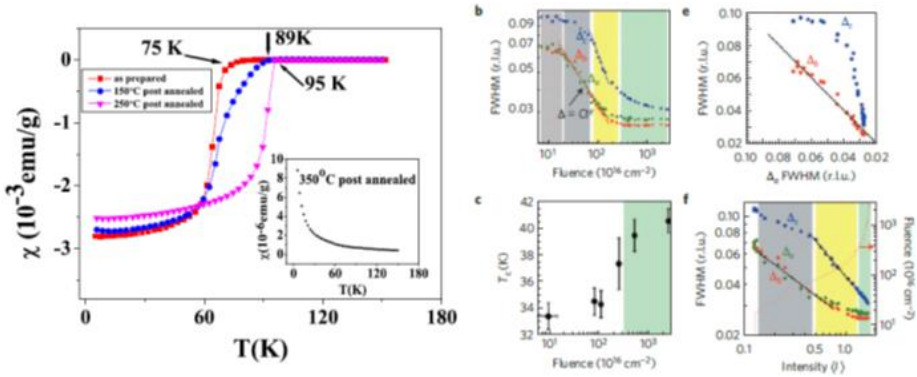

Figure 44. Oxygen interstitials ordering in cuprate superconductor Dopant ordering dependent Tc (taken from [50]) and superconducting gap change (taken from [55])

In the case of the cuprate sample, the ordering of the dopant contributes to the increase of the phase transition temperature of HTSC, and this ordering may be associated with the paring mechanism.

5.4.2. Dopant state in FeSe/STO Insulating Phase

In 1UC-FeSe / STO, the size of the gap changes according to the doping, and the doping of the superconducting layer is performed by using the excess electron given by the oxygen vacancy while the TiO2 layer directly underneath acts as a charge reservoir. As can be seen in Figure 40, the oxygen vacancy of the double TiO_2 layer under FeSe corresponds exactly to the position of the Se atom of FeSe. In other words, selenium is projected onto the TiO_2 surface, oxygen is present in the site, and this oxygen is missing and becomes a dopant. In the superconducting state, due to the Thomas Fermi screening of

the superconducting layer, the electric field caused by the charge in the lower layer is screened and the local charge distribution cannot be made on the FeSe surface. However, underdoped FeSe / STO has an insulating nature likewise in the case of the parent compound.

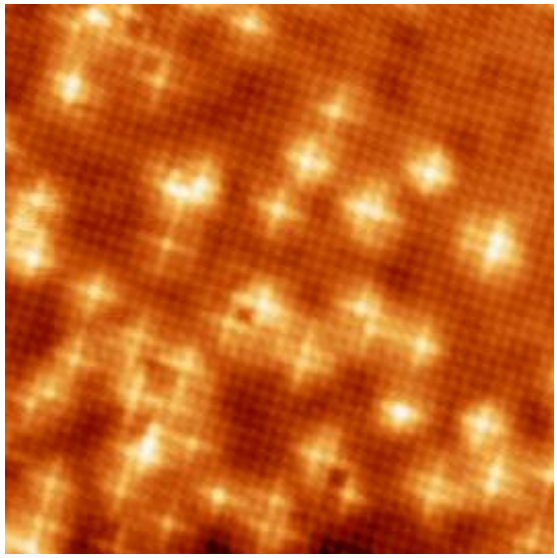

Figure 45. Dopant states reflected on FeSe/$SrTiO_3$(100)

Oxygen vacancies at TiO_2 layer under the FeSe layer behave as dopants, so they form local charge distribution on upper FeSe layer.

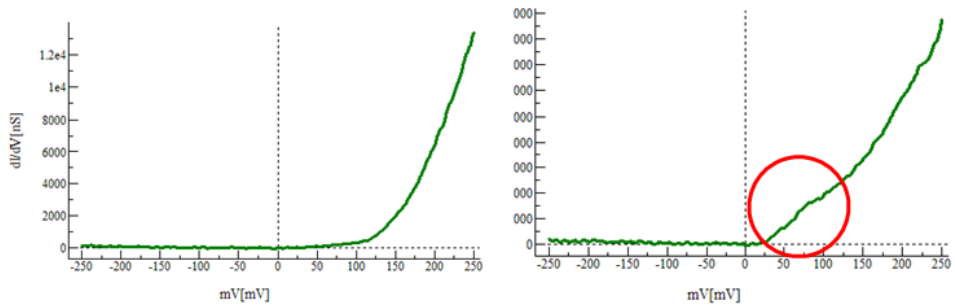

Figure 46. Tunneling spectra on the FeSe(left) and on the dopant(right)

On the dopant site, there is a state around 50meV~150meV comparing with bare FeSe layer.

Therefore, we can see the state of the dopant even on the FeSe layer and can predict the characteristics of the dopant state based on it. Figure 45 shows a cross-shaped charge state over FeSe. If you measure the LDOS above, the state is above the Fermi level, unlike the bulk STS shown in Figure 46. Through this result, we can see that the results observed through STM are due to the electron dopant state. The cross shape of this dopant state is not known exactly yet. Oxygen vacancy has a charge of -2e and is coupled with two adjacent Ti atoms in a p-orbital, so if it is thought to be an orbital shape of an oxygen defect, it should have a two-fold symmetry. Therefore, a possible scenario is that the charge from below directly charges the Fe layer only, so that the charging center appears as a cross shape because it is adjacent to the four Fe atoms.

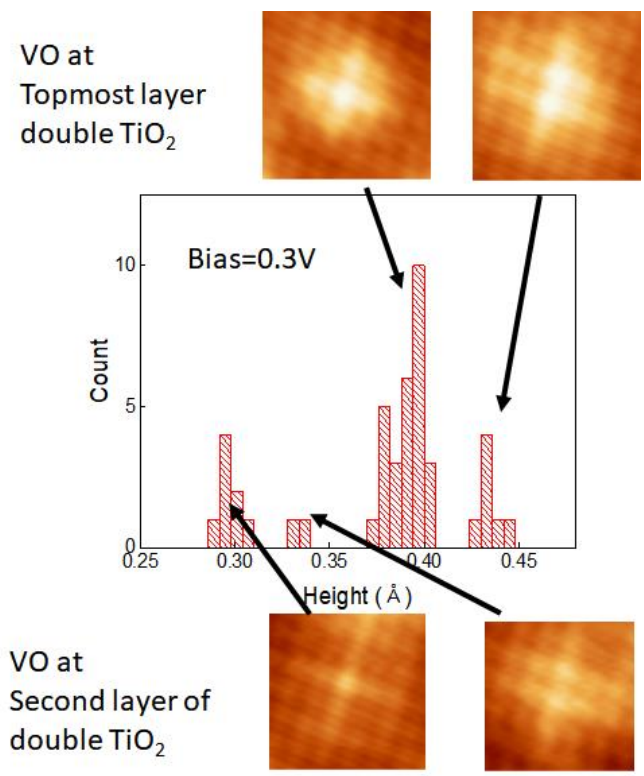

Figure 47. Distribution of dopant state height

The results for dopant state height are shown in Figure 47. The height of the dopant state is quantized to two except that the two

overlaps and appear higher. This suggests that the oxygen vacancy exists only on the double TiO_2, not only in the topmost TiO_2 layer but also in the second layer. It can be observed that the number of topmost oxygen vacancies is higher because of the energy advantage of the oxygen vacancies in the topmost layer.

5.4.3. Dopant ordering in FeSe/STO

As mentioned earlier, the interesting thing about this dopant state is that as the doping level increases, it changes from random to ordered. Figure 48 shows that the number of dopant states shown in Figure 40 increases. Interestingly, as the number of dopants increases, the long range ordering of the dopants is observed. Figure 48 shows that the dopant site is ordered and shows a 1D-CDW like shape, showing a $\sqrt{13} \times \sqrt{13}\, R\, 21.1^{\circ}$ structure. However, the overall CDW like form is not visible, indicating that the dopant is ordered within short range.

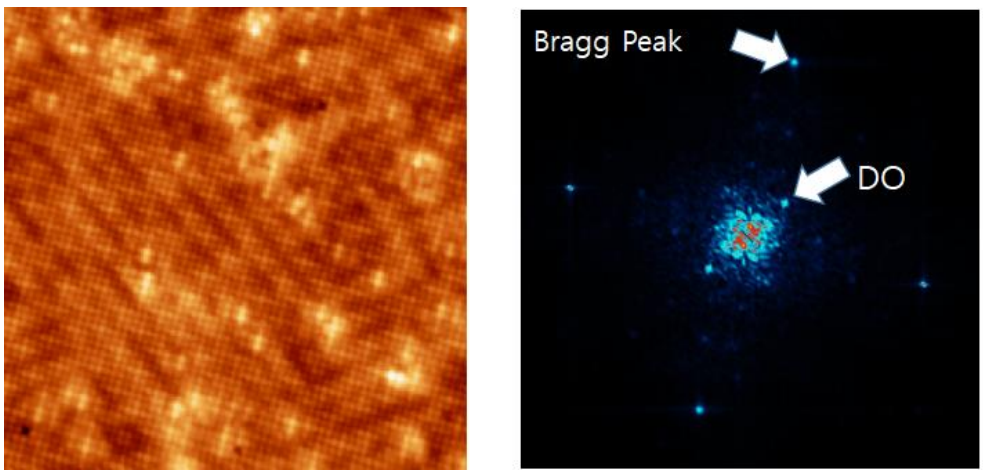

Figure 48. Topographic image of $\sqrt{13} \times \sqrt{13}\, R\, 21.1^{\circ}$ vacancy ordered phase(left) and its Fourier transformed map.

If we look at the tunneling spectra in the same region, we can see superconducting gap like results. This gap is larger than superconducting phase gap which is about 10~15meV even this is an under-doped sample. Nevertheless, the fact that the underlying state is visible means that this is a phase that does not screen the bottom-level state well, and thus the observed gap may be a pseudo gap or superconducting gap.

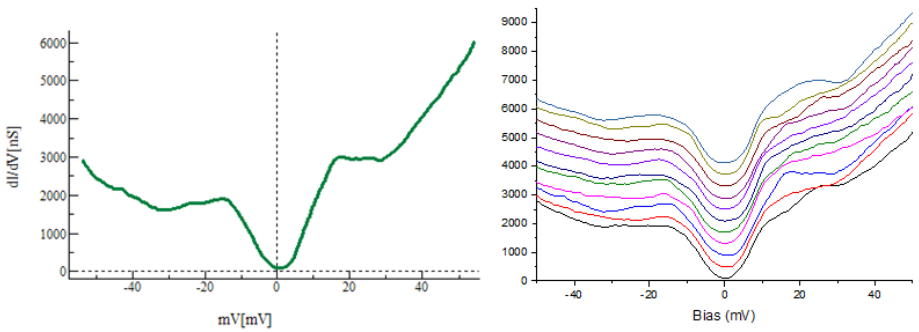

Figure 49. Tunneling Spectra on vacancy ordered FeSe/STO(left) and positional dependent spectroscopy(right)

As you look at the results of the more doped part, you can see that the ordering takes place over a wider range. The ordering in this case is $\sqrt{6} \times \sqrt{6}$ ordered phases and shows a gap size smaller than the observed gap in Figure 49.

Interestingly, the order of the long range ordered oxygen is changed according to the phase of the domain of FeSe. Figure 45 shows that the observed dopant state in the other domain is about 23 degrees from the original domain, which has a mirror symmetric order based on the Bragg peak.

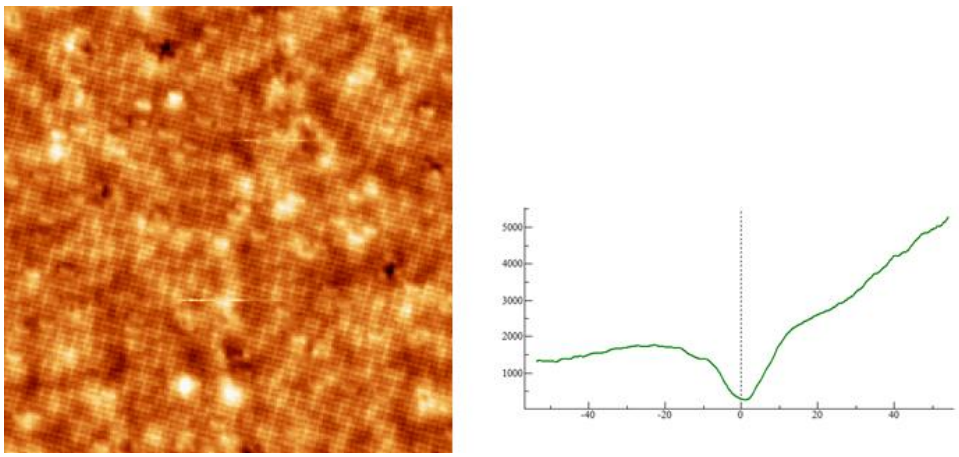

Figure 50. Topographic image of $\sqrt{6} \times \sqrt{6}$ vacancy ordered phase(left) and its tunneling spectrum,

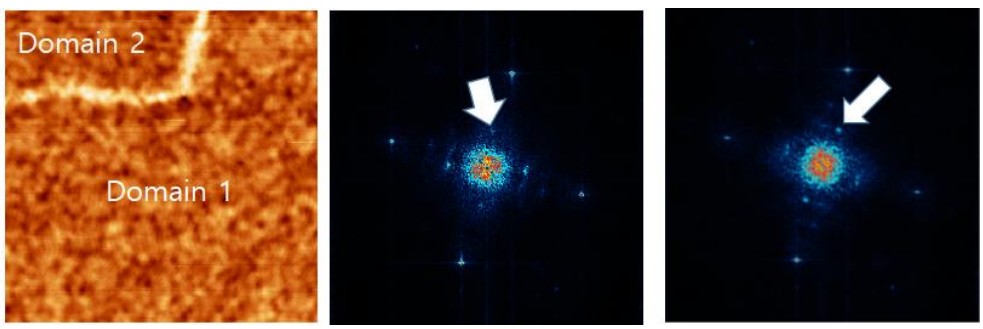

Figure 51. Domain dependence of the dopant ordering

5.5. Tunneling spectroscopy of FeSe/STO

5.5.1. Eliashberg Feature

As mentioned earlier, the superconductor exhibits feature of bosonic mode outside the gap. This is a way to see bosonic features in the superconductor, unlike the IETS signal. Figure 52 shows the Migdal-Eliashberg feature in the FeSe / STO system. According to Migdal-Eliashberg theory, the electron-boson interaction changes the quasi-particle DOS, unlike the IETS, the interaction with the geometry of the tunneling junction is not large. Therefore, it can be seen that there is almost no big difference when the reference

current is changed to change the distance of the tunneling junction. When we observe the Eliashberg feature in the tunneling spectra, we can see that bosonic mode exists at about 9meV and 14meV. However, this system can have two gap states because the Fermi surface at M point is not uniform. These two gaps are present at 10 meV and 15 meV, from which the Eliashberg feature can be considered a replica feature due to two gaps.

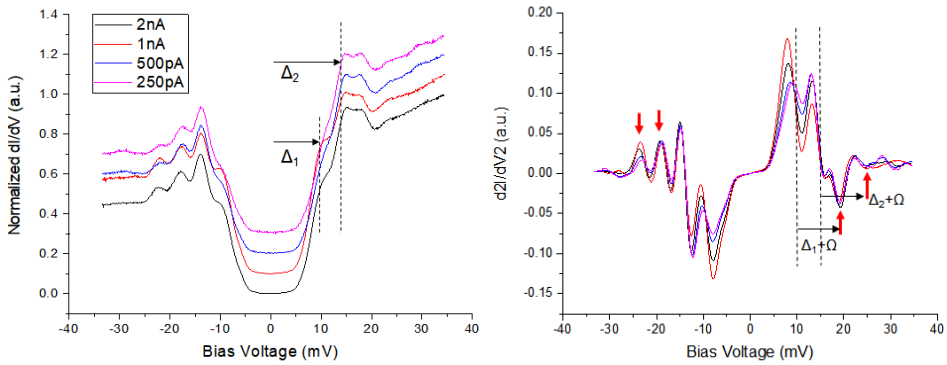

Figure 52. Eliashberg features on tunneling spectra of FeSe/STO

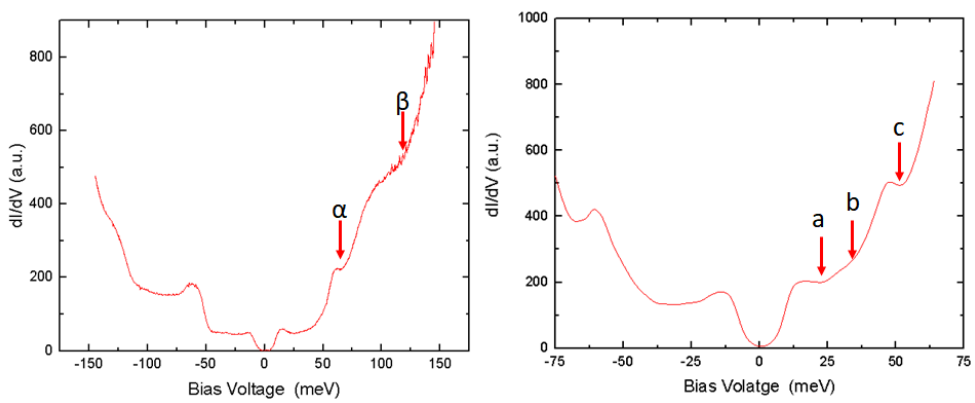

Figure 53. Various bosonic mode reflected on DOS of FeSe/STO

When the tunneling spectra of a higher bias voltage are observed, bosonic mode like features appear at about 60 meV and 100 meV. When a candidate for bosonic mode that can be observed at high

energy was observed, the FK mode of STO was observed at 60 meV and 100 meV from HREELS [56], and the replica band was also confirmed in the result of ARPES [57]. Therefore, it can be considered that this is due to the FK mode of the STO substrate.

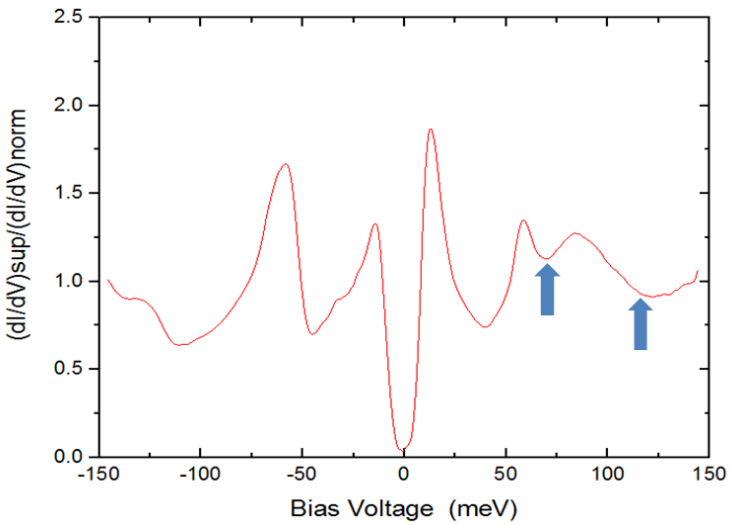

Figure 54. FK phonon mode feature on normalized conductance of FeSe/STO

If you look at the normalized density of state, it looks relatively smaller than Figure 53, so it needs to be verified through the Eliashberg calculation whether this mode is related to pairing.

5.5.2. Magnetic Field dependence

To better understand the pairing mechanism of FeSe / STO, we investigated the relationship with the magnetic field. In general, cuprate and pnictide HTSC have the most noticeable pairing mechanism with spin fluctuation [44], [58]. If the pairing mechanism is related to the spin, it is likely to be related to the magnetic field. Therefore, we investigated the relationship between the magnetic field and the Migdal–Eliashberg feature. Since FeSe/STO is 2D superconducting state, the sample thickness is thinner than

penetration depth, unlike general superconductor. Therefore, if a strong magnetic field is applied, a portion of the magnetic field may be able to influence the non-vortex region.

First, we examined whether the Eliashberg feature disappears in the vortex area. Figure 55 shows the vortex state at the domain boundary when Zero bias conductance mapping at B = 5.5T. In general, a vortex can be found using a zero bias conductance map on the domain boundary, since it is well pinned to the domain boundary[59].

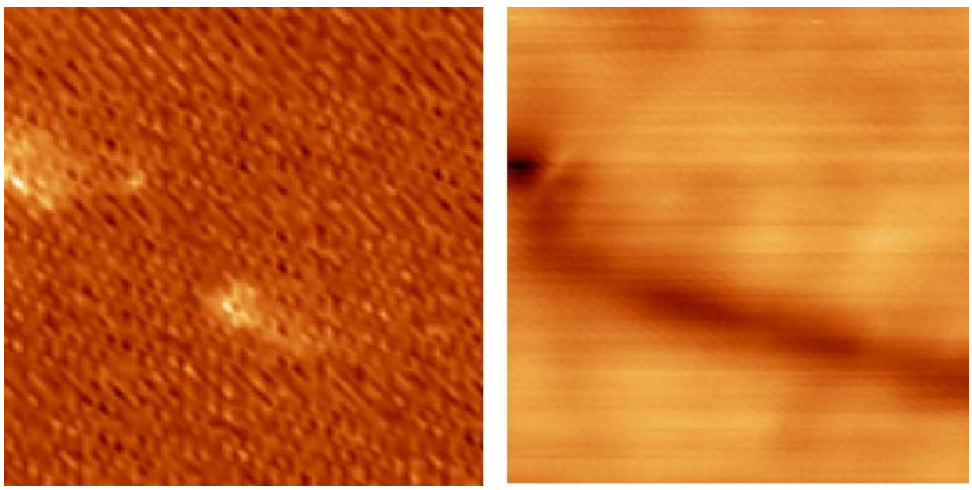

Figure 55. Zero-bias conductance map and topographic image near the vortex

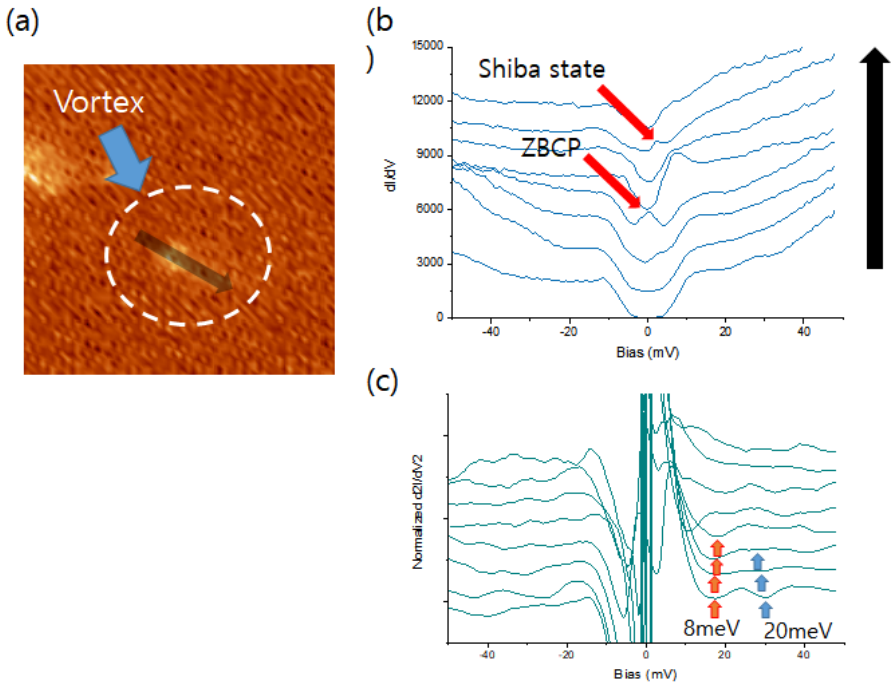

Figure 56. Tunneling spectroscopy and Eliashberg feature along the vortex

Positional LDOS was measured near the vortex with the magnetic field at B = 5.5T (Figure 56). When we looked at this dI / dV spectra, we could see the zero bias conductance peak at the vortex center and we could see the Shiba state near the center. Therefore, we can consider the possibility that this vortex pinning was induced by magnetic impurity.

We observed the Eliashberg feature at 8meV and 20meV in the positional dependent LDOS spectra obtained and observed that the intensity became smaller because the superconducting phase was changed to the normal phase while moving to the center of the vortex. Next, the Eliashberg feature was measured at the off-vortex site to study the spin dependent pairing(Figure 57). As mentioned above, the magnetic field can penetrate through a thin superconductor, which can affect the bosonic mode of FeSe. When we change the magnetic field from 0T to 4T, we can see the Eliashberg feature at about 15meV in the tunneling spectra. However, even if the magnetic field

is changed, there is no significant difference, and it can be interpreted that the bosonic mode is hardly affected by the magnetic field.

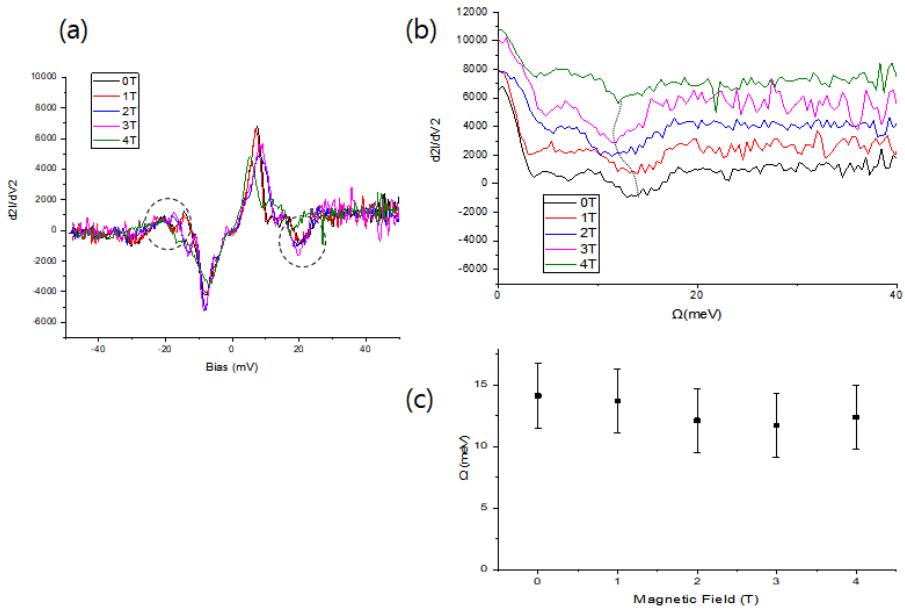

Figure 57. Magnetic field dependency of Eliashberg feature at the same site

5.6. Discussion

1UC-FeSe/STO is a 2D superconductor and a high-Tc superconductor. This sample is easily grown through molecular beam epitaxy (MBE) and is a good sample to observe with STM. Despite the high Tc and simple structure, there is no known mechanism for increasing the Tc. Recently, many models have been proposed that intrinsic paring mechanism exists, and FK phonon mode of substrate enhances Tc[60], [61]. There are theories that the phonon mode of the STO boosts the superconductivity of FeSe through the ARPES results of FeSe observations. An important point here is that one of the prerequisites for boosting Tc is that the momentum change of the

phonon to the electron should be very small when the electron and the phonon are scattering. This is called forward scattering phonon mode, and it is claimed that anisotropic dielectric constant is required for this to happen. Viewing the dopant state is one way to extract information about the dielectric response from the STM. Since 1UC-FeSe/STO is a system that can easily change doping level by post annealing condition, we changed the doping level while raising post annealing temperature. We have found a dopant state at low post annealing temperature and can be interpreted as having a higher in-plane dielectric constant than that of a normal dopant. An exact discussion of this needs to be quantified through simulation.

The Eliashberg feature is a good way to view information about the phonon mode involved in pairing through the tunneling spectra. In the superconducting state, we were able to observe the Eliashberg feature at 9 to 12 meV. I tried several things to know the origin of this. The bosonic mode, which can be considered in low bias energy, is typically spin fluctuation and acoustic phonon mode. However, when the magnetic field is present, the low-bias Eliashberg feature does not change, suggesting that this bosonic mode has high potential and does not have magnetic properties. The Eliashberg feature at 9-12 meV is likely to be a phonon and the same at around 40 meV, considering that the energy level is good when compared with HREELS data[56]. But this alone cannot pinon the pairing mechanism of this superconductor to the phonon. The spin fluctuation mechanism has a broad density of states, which makes it difficult to observe through tunneling. Therefore, it is difficult to predict the pairing mechanism only with Eliashberg, and the theoretical interpretation needs to be further discussed.

Bibliography

[1] W. Su, J. R. Schrieffer, and A. J. Heeger, "Solitons in polyacetylene," *Phys. Rev. Lett.*, vol. 42, no. 25, p. 1698, 1979.

[2] I. K. Drozdov *et al.*, "One-dimensional topological edge states of bismuth bilayers," *Nat. Phys.*, vol. 10, no. 9, p. 664, Sep. 2014.

[3] J. Seo, P. Roushan, H. Beidenkopf, Y. S. Hor, R. J. Cava, and A. Yazdani, "Transmission of topological surface states through surface barriers," *Nature*, vol. 466, no. 7304, p. 343, Jul. 2010.

[4] F. Ma *et al.*, "Predicting a new phase (T'') of two-dimensional transition metal di-chalcogenides and strain-controlled topological phase transition," *Nanoscale*, vol. 8, no. 9, pp. 4969–4975, Feb. 2016.

[5] M. König *et al.*, "Quantum Spin Hall Insulator State in HgTe Quantum Wells," *Science*, vol. 318, no. 5851, pp. 766–770, Nov. 2007.

[6] P. Roushan *et al.*, "Topological surface states protected from backscattering by chiral spin texture," *Nature*, vol. 460, no. 7259, p. 1106, Aug. 2009.

[7] H. Zhang, C.-X. Liu, X.-L. Qi, X. Dai, Z. Fang, and S.-C. Zhang, "Topological insulators in Bi_2Se_3, Bi_2Te_3 and Sb_2Te_3 with a single Dirac cone on the surface," *Nat. Phys.*, vol. 5, no. 6, p. 438, Jun. 2009.

[8] M. Wang *et al.*, "A combined method for synthesis of superconducting Cu doped Bi_2Se_3," *Sci. Rep.*, vol. 6, p. 22713, Mar. 2016.

[9] S. Nadj-Perge *et al.*, "Observation of Majorana fermions in ferromagnetic atomic chains on a superconductor," *Science*, vol. 346, no. 6209, pp. 602–607, Oct. 2014.

[10] M. T. Deng, C. L. Yu, G. Y. Huang, M. Larsson, P. Caroff, and H. Q. Xu, "Anomalous Zero-Bias Conductance Peak in a Nb–InSb Nanowire–Nb Hybrid Device," *Nano Lett.*, vol. 12, no. 12, pp. 6414–6419, Dec. 2012.

[11] W. Qing-Yan *et al.*, "Interface-Induced High-Temperature Superconductivity in Single Unit-Cell FeSe Films on SrTiO 3," *Chin. Phys. Lett.*, vol. 29, no. 3, p. 037402, 2012.

[12] J. J. Lee *et al.*, "Interfacial mode coupling as the origin of the enhancement of Tc in FeSe films on SrTiO3," *Nature*, vol. 515, no. 7526, pp. 245–248, Nov. 2014.

[13] C. Zhang *et al.*, "Ubiquitous strong electron–phonon coupling at the interface of FeSe/$SrTiO_3$," *Nat. Commun.*, vol. 8, p. 14468, Feb. 2017.

[14] C.-L. Song *et al.*, "Observation of Double-Dome Superconductivity in Potassium-Doped FeSe Thin Films," *Phys. Rev. Lett.*, vol. 116, no. 15, Apr. 2016.

[15] P. Zhang *et al.*, "Observation of high-Tc superconductivity in rectangular FeSe/SrTiO3(110) monolayers," *Phys. Rev. B*, vol. 94, no. 10, p. 104510, Sep. 2016.

[16] Q. Fan *et al.*, "Plain s-wave superconductivity in single-layer FeSe on SrTiO3 probed by scanning tunnelling microscopy," *Nat. Phys.*, vol. 11, no. 11, pp. 946–952, Aug. 2015.

[17] Z. Li *et al.*, "Visualizing superconductivity in FeSe nanoflakes on SrTiO3 by scanning tunneling microscopy," *Phys. Rev. B*, vol. 91, no. 6, p. 060509, Feb. 2015.

[18] W. Zhang *et al.*, "Interface charge doping effects on superconductivity of single-unit-cell FeSe films on SrTiO3 substrates," *Phys. Rev. B*, vol. 89, no. 6, p. 060506, Feb. 2014.

[19] A. B. Migdal, "Interaction between electrons and lattice vibrations in a normal metal," *Sov Phys JETP*, vol. 7, no. 6, pp. 996–1001, 1958.

[20] I. Giaever, "Electron tunneling between two superconductors," *Phys. Rev. Lett.*, vol. 5, no. 10, p. 464, 1960.

[21] J. Bardeen, "Tunnelling from a many-particle point of view," *Phys. Rev. Lett.*, vol. 6, no. 2, p. 57, 1961.

[22] J. Tersoff and D. R. Hamann, "Theory and application for the scanning tunneling microscope," *Phys. Rev. Lett.*, vol. 50, no. 25, p. 1998, 1983.

[23] J. Tersoff and D. R. Hamann, "Theory of the scanning tunneling microscope," *Phys. Rev. B*, vol. 31, no. 2, p. 805, 1985.

[24] C. J. Chen, "Tunneling matrix elements in three-dimensional space: The derivative rule and the sum rule," *Phys. Rev. B*, vol. 42, no. 14, p. 8841, 1990.

[25] M. P. Schackert, *Scanning Tunneling Spectroscopy on Electron-Boson Interactions in Superconductors*, vol. 13. KIT Scientific Publishing, 2015.

[26] S. H. Pan, E. W. Hudson, and J. C. Davis, "3He refrigerator based very low temperature scanning tunneling microscope," *Rev. Sci. Instrum.*, vol. 70, no. 2, pp. 1459–1463, Feb. 1999.

[27] F. M. Smits, "Measurement of Sheet Resistivities with the Four-Point Probe," *Bell Syst. Tech. J.*, vol. 37, no. 3, pp. 711–718, May 1958.

[28] M.-H. Chiu *et al.*, "Determination of band alignment in the single-layer MoS_2/WSe_2 heterojunction," *Nat. Commun.*, vol. 6, p. 7666, Jul. 2015.

[29] L. Tapasztó, T. Dumitrică, S. J. Kim, P. Nemes-Incze, C. Hwang, and L. P. Biró, "Breakdown of continuum mechanics for nanometre-wavelength rippling of graphene," *Nat. Phys.*, vol. 8, no. 10, p. 739, Oct. 2012.

[30] J.-F. Ge *et al.*, "Superconductivity above 100 K in single-layer FeSe films on doped $SrTiO_3$," *Nat. Mater.*, vol. 14, no. 3, p. 285, Mar. 2015.

[31] I. Razado-Colambo, J. He, H. M. Zhang, G. V. Hansson, and R. I. G. Uhrberg, "Electronic structure of Ge(111)c(2×8): STM, angle-resolved photoemission, and theory," *Phys. Rev. B*, vol. 79, no. 20, p. 205410, May 2009.

[32] A. C. Papageorgopoulos and M. Kamaratos, "A Study of the restoration of Se/Si(111)-7×7 reconstructed surfaces: preservation of the

bulk-terminated state," *Surf. Sci.*, vol. 504, no. Supplement C, pp. L191–L195, Apr. 2002.

[33] R. D. Bringans, R. I. G. Uhrberg, R. Z. Bachrach, and J. E. Northrup, "Arsenic-terminated Ge(111): An ideal 1×1 surface," *Phys. Rev. Lett.*, vol. 55, no. 5, pp. 533–536, Jul. 1985.

[34] C. Stuhlmann, G. Bogdányi, and H. Ibach, "Surface phonons of the hydrogen-terminated Si(111)(1×1) surface," *Phys. Rev. B*, vol. 45, no. 12, pp. 6786–6792, Mar. 1992.

[35] F. Solal, G. Jezequel, A. Barski, P. Steiner, R. Pinchaux, and Y. Petroff, "Ge(111)2×1: π-Bonded Chain Model or Not?," *Phys. Rev. Lett.*, vol. 52, no. 5, pp. 360–363, Jan. 1984.

[36] J. A. Stroscio, R. M. Feenstra, and A. P. Fein, "Electronic Structure of the Si(111)2×1 Surface by Scanning-Tunneling Microscopy," *Phys. Rev. Lett.*, vol. 57, no. 20, pp. 2579–2582, Nov. 1986.

[37] M. A. Olmstead and N. M. Amer, "Polarization dependence of Ge(111)2×1 surface-state absorption using photothermal displacement spectroscopy: A test of surface reconstruction models," *Phys. Rev. B*, vol. 29, no. 12, pp. 7048–7050, Jun. 1984.

[38] D. A. Muzychenko, K. Schouteden, M. Houssa, S. V. Savinov, and C. Van Haesendonck, "Noninvasive Embedding of Single Co Atoms in Ge(111)2×1 Surfaces," *Phys. Rev. B*, vol. 85, no. 12, Mar. 2012.

[39] G. Kresse and J. Furthmüller, "Efficiency of ab-initio total energy calculations for metals and semiconductors using a plane-wave basis set," *Comput. Mater. Sci.*, vol. 6, no. 1, pp. 15–50, Jul. 1996.

[40] J. G. Bednorz and K. A. Müller, "Possible highTc superconductivity in the Ba-La-Cu-O system," *Z. Für Phys. B Condens. Matter*, vol. 64, no. 2, pp. 189–193, Jun. 1986.

[41] "Milestone Superconductivity Above 200 Celsius." [Online]. Available: http://www.superconductors.org/202C.htm. [Accessed: 12-Jun-2017].

[42] F. Steglich *et al.*, "Superconductivity in the Presence of Strong Pauli Paramagnetism: CeCu2Si2," *Phys. Rev. Lett.*, vol. 43, no. 25, pp. 1892–1896, Dec. 1979.

[43] Y. Kamihara, T. Watanabe, M. Hirano, and H. Hosono, "Iron–Based Layered Superconductor La[O1–xFx]FeAs (x = 0.05–0.12) with Tc = 26 K," *J. Am. Chem. Soc.*, vol. 130, no. 11, pp. 3296–3297, Mar. 2008.

[44] L. Shan *et al.*, "Evidence of a Spin Resonance Mode in the Iron–Based Superconductor Ba0.6K0.4Fe2As2 from Scanning Tunneling Spectroscopy," *Phys. Rev. Lett.*, vol. 108, no. 22, p. 227002, May 2012.

[45] D. J. Scalapino, J. R. Schrieffer, and J. W. Wilkins, "Strong–Coupling Superconductivity. I," *Phys. Rev.*, vol. 148, no. 1, pp. 263–279, Aug. 1966.

[46] F. Li *et al.*, "Atomically resolved FeSe/SrTiO $_3$ (001) interface structure by scanning transmission electron microscopy," *2D Mater.*, vol. 3, no. 2, p. 024002, Mar. 2016.

[47] Z. Li *et al.*, "Molecular beam epitaxy growth and post–growth annealing of FeSe films on SrTiO 3 : a scanning tunneling microscopy study," *J. Phys. Condens. Matter*, vol. 26, no. 26, p. 265002, 2014.

[48] S. He *et al.*, "Phase diagram and electronic indication of high–temperature superconductivity at 65 K in single–layer FeSe films," *Nat. Mater.*, vol. 12, no. 7, p. 605, Jul. 2013.

[49] S. J. Skinner and J. A. Kilner, "Oxygen ion conductors," *Mater. Today*, vol. 6, no. 3, pp. 30–37, Mar. 2003.

[50] Q. Q. Liu *et al.*, "Enhancement of the superconducting critical temperature of Sr2CuO3+δ up to 95K by ordering dopant atoms," *Phys. Rev. B*, vol. 74, no. 10, p. 100506, Sep. 2006.

[51] T. Frello *et al.*, "Dynamics of Oxygen ordering in YBa2Cu3O6+x studied by neutron and high–energy synchrotron x–ray diffraction," *Phys. C Supercond.*, vol. 282–287, no. Part 2, pp. 1089–1090, Aug. 1997.

[52] B. Lorenz, Z. G. Li, T. Honma, and P.−H. Hor, "Intrinsic tendency of electronic phase separation into two superconducting states in $La_{2-x}Sr_xCuO_{4+\delta}$," *Phys. Rev. B*, vol. 65, no. 14, p. 144522, Apr. 2002.

[53] H. E. Mohottala *et al.*, "Phase separation in superoxygenated La2−xSrxCuO4+y," *Nat. Mater.*, vol. 5, no. 5, pp. 377–382, May 2006.

[54] Y. S. Lee, F. C. Chou, A. Tewary, M. A. Kastner, S. H. Lee, and R. J. Birgeneau, "Neutron scattering study of the effects of dopant disorder on the superconductivity and magnetic order in stage−4 La2CuO4+y," *Phys. Rev. B*, vol. 69, no. 2, p. 020502, Jan. 2004.

[55] N. Poccia *et al.*, "Evolution and control of oxygen order in a cuprate superconductor," *Nat. Mater.*, vol. 10, no. 10, pp. 733–736, Aug. 2011.

[56] S. Zhang *et al.*, "Role of $SrTiO_3$ phonon penetrating into thin FeSe films in the enhancement of superconductivity," *Phys. Rev. B*, vol. 94, no. 8, p. 081116, Aug. 2016.

[57] S. N. Rebec *et al.*, "Coexistence of Replica Bands and Superconductivity in FeSe Monolayer Films," *Phys. Rev. Lett.*, vol. 118, no. 6, p. 067002, Feb. 2017.

[58] N. Jenkins *et al.*, "Imaging the essential role of spin fluctuations in high−T c superconductivity," *Phys. Rev. Lett.*, vol. 103, no. 22, p. 227001, 2009.

[59] Y. Sun *et al.*, "High temperature superconducting FeSe films on $SrTiO_3$ substrates," *Sci. Rep.*, vol. 4, p. 6040, Aug. 2014.

[60] L. Rademaker, Y. Wang, T. Berlijn, and S. Johnston, "Enhanced superconductivity due to forward scattering in FeSe thin films on SrTiO 3 substrates," *New J. Phys.*, vol. 18, no. 2, p. 022001, 2016.

[61] Y. Bang, "Pairing mechanism of heavily electron doped FeSe systems: dynamical tuning of the pairing cutoff energy," *New J. Phys.*, vol. 18, no. 11, p. 113054, 2016.

Appendix

A. STM2 Instrumentation

A.1 STM Design

The weight of the STM was lightened to improve the low temperature performance. (~110g with sample holder). In the continuous flow type cooling method, the cooling power is determined according to the flow amount, but when the coolant flows heavily, the vibration problem and the consumption of the coolant become worse. However, since it has a temperature stability of ±1mK, it is advantageous for STM to make the heat mass as light as possible. In the case of a system with a large heat mass, it is advantageous in the temperature fluctuation of the reservoir but has a slow cooling rate and is exposed to radiation heating because of its large volume. It is good to lighten the mass of the STM when the stability of the reservoir is secured. The STM head was made of copper for heat conductivity. In the transport measurement using M4PP, the temperature response of the system is important, so we used material that maximizes the heat conductivity. Vibration isolation was performed using Inconel spring, Eddy current damper, and optical table. When LHe cooling was performed with a two-layer copper shield, the minimum STM operating temperature could be reduced to ~ 6K. Temperature can be changed by controlling the flow of the PID controlled heater and coolant connected to the cryostat. In STM2, up to 7 deposition ports were made with E-beam heater and resistance heater in preparation chamber for interlocking with MBE. The Deposition Rate is measured through a home built thickness sensor.

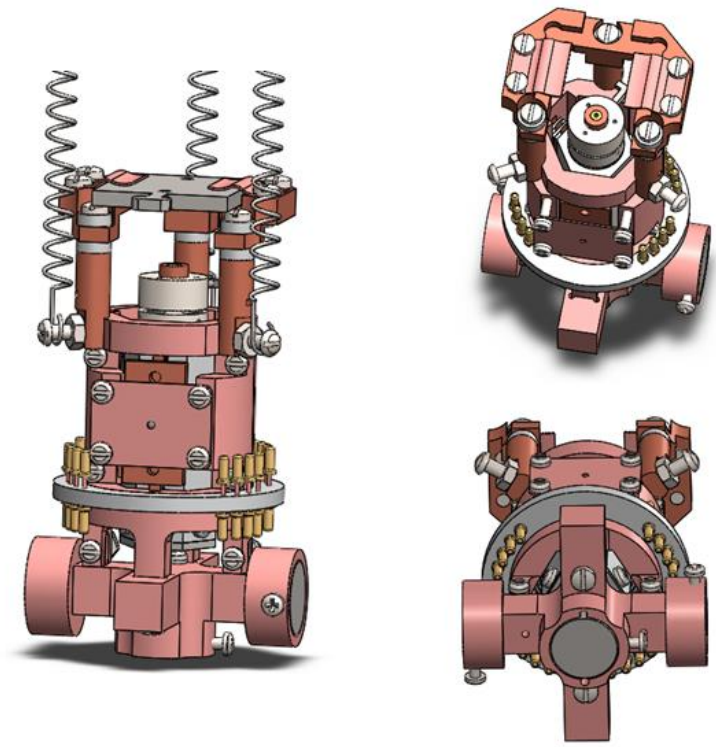

Figure 58. STM2 Head design

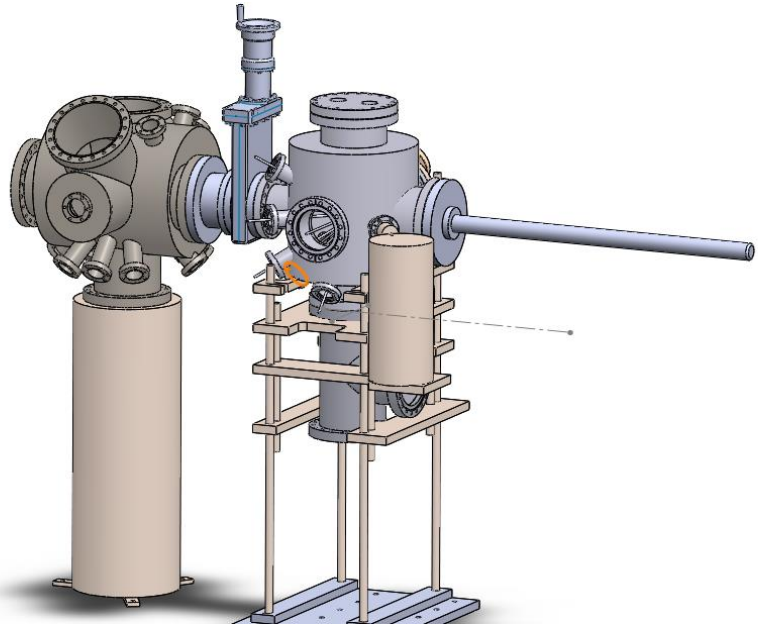

Figure 59. Main chamber and sample growth Chamber system design.

A.2 Multifunctional Tip Holder Stage

The STM2 system can be equipped with a variety of probes using a tip holder stage with four electrodes. In addition to the basic STM tip, you can also mount Qplus sensors for AFM and M4PP sensors for transport measurements.

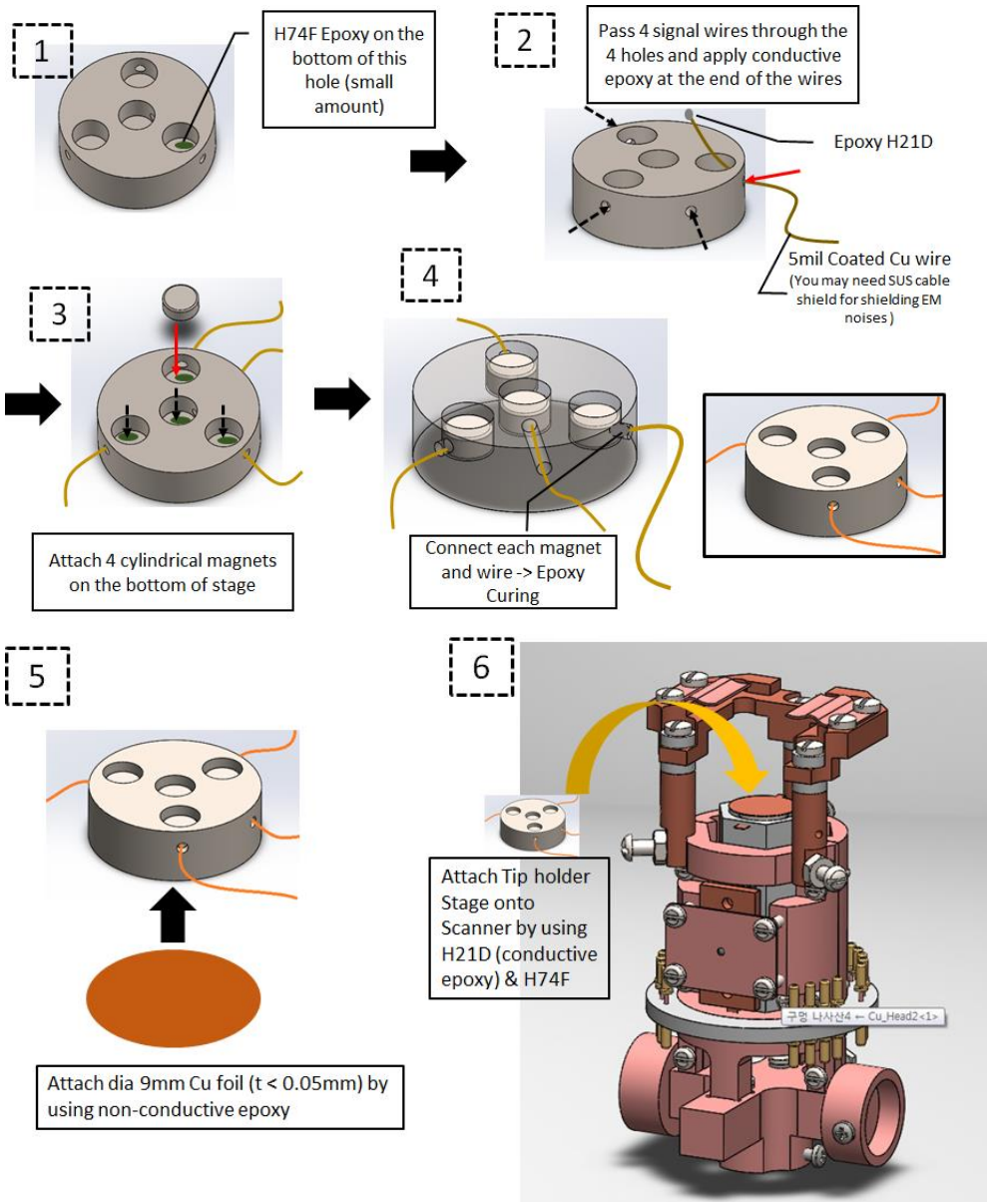

Figure 60. Multi probe mountable tip holder

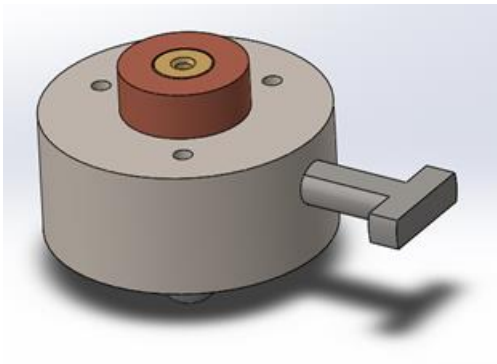

Figure 61. Tip holder for STM.

This tip holder has 3 iron ball for mechanical and electrical contact

The tip holders carrying each probe have three or four iron balls underneath, and the balls are combined with the magnets on the tip holder stage. A tip holder with three balls can basically make a 3-point contact to obtain a mechanical stability, but in the case of a tip holder with 4 balls, it is difficult to obtain a stable three point contact so that the ball in the middle is suspended by a wire, and only the remaining three balls were rigidly connected to the sample holder body. In addition, each of the magnets attached to the tip holder stage provides stable mechanical contact, and also acts as four different electrodes through the wires attached to the magnet to enable the use of various functional tips.

B. Cryogenic preamplifier

B.1 Bias voltage stability measurement

At low temperature, electromagnetic noise couples directly to measurement devices and/or heats up the electrons of the sample even the sample is cooled down to the certain temperature. This effect makes the result we got from at low temperature can only be interpreted with an effective temperature which is larger than the temperature of the sample itself. The goal of our preamplifier is achieving lower effective temperature. In order to understand this scheme, we should look into the mechanism how the effective temperature can be created. For STS, tunneling current can be simply expressed as, (Assume that it is sample bias)

$$\mathrm{I} = \frac{4\pi \mathrm{e}}{\hbar}\int_{-\infty}^{\infty} d\epsilon\,[f(eV+\epsilon)-f(\epsilon)]\rho_S(eV+\epsilon)\rho_T(\epsilon)$$

Now, at finite temperature

$$\frac{\mathrm{dI}}{\mathrm{dV}}(V) \propto \int_{-\infty}^{\infty} d\epsilon - \frac{\partial f}{\partial \epsilon}(-eV+\epsilon)\rho_S(\epsilon) = \int_{-\infty}^{\infty} d\epsilon\, p(V,\epsilon)\rho_S(\epsilon)$$

where, $p(V,\epsilon) \equiv -\frac{\partial f}{\partial \epsilon}(\epsilon - eV) = \frac{1}{4k_BT}\mathrm{sech}\left(\frac{\epsilon - eV - \mu}{2k_BT}\right)^2$

We can see the STS result can be divide into DOS and the function of V and ϵ. Physically, the function p can be interpreted as probability distribution that an electron which tunnels the junction can have energy ϵ when the certain initial bias voltage V applied. Now, consider the noise and the noise make instable bias voltage. Then, statistically,

$$\langle \frac{\mathrm{dI}}{\mathrm{dV}}(\bar{V})\rangle = \int_{-\infty}^{\infty} dV\ \frac{\mathrm{dI}}{\mathrm{dV}}(V)P(V;\bar{V})$$

,where P is probability distribution of V having mean value $\bar{V}$.

$$\langle \frac{\mathrm{dI}}{\mathrm{dV}}(\bar{V})\rangle \propto \int_{-\infty}^{\infty} dV\ \int_{-\infty}^{\infty} d\epsilon\, p(V,\epsilon)\rho_S(\epsilon)\, P(V;\bar{V}) = \int_{-\infty}^{\infty} d\epsilon\, P_t(\bar{V},\epsilon)\rho_S(\epsilon)$$

, where $P_t(\bar{V},\epsilon) = \int_{-\infty}^{\infty} dV\, p(V,\epsilon)P(V;\bar{V})$, it is a total probability distribution caused by thermal distribution and electrical noise.

Now, it is quite reasonable to assume the electrical noise is WGN(white Gaussian noise), because a lot of white noise can be represented as a Gaussian.

$$P(V;\bar{V}) = \frac{1}{\sqrt{2\pi\sigma_n}} e^{-\frac{(V-\bar{V})^2}{\sigma_n^2}}$$

Where, σ_n is a standard deviation of WGN so that it is equivalent to rms voltage of noise (V_n).To calculate conveniently, we can approximate $p(V,\epsilon)$ as a Gaussian distribution having same standard deviation, and set e=1 (dimensionless value) so that eV−>V,

$$\sigma_p \equiv \sigma[p(V,\epsilon)] = \sigma\left[\frac{1}{4k_BT}\operatorname{sech}\left(\frac{\epsilon-V-\mu}{2k_BT}\right)^2\right] =$$

$$\left[\frac{1}{4k_BT}\int_{-\infty}^{\infty} dx\, x^2 \operatorname{sech}\left(\frac{x}{2k_BT}\right)^2\right]^{\frac{1}{2}} = \frac{\pi}{\sqrt{3}}k_BT$$

Therefore,

$$p(V,\epsilon) \cong \frac{1}{\sqrt{2\pi\sigma_p}} e^{-\frac{(\epsilon-V-\mu)^2}{\sigma_p^2}}$$

Then we can substitute this function with the function in integral aforementioned and calculate the integral, we can get

$$P_t(\bar{V},\epsilon) \cong \frac{1}{\sqrt{2\pi\sigma_t}} e^{-\frac{(\epsilon-\mu_t)^2}{\sigma_t^2}}.$$

Where $\sigma_t = \sqrt{\sigma_n^2 + \sigma_p^2}$, $\mu_t = \bar{V} + \mu$

Again make this function back to the square secant distribution (derivative of Fermi distribution) and set V−>eV and $\sigma_n \to V_n$, we can get

$$\frac{\pi}{\sqrt{3}}k_BT_{eff} = \sigma_t$$

$$T_{eff} = \sqrt{T^2 + \frac{3e^2V_n^2}{k^2\pi^2}}$$

Therefore, if we want to have 50mK effective temperature for 10mK system, the rms noise voltage should be equal or less than 76.57uV. If we limit input voltage bandwidth to 1.6KHz, roughly voltage noise density should be less than 1.914 uVrms/ √Hz.

Consequently, it is apparent to remove RF frequency noise for input and output, even if STM just has several KHz bandwidth in its measurement devices. Since WGN is a noise spread all frequency range, high frequency noise can contribute to increase standard deviation of the WGN if we do not get rid of the noise, as following relation,

$$V_n^2 = \sigma_n^2 = \frac{1}{T}\int_0^T V(t)^2 dt = \int_0^\infty v(f)^2 df$$

,where $v(f)^2$ is a power spectral density of noise signal V(t), T ->∞.

This means V_n is increased as well, then the effective temperature raises. The point of this analysis is that we can describe effective temperature only in terms of sample temperature and electrical noise. It means the source which increases electron temperature can be dealt with electrically and it can be reduced electrical methods likewise filters. Thus, what we can do is just pay attention to reduce electrical noise from noise sources.

B.2 Circuit analysis

In this circuit, we should use low resistance feedback resistor and high capacitance feedback capacitors, in order to decrease high frequency noise from input op-amp itself. However too small feedback resistor value decrease the input resistance in order to keep amplifying ratio. If the input resistance is small, it distort the input voltage from external source. Also we should use op-amp as following conditions written below,

1. low voltage noise density

2. low GBW product – in order to decrease high frequency cutoff (at noise gain)

3. low 0.1~10Hz noise.

4. low current noise density

5. High open-loop gain – in order to make same voltage to the input electrodes

*(optional: low offset voltage, low bias current)

– The lower the number in this list means, the more important parameter. Now, I will describe why we need above things to establish small voltage noise output. Our noise model of voltage input part can be represented as below figure.

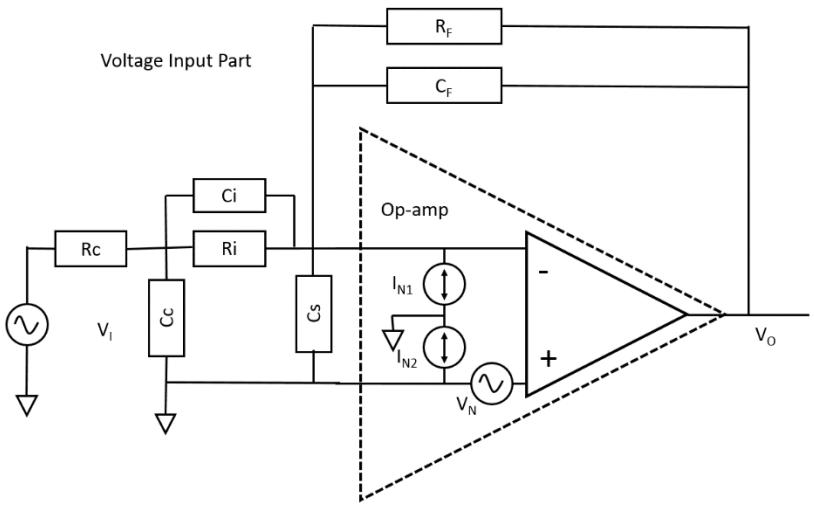

Figure 62. Noise model of cryogenic preamplifier–Voltage input part

First, I disregarded Johnson noise of two resistors, because Johnson noise of R1 is 1.48 nV/√Hz and Rf is 0.47nV/√Hz at 4K, and these values are negligible.

*Note : Even if one noise source has noise level as 1/3 large as noise level of the other source, it is quite negligible because total noise level is square root of sum of squares. I.e.

$$\text{Total noise} = \sqrt{N^2 + \left(\frac{N}{3}\right)^2} = \sqrt{\frac{10}{9}N^2} \cong 1.05N \approx N$$

In this model, Rc is resistance of cable Cc is stray capacitance of signal cable, Cs is stray capacitance of op–amp itself, Ci is stray capacitance of input resistor, and VI is noise from input signal. Also Vn, In1, and In2 are internal noise source of an op–amp.

Now, we can divide the noise sources independently because of superposition rule. At the V_o, we can simply calculate the contributions of each noise sources

$$V_{o1} = -\frac{R_F \parallel C_F}{R_i \parallel C_i} V_I$$

$$V_{o2} = 1 + \frac{R_F \parallel C_F}{(R_i \parallel C_i + R_c \parallel C_c) \parallel C_s} V_N$$

$$V_{o3} = (R_F \parallel C_F) I_{N1}$$

Thus, total noise density is

$$V_O = \sqrt{V_{O1}^2 + V_{O2}^2 + V_{O3}^2}$$

And, total noise is

$$V_T = \sqrt{\int_0^{f_0} df \, (V_{O1}^2 + V_{O2}^2 + V_{O3}^2)}$$

,where f_0 is roll-off frequency of noise gain (roughly f0= GBP/ high frequency noise gain). Therefore, if the GBP is small, total noise level can be small in that it limits the range of integration. More precisely, we can use infinite frequency boundary and finite open loop gain. Important thing is that cable capacitance does not contribute output noise here.

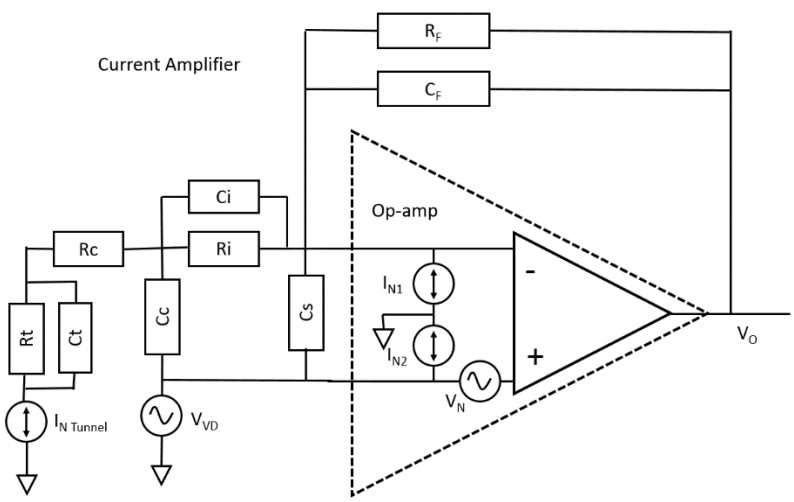

Figure 63. Noise model of cryogenic preamplifier-current amplifier part

B.3 Cabling

For cabling, in order to make effective temperature lower, we should pay attention to the voltage noise from external source. Actually voltage noise can be induce by the stray inductance of the cable, because of $V = L\frac{dI}{dt}$. For our signal bandwidth range, we don't have to worry about electrostatic noise if we make ground very well. Make sure that large capacitance between source and ground makes small noise voltage fluctuation. However large capacitance make big current noise fluctuation. For stray inductance, this effect appears oppositely. However, for the coaxial cable, inductance is proportional to $\ln\left(\frac{r_{out}}{r_{in}}\right)$, even though capacitance is inversely proportional to it. The only way to reduce both inductance and capacitance is making the cable as short as possible if we cannot change the insulating material.

Therefore, it is the best solution to separate voltage source and current measurement part. Then they can have different scheme in cabling. If it is possible, I would like to make 3 or 4-point measurement for STM, such that one or two cables are connected to sample, and the other two cables are connected to tip. But magnetic noise can induce voltage noise. In order to decrease this, we can use twisted pair, current driven shield (for current returning, this is different with voltage driven shield), Mu-metal shield or superconductor shield.

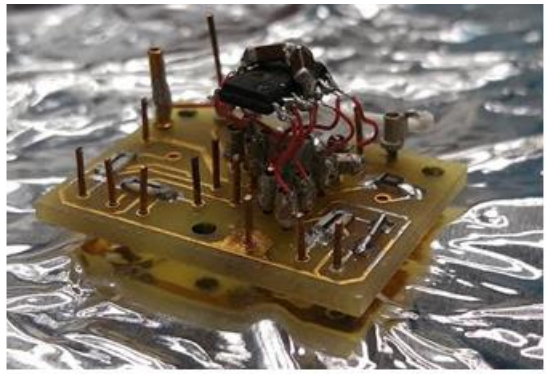

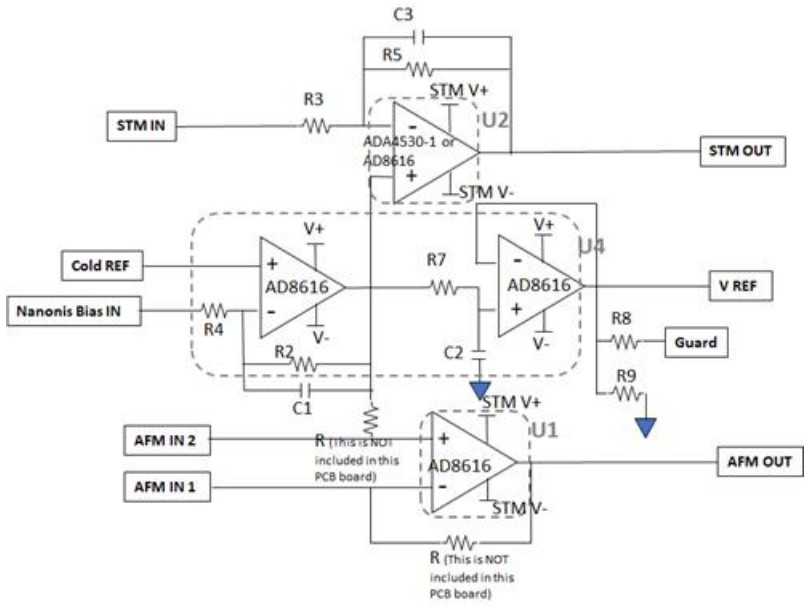

Figure 64.Cryogenic preamplifier and its schematic design

C. Sn/InSb(111)

Stanene is a material that occurs when Sn makes a honeycomb structure and is being predicted as a 2D topological insulator. Similarly, from the ARPES experiments, Sn on InSb (100) was found to have topological behavior. In order to realize 2D topological insulator, Sn was deposited on InSb (111) surface and the following structure was shown. The lattice mismatch between Sn and InSb (111) was so large that it did not grow uniformly into a crystal, and thus the Stanene structure could not be found.

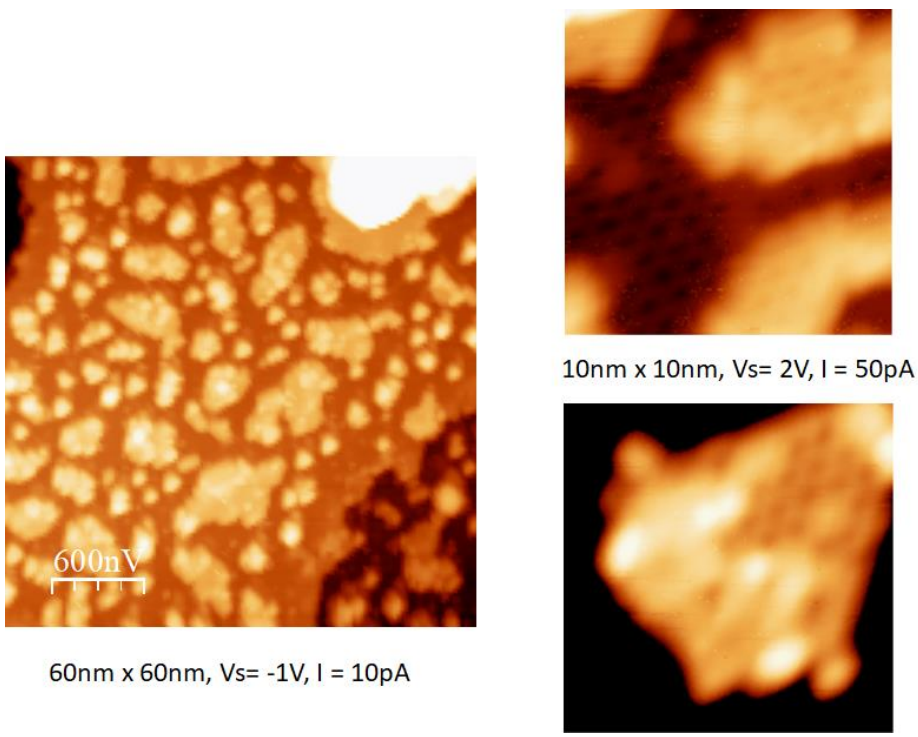

Figure 65. Sn on InSb(111) surface

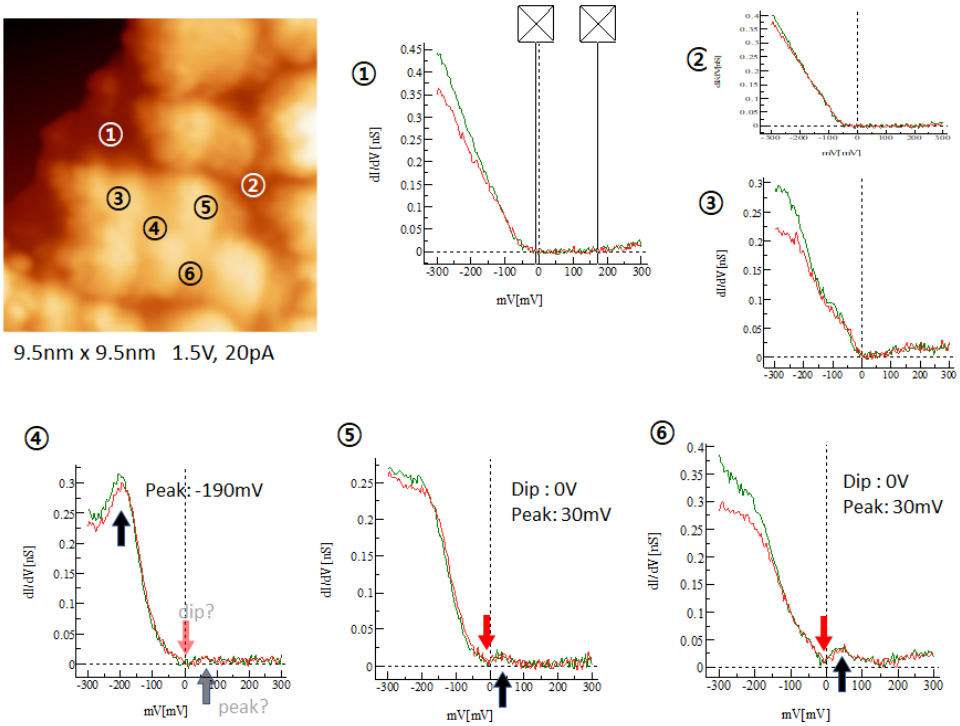

Figure 66. Tunneling spectra of Sn/InSb(111)

D. SnSe on Ge(111)

SnSe was predicted by topological crystalline insulator (TCI) and succeeded in growing in Bi2Se3 in the Q. Xue group. We have grown about 5 ~ 6 ML of SnSe on Se-terminated Ge (111) substrate. This SnSe is generally semiconducting, but when it is stressed by the substrate and transforms from orthorhombic to tetragonal structure, it becomes TCI due to its crystalline symmetry. We have shown through experiments that SnSe has a Dirac cone-like energy dispersion near the Fermi energy. In addition, this Dirac cone like shape has locality, which is visible and invisible depending on its location. This can be interpreted as observing on the lattice with tetragonal symmetry due to stress and semi-conducting like shape on the non-lattice.

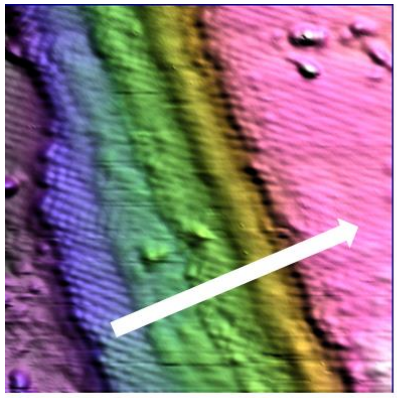

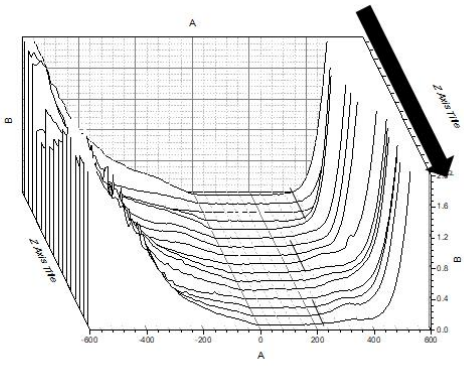

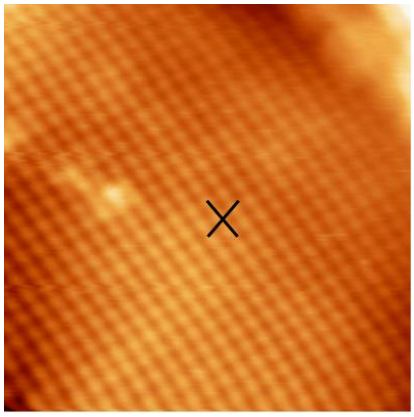

9.5nmX9.5nm
-1.5V 30pA

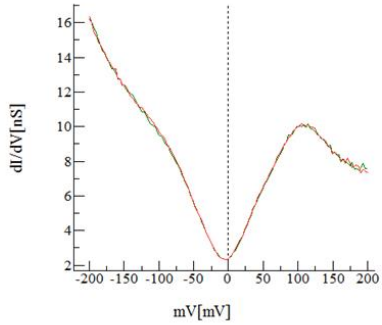

Reference condition: -0.2V, 2nA
Modulation: 371Hz, 3mV
Time constant: 10ms

Figure 67. SnSe on Ge(111)

초 록

정수 양자 홀 효과의 발견은 위상학적 시스템에 대한 많은 연구를 이끌어 냈다. 최근 몇 년 동안 광범위하게 연구되어 온 2D 또는 3D 위상학적 시스템에 대한 연구로 지금까지 알려지지 않은 새로운 물리적 특성에 대한 이해가 향상되었다. 1D 위상학적 시스템에 대한 연구 또한 Su-Schrieffer-Heeger(SSH)에 의해 시작되었으며, Majorana zero mode 와 같은 많은 특이한 현상이 지금까지 발견되었다.

현재까지 독립된 1D 시스템의 예는 많지 않다. 이 논문을 통해 나는 Se 원자가 Ge (111) 위에 자기 조립되어 있고 엇갈린 호핑 구조로 배열되어 있으며 이 독특한 구조가 polyacetylene 과 유사한 시스템을 만든다고 보고한다. Se 체인의 양 끝 단에 에지 상태가 발견되었고 위상학적인 모델을 통한 해석이 가능하다는 것을 보였다. 같은 방식으로, 1 차원 와이어 뿐만 아니라 자기 조립 된 Se 아일랜드 가장자리에도 에지 상태가 있는 것을 발견했다.

토폴로지 절연체 외에도, 또 다른 강하게 상관관계가 있는 시스템으로 다른 고온 초전도체 (HTSC)가 있다. HTSC 의 패러디 메커니즘은 아직 잘 알려져 있지 않다. 많은 HTSC 가 주사터널링 현미경(STM)으로 연구되었지만, 이 논문에서는 2012 년에 Xue 그룹에서 처음으로 보고 된 계면유도박막초전도체 인 FeSe/$SrTiO_3$ (100)을 연구하였다. 2 차원 고온 초전도체와 비정상적으로 높은 초전도 상전이 온도가 $SrTiO_3$ 또는 TiO_2 기판에서만 나타나기 때문에, 이 특이한 현상의 메커니즘에 대한 많은 연구가 이루어졌다. 이 본 논문에서 도핑 레벨을 조정하면서 연구에서 도펀트 상태를 관찰했으며, 그 오더링이 높은 Tc 의 형성에 어떻게 기여하는지 연구했다. 우리는 또한 Migdal-Eliashberg 모델을 기반으로 전자의 쌍을 만드는 Bosonic 모드에 대한 연구를 하였다.

주요어: 위상절연체, 고온초전도체, FeSe/STO
학번: 2014-30112